

# **Dynamics of Flexible Multibody Systems**

Small Vibrations Superimposed on a  
General Rigid Body Motion



# **Dynamics of Flexible Multibody Systems**

## **Small Vibrations Superimposed on a General Rigid Body Motion**

Proefschrift

ter verkrijging van de graad van doctor  
aan de Technische Universiteit Delft,  
op gezag van de Rector Magnificus prof.dr.ir. J.T. Fokkema  
voorzitter van het College van Promoties,  
in het openbaar te verdedigen op maandag 29 april 2002 om 16:00 uur  
door Arend Leendert SCHWAB,  
werktuigkundig ingenieur,  
geboren te Naarden.

Dit proefschrift is goedgekeurd door de promotor:  
Prof. dr. ir. P. Meijers

Samenstelling promotiecommissie:

Rector Magnificus, voorzitter

Prof. dr. ir. P. Meijers, Technische Universiteit Delft, promotor

Prof. dr. ir. D. J. Rixen, Technische Universiteit Delft

Prof. dr. ir. G. Lodewijks, Technische Universiteit Delft

Prof. dr. ir. J. B. Jonker, Universiteit Twente

Prof. dr. J. C. Samin, Université catholique de Louvain

Prof. dr. C. Glocker, Eidgenössische Technische Hochschule Zürich

Dr. ir. J. P. Meijaard, Technische Universiteit Delft

Title: Dynamics of Flexible Multibody Systems; Small Vibrations  
Superimposed on a General Rigid Body Motion. Ph.D. thesis, Delft  
University of Technology, Delft, The Netherlands, April 2002.

Author: Schwab, Arend L.

Subject headings: Mechanics, Multibody Dynamics, Mechanical Vibrations, Finite El-  
ement Method.

Cover: Andre Dekker (1956 - ), *Bladstudie*, 1994.

Copyright: Arend L. Schwab, Delft, The Netherlands, 2002.

Print: Ponsen en Looijen BV.

ISBN 90-6464-932-4

to Ellen

*with whom I settled down,  
who gave me peace, and peace of mind,  
just always being there.*



# Contents

- 1 Introduction** **1**
  
- 2 Finite Element Modelling** **5**
  - 2.1 Equations of Motion . . . . . 6
  - 2.2 Nominal Rigid Body Motion . . . . . 8
  - 2.3 Linearized Equations of Motion . . . . . 8
  - 2.4 Non-Holonomic Systems . . . . . 10
    - 2.4.1 Equations of Motion . . . . . 11
    - 2.4.2 Linearized Equations of Motion . . . . . 14
  
- 3 Special Finite Elements** **17**
  - 3.1 Cylindrical Bearing . . . . . 17
  - 3.2 Belt and Pulley Pair . . . . . 19
    - 3.2.1 Cable Drum . . . . . 24
  - 3.3 Gear Pair . . . . . 26
    - 3.3.1 Application to a Step-Dwell Mechanism . . . . . 29
  - 3.4 Spatial Hinge . . . . . 30
    - 3.4.1 Application to a Cardan Joint . . . . . 33
  - 3.5 Two-Dimensional Wheel . . . . . 34
    - 3.5.1 Application to a Planimeter . . . . . 36
    - 3.5.2 Swivel Wheel Shimmy . . . . . 39
  - 3.6 Three-Dimensional Wheel . . . . . 42
    - 3.6.1 The Rolling Disk . . . . . 45
    - 3.6.2 Bombardier-ILTIS Road Vehicle . . . . . 48
  
- 4 Solution Techniques for Small Vibrations** **53**
  - 4.1 Periodic Solution . . . . . 55
  - 4.2 Transient Solution . . . . . 57

4.3	Stability of the Solutions . . . . .	58
4.4	Examples and Comparison . . . . .	60
4.4.1	Parametrically Excitated Pendulum . . . . .	60
4.4.2	Slider-Crank Mechanism . . . . .	65
4.4.3	Rotor Dynamics Model . . . . .	68
4.4.4	Cardan Drive Shaft . . . . .	70
4.4.5	Slider-Crank Mechanism with Joint Clearance . . . . .	74
<b>5</b>	<b>Joint Clearance</b>	<b>79</b>
5.1	Joint Clearance Model . . . . .	80
5.2	Continuous Contact Force Models . . . . .	81
5.2.1	Hertzian Contact Force Model with Dissipation . . . . .	81
5.2.2	Hydrodynamic Contact Force Model . . . . .	84
5.3	Discontinuous Contact Force Model . . . . .	85
5.3.1	Impulse Equations . . . . .	85
5.3.2	Numerical Aspects of Impact Analysis . . . . .	87
5.4	Application to a Slider-Crank Mechanism . . . . .	91
5.4.1	Continuous Hertzian Contact Force Model . . . . .	92
5.4.2	Impact Model with Estimated Maximum Contact Force . . . . .	93
5.4.3	Continuous Hertzian Contact Force Model and Elastic Connecting Rod . . . . .	96
5.4.4	Continuous Contact Force Model with Hydrodynamic Lu- bricated Bearing . . . . .	97
5.5	Discussion . . . . .	98
<b>6</b>	<b>Concluding Remarks</b>	<b>103</b>
6.1	Conclusions . . . . .	103
6.2	Suggestions for Further Research . . . . .	104
<b>A</b>	<b>Equations of Motion and Linearization</b>	<b>107</b>
A.1	Equations of Motion . . . . .	108
A.2	Nominal Gross Motion . . . . .	115
A.3	Linearized Equations of Motion . . . . .	116
A.4	Extensions to Non-Holonomic Systems . . . . .	123
A.4.1	State Equations . . . . .	125
A.4.2	Linearized State Equations . . . . .	128
<b>B</b>	<b>Quaternions, Finite Rotation, and Euler Parameters</b>	<b>131</b>

CONTENTS

ix

<b>C An Algorithm for Hydrodynamic Journal Bearing Forces</b>	<b>137</b>
<b>Summary</b>	<b>141</b>
<b>Samenvatting</b>	<b>143</b>
<b>Curriculum Vitae</b>	<b>145</b>
<b>References</b>	<b>147</b>



# Chapter 1

## Introduction

*Beginning my studies the first step pleas'd me so much,  
The mere fact consciousness, these forms, the power of motion,  
The least insect or animal, the senses, eyesight, love,  
The first step I say awed me and pleas'd me so much,  
I have hardly gone and hardly wish'd to go any farther,  
But stop and loiter all the time to sing it in ecstatic songs.*

(Walt Whitman, *Leaves of Grass*)

In the dynamic analysis of engineering problems a multibody model in which all structural elements are assumed to be rigid suffices for a quick judgement about the motion and forces in the system. However, in cases where a high accuracy is required, for instance in positioning mechanisms, or where the structural elements are rather compliant, vibrations due to deformation can become important and have to be considered. Incorporation of these deformations in the dynamic analysis of the system enlarges the number of degrees of freedom, the frequency range of interest, and the stiffness of the differential equations, which results in a longer simulation time.

To reduce the simulation time and to gain more insight in the vibration phenomena at hand we assume that the effect of deformation may be approximated by superimposing small linear vibrations on the nominal rigid body motion. This idea has been inspired by the computational results from simulations of flexible multibody systems where one often recognizes a gross rigid body motion with small-amplitude nearly harmonic vibrations added.

The method of superimposition as presented here systematically leads to a system of linear differential equations with time-varying coefficients and time-varying forcing. In particular, if the nominal reference motion is periodic, the

coefficients and forcing are also periodic. The equations are amenable to several kinds of analysis, such as the determination of transient and periodic solutions, the investigation of the stability of these solutions and the continuation of these solutions if a parameter, for instance the driving speed of the multibody system, is varied.

The equations of motion for the flexible multibody system and their linearization, which describe the small vibrations, are derived by a finite element method. With the help of a limited number of element types it is possible to model a variety of flexible multibody systems. Typical types of elements are beam, truss and hinge elements, while more specialized elements are used to model joint connections and transmissions of motion. The finite element approach for the kinematic and dynamic analysis of mechanisms and machines was initiated by Besseling [2] who, in his study of discretization methods for deriving finite dimensional element models for the mechanics of continua, pointed at the complete analogy between the discrete case and the continuous case. The analogues of the physical stresses and strains for the continua are the so-called generalized stresses and generalized strains for the finite elements. Van der Werff [83] used the large displacement formulation of Visser and Besseling [86] to model (partly) rigid elements by equating some generalized deformations to zero and introduced the transfer function formalism. With these methods he started the development of computer programs for the kinematic analysis of two-dimensional (PLANAR) and three-dimensional (SPACAR [84]) mechanisms and machines. The author implemented the first extension for the dynamic analysis of flexible multibody systems in the program [67]. The method for dynamic analysis and the corresponding software matured by the thesis of Jonker [29]. In the course of years, the SPACAR program system [31] has been enlarged, among others, by Jonker [32] for handling of controlled robotic manipulators, and by Meijaard [45] for the direct determination of periodic solutions of flexible multibody systems and many other options.

The method of superimposition as presented here can also be applied to systems having rolling contact, as in road vehicles and track-guided vehicles. If these contacts are ideal, they impose, in addition to some holonomic constraints, also non-holonomic constraints on the system, which can be expressed as constraints of special finite elements like the wheel on a surface. These new element types and a procedure for formulating the equations of motion for such flexible non-holonomic systems and their linearization are part of this thesis.

To implement these elements and methods in the SPACAR program system a more versatile implementation was needed than the original FORTRAN-IV version started in 1980 by Van der Werff. After thorough investigation we, the author

and J. P. Meijaard, decided to re-code the software in FORTRAN77. Keeping in mind an object oriented approach for the element procedures and using include-files and parameters to define the global memory allocation, we came up with an implementation, SPACAR95, which has proved its functionality over the past years. Some of the ideas which helped the viability of this implementation can be found in the “credo” part of the manual [72].

The outline of this thesis is as follows. In Chapter 2 the method of finite element modelling as applied to flexible multibody systems is briefly described. The equations of motion and their linearization for both holonomic and non-holonomic constrained systems are derived. In Chapter 3 an extension to the typical set of element types is presented. With the introduced belt (or cable) and pulley pair and gear pair element a broad range of planar mechanisms and machines can be analysed. The cylindrical bearing element and the redefined three-dimensional cylindrical hinge element can be used for describing large relative motion in the system. Finally two elements for describing rolling contact are introduced, the two-dimensional wheel element or knife edge element and the three-dimensional wheel element like a sharp edge bounded disk on a surface. In the definition of the spatial element types finite rotations are described by Euler parameters, in which a fruitful use of quaternion algebra is made. All element types are illustrated with an appropriate engineering examples. In Chapter 4 the solution techniques for the determination of the transient and periodic solutions of the small vibration problem are presented. For the stability analysis of the periodic solutions a method directly based on the Floquet theory is used. The techniques are illustrated by examples with increasing complexity. In Chapter 5 the effect of joint clearance on the dynamic response of a flexible multibody system is discussed. Joint clearances due to manufacturing tolerances and wear can seriously affect the dynamic response of multibody systems. In unlubricated joints it is usually accompanied by rattling, excessive wear and noise, caused by peak contact forces. A critical factor in the precise prediction of the peak forces is the contact model being used. In this chapter a comparison is made between a continuous and a discontinuous contact force model. For the discontinuous model, impact with rebound, a method is presented to predict the maximum impact force for given elastic joint material properties. Since many of the joint clearances in mechanisms and machines are in lubricated bearings, a comparison is made between an unlubricated and a hydrodynamic lubricated bearing in a slider-crank mechanism. The effect of the joint clearance on the dynamic response of the multibody system is handled with the concept of small vibrations superimposed on non-linear rigid body motion as described in Chapter 4.

The work presented here is partly based on some of the earlier publications of the author. Preliminary versions of the wheel element can be found in [68], whereas some of the other special finite elements are presented in [70]. A mature version of the wheel element together with methods for dynamic analysis of flexible non-holonomic multibody systems are presented in [71]. The method of superimposition was first published in [69] and found its final form in [73]. The part on the effect of joint clearance on the dynamic response of flexible multibody systems is reproduced in [74].

As for the applied notation, algebraic vectors and matrices are denoted by bold face symbols, where typically lower-case characters are used for vectors and upper-case characters for matrices.

## Chapter 2

# Finite Element Modelling

*On ne trouvera point de Figures dans cet Ouvrage. Les méthodes que j'y expose ne demandent ni constructions, ni raisonnemens géométriques ou mécaniques, mais seulement des opérations algébriques, assujetties à une marche régulière et uniforme. Ceux qui aiment l'Analyse, verront avec plaisir la Mécanique en devenir une nouvelle branche, et me sauront gré d'en avoir étendu ainsi le domaine.*

No figures will be found in this work. The methods I present require neither constructions nor geometrical or mechanical arguments, but solely algebraic operations subject to a regular and uniform procedure. Those who appreciate mathematical analysis will see with pleasure mechanics becoming a new branch of it and hence, will recognize that I have enlarged its domain.

(Joseph Louis Lagrange, *Mécanique analytique*)

The dynamics of multibody systems with deformable bodies may well be modelled by finite elements. The finite element method is usually presented as a numerical method for solving partial differential equations that describe continuum problems in structural mechanics and other fields. On the other hand, one may look on a finite element description of a mechanical system and its physical behaviour as a model in its own right. This latter approach has been used successfully in the analysis of the strength and stiffness of structures and has proved to be useful in the kinematic and dynamic analysis of mechanisms and machines.

The distinguishing point in the finite element approach is the specification of independent deformation modes of the finite elements, the so-called generalized deformations or generalized strains. These are the algebraic analogue to

the continuous field description of deformations. Rigid body motions are displacements for which the generalized strains are zero. If the specification of the generalized strains remains valid for arbitrary large translations and rotations, rigid multibody systems such as mechanisms and machines can be analysed by setting all generalized strains to zero. These strain equations are now the constraint equations which express rigidity. Deformable bodies are handled by allowing non-zero strains and specifying constitutive equations for the generalized stresses, which are the duals of the generalized strains.

Instead of imposing constraint equations for the interconnection of bodies, which is a widespread approach in multibody system dynamics formalisms, permanent contact of elements is achieved by letting them have nodal points in common. With the help of a rather limited number of element types it is possible to model a wide class of systems. Typical types of elements are beam, truss and hinge elements, while more specialized elements can be used to model joint connections and transmissions of motion.

This chapter is organized as follows. In Section 2.1 the formulation of the equations of motion for flexible multibody systems is summarized. The rigid body motion is treated in Section 2.2, whereas the linearized equations of motion, describing the small vibrations, are derived in Section 2.3. These formalisms are the basis for solution techniques of the small vibrations superimposed on the rigid body motion, as presented in Chapter 4. In Section 2.4 the extension to the equations of motion and its linearization for flexible multibody systems having non-holonomic constraints, as may arise from the condition of rolling without slipping, are treated. Examples of such systems are presented in Chapter 3 on special finite elements. A detailed description of the equations of motion for both holonomic and non-holonomic systems and its linearization which is well fitted for coding of the presented methods can be found in Appendix A.

## 2.1 Equations of Motion

In a finite element description of a multibody system the configuration is described by a number of nodal points with coordinates  $\mathbf{x}$  and a number of elements with generalized deformations or generalized strains  $\boldsymbol{\varepsilon}$ . The nodal coordinates can be absolute coordinates of the position or parameters that describe the orientation of the nodes. The generalized deformations depend on the nodal coordinates and can be expressed as

$$\boldsymbol{\varepsilon} = \mathbf{D}(\mathbf{x}). \quad (2.1)$$

Usually constraints are imposed on some generalized deformations and nodal coordinates, which we assume, for the present section, to be holonomic. For instance, the conditions for rigidity of element  $e$  are

$$\boldsymbol{\varepsilon}^e = \mathbf{D}^e(\mathbf{x}^e) = \mathbf{0}. \quad (2.2)$$

If the constraints are consistent, the coordinates can locally be expressed as functions of the generalized coordinates  $\mathbf{q}$ , the kinematic degrees of freedom (configuration coordinates), by means of a transfer function  $\mathbf{F}$  as

$$\mathbf{x} = \mathbf{F}(\mathbf{q}). \quad (2.3)$$

The generalized coordinates can be chosen from components of the nodal coordinate vector  $\mathbf{x}$  and the generalized deformation vector  $\boldsymbol{\varepsilon}$ . Generally the transfer function cannot be calculated explicitly, but has to be determined by solving the constraint equations numerically in an iterative way. Partial derivatives are calculated by means of implicit differentiation.

The equations of motion for the constraint multibody system will be derived from the principle of virtual power and the principle of D'Alembert. This method can be traced back to Lagrange who by his monumental *Mécanique analytique* [39] became the founder of the study of motion of systems of bodies. First for each node and element in the system, we determine a mass matrix  $\mathbf{M}^e$  and a force vector  $\mathbf{f}^e$ , which give a contribution to the virtual power of

$$\delta \dot{\mathbf{x}}^{eT} (\mathbf{f}^e - \mathbf{M}^e \ddot{\mathbf{x}}^e). \quad (2.4)$$

The unreduced equations of motion for the multibody system are obtained by assembling the contribution of all elements and nodes in a global mass matrix  $\mathbf{M}$  and a global force vector  $\mathbf{f}$ , which results in the virtual power equation

$$\delta \dot{\mathbf{x}}^T [\mathbf{f}(\dot{\mathbf{x}}, \mathbf{x}, t) - \mathbf{M}(\mathbf{x}) \ddot{\mathbf{x}}] = 0. \quad (2.5)$$

Here,  $\delta \dot{\mathbf{x}}$  are kinematically admissible virtual velocities, which satisfy all instantaneous kinematic constraints. The degrees of freedom can be split in prescribed ones,  $\mathbf{q}^r$ , which are known explicit functions of time and represent the rheonomic constraints, which are the prescribed input motions, and the dynamic degrees of freedom  $\mathbf{q}^d$ . By differentiating the transfer function (2.3) we obtain

$$\dot{\mathbf{x}} = \mathbf{F}_{,\mathbf{q}} \dot{\mathbf{q}}, \quad \ddot{\mathbf{x}} = \mathbf{F}_{,\mathbf{q}} \ddot{\mathbf{q}} + \mathbf{F}_{,\mathbf{q}\mathbf{q}} \dot{\mathbf{q}} \dot{\mathbf{q}}, \quad \delta \dot{\mathbf{x}} = \mathbf{F}_{,\mathbf{q}^d} \delta \dot{\mathbf{q}}^d. \quad (2.6)$$

Here a subscript comma followed by one or more variables denotes partial derivatives with respect to these variables. The way in which higher-order derivatives

have to be multiplied by the juxtaposed vectors goes without saying. Substituting these expressions in the virtual power equation (2.5) yields the reduced equations of motion

$$\bar{\mathbf{M}}(\mathbf{q}^d, t)\ddot{\mathbf{q}}^d = \bar{\mathbf{f}}(\dot{\mathbf{q}}^d, \mathbf{q}^d, t), \quad (2.7)$$

with the reduced global mass matrix,

$$\bar{\mathbf{M}} = \mathbf{F}_{,\mathbf{q}^d}^T \mathbf{M} \mathbf{F}_{,\mathbf{q}^d}, \quad (2.8)$$

and the reduced global force vector,

$$\bar{\mathbf{f}} = \mathbf{F}_{,\mathbf{q}^d}^T [-\mathbf{M}(\mathbf{F}_{,\mathbf{q}\mathbf{q}}\dot{\mathbf{q}}\dot{\mathbf{q}} + \mathbf{F}_{,\mathbf{q}^r}\ddot{\mathbf{q}}^r) + \mathbf{f}]. \quad (2.9)$$

## 2.2 Nominal Rigid Body Motion

The nominal state of the multibody system for the small vibration superimposition method is that state in which all elements are assumed to be rigid. The input motions  $\mathbf{q}^r$  are prescribed functions of time, usually periodic, and the dynamic degrees of freedom,  $\mathbf{q}^d$ , which describe the small vibration problem, are identically equal to zero. In order to maintain these prescribed values for the deformations, additional generalized forces,  $\mathbf{f}^d$ , dual to the generalized deformations  $\mathbf{q}^d$  have to be introduced in the right-hand side of the reduced equations of motion (2.7) and the sum of all reduced forces has to be zero,

$$\mathbf{F}_{,\mathbf{q}^d}^T [-\mathbf{M}(\mathbf{F}_{,\mathbf{q}^r\mathbf{q}^r}\dot{\mathbf{q}}^r\dot{\mathbf{q}}^r + \mathbf{F}_{,\mathbf{q}^r}\ddot{\mathbf{q}}^r) + \mathbf{f}] + \mathbf{f}^d = \mathbf{0}. \quad (2.10)$$

From this equation the additional forces  $\mathbf{f}^d$  are found.

## 2.3 Linearized Equations of Motion

To describe the small vibration we have to linearize the equations of motion about the nominal solution in which the deformation mode coordinates  $\mathbf{q}^d$  are zero. Linearizing the reduced equation of motion (2.7) at  $\mathbf{q}^d = \mathbf{0}$ ,  $\dot{\mathbf{q}}^d = \mathbf{0}$  and  $\ddot{\mathbf{q}}^d = \mathbf{0}$  results in

$$\bar{\mathbf{M}}\Delta\ddot{\mathbf{q}}^d + \bar{\mathbf{C}}\Delta\dot{\mathbf{q}}^d + \bar{\mathbf{K}}\Delta\mathbf{q}^d = -\mathbf{f}^d + \mathbf{f}_a^d. \quad (2.11)$$

Here  $\bar{\mathbf{M}}$  is the system mass matrix from (2.8),  $\bar{\mathbf{C}}$  is the velocity sensitivity matrix and  $\bar{\mathbf{K}}$  contains the stiffness terms;  $\mathbf{f}^d$  are the forces from (2.10) and

$\mathbf{f}_a^d$  represents additional applied forces. These may arise from independently modelled elements or subsystems which were not included in the calculation of the nominal solution, for instance actuators with a control system or bearings and seals in rotor dynamics (see the example given in Section 4.4.3), and often they represent the non-linear contribution to the small vibration problem. The system mass matrix  $\bar{\mathbf{M}}$  is symmetric, but  $\bar{\mathbf{C}}$  and  $\bar{\mathbf{K}}$  need not be so.

The matrices of the linearized equations are determined in the following way. First, for all elements and nodes the contribution to the global stiffness matrix  $\mathbf{K}$  and the global velocity matrix  $\mathbf{C}$  are determined as

$$\mathbf{C}^e = -(\mathbf{f}^e)_{,\dot{\mathbf{x}}^e}, \quad \mathbf{K}^e = (\mathbf{M}^e \ddot{\mathbf{x}}^e - \mathbf{f}^e)_{,\mathbf{x}^e}. \quad (2.12)$$

These global matrices having been determined, the matrices in the linearized equations are given by

$$\begin{aligned} \bar{\mathbf{C}} &= \mathbf{F}_{,\mathbf{q}^d}^T \mathbf{C} \mathbf{F}_{,\mathbf{q}^d} + 2\mathbf{F}_{,\mathbf{q}^d}^T \mathbf{M} \mathbf{F}_{,\mathbf{q}^d \mathbf{q}^d} \dot{\mathbf{q}}, \\ \bar{\mathbf{K}} &= \mathbf{F}_{,\mathbf{q}^d}^T \mathbf{K} \mathbf{F}_{,\mathbf{q}^d} + \mathbf{F}_{,\mathbf{q}^d \mathbf{q}^d}^T [\mathbf{M} \ddot{\mathbf{x}} - \mathbf{f}] + \\ &\quad \mathbf{F}_{,\mathbf{q}^d}^T [\mathbf{M} (\mathbf{F}_{,\mathbf{q}^d \mathbf{q}^d} \ddot{\mathbf{q}} + \mathbf{F}_{,\mathbf{q}^d \mathbf{q}^d \mathbf{q}^d} \dot{\mathbf{q}} \dot{\mathbf{q}}) + \mathbf{C} \mathbf{F}_{,\mathbf{q}^d \mathbf{q}^d} \dot{\mathbf{q}}]. \end{aligned} \quad (2.13)$$

The independently modelled elements or subsystems can be included in the small vibration problem in a linearized form. For such an element  $e$ , the additional reduced forces  $\mathbf{f}_a^{de}$  follow from linearized constitutive equations and inertia terms as

$$\mathbf{f}_a^{de} = \mathbf{F}_{,\mathbf{q}^d}^{eT} (-\mathbf{K}^e \Delta \mathbf{x}^e - \mathbf{C}^e \Delta \dot{\mathbf{x}}^e - \mathbf{M}^e \Delta \ddot{\mathbf{x}}^e + \mathbf{f}^e). \quad (2.14)$$

The kinematics of such an additional element  $e$  are determined from the transfer functions and the degrees of freedom as

$$\begin{aligned} \Delta \mathbf{x}^e &= \mathbf{F}_{,\mathbf{q}^d}^e \Delta \mathbf{q}^d, \\ \Delta \dot{\mathbf{x}}^e &= \mathbf{F}_{,\mathbf{q}^d}^e \Delta \dot{\mathbf{q}}^d + \mathbf{F}_{,\mathbf{q}^d \mathbf{q}^d}^e \dot{\mathbf{q}} \Delta \mathbf{q}^d, \\ \Delta \ddot{\mathbf{x}}^e &= \mathbf{F}_{,\mathbf{q}^d}^e \Delta \ddot{\mathbf{q}}^d + 2\mathbf{F}_{,\mathbf{q}^d \mathbf{q}^d}^e \dot{\mathbf{q}} \Delta \dot{\mathbf{q}}^d + [\mathbf{F}_{,\mathbf{q}^d \mathbf{q}^d}^e \ddot{\mathbf{q}} + \mathbf{F}_{,\mathbf{q}^d \mathbf{q}^d \mathbf{q}^d}^e \dot{\mathbf{q}} \dot{\mathbf{q}}] \Delta \mathbf{q}^d, \end{aligned} \quad (2.15)$$

which yields the incremental displacements, velocities and accelerations. Substitution of these results in (2.14), expansion and collection of terms gives us the contributions to the total reduced mass, velocity sensitivity and stiffness matrices and the right-hand side of the linearized equations of motion.

The resulting set of linearized equations (2.11) is amenable to several kinds of analysis. If the nominal motion is periodic and there are no non-linear terms in the additional forces, the linear differential equations have periodic coefficients

and periodic forcing. The solution techniques for the determination of periodic solutions of these equations in closed form approximation, their stability and transient solutions are described in Chapter 4. If there are non-linear additional forces in the system, a simple shooting method as described by Meijaard [43, 45] can be used to determine the periodic solutions of the periodic forced non-linear system. Transient solutions can be found by direct numerical integration of the equations of motion.

If the actual input motion is not fully described, as for instance in the case of a motor driven mechanism with a given motor characteristic, the angular deviation of this input from the nominal value can be included as an additional dynamic deformation mode coordinate by putting two hinge elements in series. The first hinge describes the nominal motion while the second hinge describes the angular deviation.

## 2.4 Non-Holonomic Systems

The motion of mechanical systems having rolling contact, as in road vehicles and track-guided vehicles, has intrigued the author from early childhood on. In broadening our horizons we make use of different means of transport, evolving from tricycles, skates, scooters, bicycles, motor scooters and cars to trains, ships and planes. The motion of each of these systems can be investigated approximately by a mechanical model having non-holonomic constraints. In the excellent book by Neĭmark and Fufaev [55], the kinematics and dynamics of non-holonomic mechanical systems are treated in great detail. They illustrate the presented theory with worked-out examples, and the book has an elaborate reference list with over 500 items.

The case of small vibrations and stability of conservative non-holonomic systems near equilibrium states has lead to some controversy in the past. Whittaker concluded in his *Analytical Dynamics* [88, Section 90] that for such cases “the difference between holonomic and non-holonomic systems is unimportant” and that the vibration motion of a given non-holonomic system with  $n$  independent coordinates and  $m$  non-holonomic constraints is the same as that of a certain holonomic system with  $n - m$  degrees of freedom. Bottema [4] showed that these conclusions are incorrect, and pointed out that the characteristic determinant of a non-holonomic system is asymmetric and that the corresponding characteristic equation possesses as many vanishing roots, as there are non-holonomic constraints. However, besides a manifold of equilibrium states, non-holonomic systems also possess a manifold of steady motion. Due to these non-zero motions

some vanishing roots may get non-zero values.

The inclusion of the non-holonomic constraints in the dynamics of flexible multibody systems as presented here, surpasses the conventional Lagrangian multipliers approach by the introduction of generalized kinematic coordinates. These coordinates, as many as there are non-holonomic constraints, describe together with the degrees of freedom the configuration of the system, whereas the velocities of the system in a given configuration are uniquely determined by the velocities of the degrees of freedom. The derivation of the linearized equations of motion is straightforward and they can, among other things, be used to analyse the stability of a nominal steady motion.

### 2.4.1 Equations of Motion

Besides the non-holonomic constraints, we assume that there are also holonomic constraints imposed on the system. The latter, as described in Section 2.1, reduces the coordinates  $\mathbf{x}$  to the independent generalized coordinates  $\mathbf{q}$  by means of a transfer function  $\mathbf{F}$  as in

$$\mathbf{x} = \mathbf{F}(\mathbf{q}, t). \quad (2.16)$$

The prescribed motions, or rheonomic constraints, which are known explicit functions of time, are represented here by the time  $t$ . The non-holonomic constraints, as may arise from elements having idealized rolling contact, can be expressed in terms of zero slip functions. Such a slip function is usually defined as some relative velocity between the two bodies in the contact area, and is therefore linear in the velocities. For instance, if element  $e$  has non-slipping components, it has to satisfy the constraints  $\mathbf{s}^e = \mathbf{V}^e(\mathbf{x}^e)\dot{\mathbf{x}}^e = \mathbf{0}$ . Assembly of all non-slipping components for the system results in the non-holonomic constraints

$$\mathbf{V}(\mathbf{x})\dot{\mathbf{x}} = \mathbf{0}. \quad (2.17)$$

Owing to these constraints, the generalized velocities  $\dot{\mathbf{q}}$  are now dependent. This dependency is expressed by a splitting of the generalized coordinates  $\mathbf{q}$  into the degrees of freedom  $\mathbf{q}^d$  and the generalized kinematic coordinates  $\mathbf{q}^k$ . The velocities of the system can now be expressed in terms of the first order transfer function  $\mathbf{H}$  times the velocities of the degrees of freedom and a term representing the prescribed motion, as in

$$\dot{\mathbf{x}} = \mathbf{H}(\mathbf{q}, t)\dot{\mathbf{q}}^d + \mathbf{v}(\mathbf{q}, t). \quad (2.18)$$

The expressions for the first order transfer function and the prescribed motion terms are found by differentiation of (2.16) and splitting of terms as in

$$\dot{\mathbf{x}} = \mathbf{F}_{,\mathbf{q}^d} \dot{\mathbf{q}}^d + \mathbf{F}_{,\mathbf{q}^k} \dot{\mathbf{q}}^k + \mathbf{F}_{,t}, \quad (2.19)$$

and substitution of this result in the non-holonomic constraints (2.17) resulting in

$$\mathbf{V}[\mathbf{F}_{,\mathbf{q}^d} \dot{\mathbf{q}}^d + \mathbf{F}_{,\mathbf{q}^k} \dot{\mathbf{q}}^k + \mathbf{F}_{,t}] = \mathbf{0}. \quad (2.20)$$

From these equations, as many as there are kinematic coordinates  $\mathbf{q}^k$ , their velocities  $\dot{\mathbf{q}}^k$  can be solved as

$$\dot{\mathbf{q}}^k = -(\mathbf{V}\mathbf{F}_{,\mathbf{q}^k})^{-1}[\mathbf{V}\mathbf{F}_{,\mathbf{q}^d} \dot{\mathbf{q}}^d + \mathbf{V}\mathbf{F}_{,t}]. \quad (2.21)$$

Substitution of this result in (2.19) and comparing terms with (2.18) results in the first order transfer function

$$\mathbf{H} = [\mathbf{I} - \mathbf{F}_{,\mathbf{q}^k}(\mathbf{V}\mathbf{F}_{,\mathbf{q}^k})^{-1}\mathbf{V}]\mathbf{F}_{,\mathbf{q}^d}, \quad (2.22)$$

and the velocities  $\mathbf{v}$ , representing the prescribed motion, as

$$\mathbf{v} = [\mathbf{I} - \mathbf{F}_{,\mathbf{q}^k}(\mathbf{V}\mathbf{F}_{,\mathbf{q}^k})^{-1}\mathbf{V}]\mathbf{F}_{,t}. \quad (2.23)$$

In both expressions we identify the use of the inverse of the Jacobian of the non-holonomic constraints with respect to the generalized kinematic coordinates

$$\mathbf{V}\mathbf{F}_{,\mathbf{q}^k}. \quad (2.24)$$

If this Jacobian is singular, we have to choose another set of generalized kinematic coordinates and consequently another set of degrees of freedom to describe the system uniquely. Having taken into account all constraints we can define the state of the system as

$$(\dot{\mathbf{q}}^d, \mathbf{q}^d, \mathbf{q}^k, t). \quad (2.25)$$

Next we will treat the dynamics of the system; the transition of the system with respect to time or, in other words, the time derivative of the state of the system.

The derivative of the first part of the state vector,  $\dot{\mathbf{q}}^d$ , with respect to time follows from the equations of motion of the system. In the generation of the equations of motion, for each node and element, we determine a mass matrix  $\mathbf{M}^e$  and a force vector  $\mathbf{f}^e$ , which give a contribution to the virtual power of

$$\delta \dot{\mathbf{x}}^{eT} (\mathbf{f}^e - \mathbf{M}^e \ddot{\mathbf{x}}^e) \quad (2.26)$$

The virtual power equation of the system is obtained by assembling the contribution of all elements and nodes in a global mass matrix  $\mathbf{M}$  and a global force vector  $\mathbf{f}$ , which results in

$$\delta \dot{\mathbf{x}}^T [\mathbf{f}(\dot{\mathbf{x}}, \mathbf{x}, t) - \mathbf{M}(\mathbf{x})\ddot{\mathbf{x}}] = 0. \quad (2.27)$$

Here,  $\delta \dot{\mathbf{x}}$  are kinematically admissible virtual velocities, which satisfy all instantaneous kinematic constraints. They follow directly from (2.18) as

$$\delta \dot{\mathbf{x}} = \mathbf{H} \delta \dot{\mathbf{q}}^d. \quad (2.28)$$

The coordinate accelerations are obtained by differentiation of the velocities (2.18), resulting in

$$\ddot{\mathbf{x}} = \mathbf{H}(\mathbf{q}, t) \ddot{\mathbf{q}}^d + \mathbf{g}(\dot{\mathbf{q}}, \mathbf{q}, t), \quad (2.29)$$

where we have collected all convective and prescribed accelerations in the  $\mathbf{g}$  terms. These accelerations, which depend only on the state of the system, are given by

$$\mathbf{g} = \mathbf{H}_{,\mathbf{q}} \dot{\mathbf{q}}^d \dot{\mathbf{q}} + \mathbf{H}_{,t} \dot{\mathbf{q}}^d + \mathbf{v}_{,\mathbf{q}} \dot{\mathbf{q}} + \mathbf{v}_{,t}. \quad (2.30)$$

Substitution of the acceleration (2.29) in the virtual power equation (2.27) yields the reduced equations of motion

$$\bar{\mathbf{M}}(\mathbf{q}^d, \mathbf{q}^k, t) \ddot{\mathbf{q}}^d = \bar{\mathbf{f}}(\dot{\mathbf{q}}^d, \mathbf{q}^d, \mathbf{q}^k, t), \quad (2.31)$$

with the reduced global mass matrix,

$$\bar{\mathbf{M}} = \mathbf{H}^T \mathbf{M} \mathbf{H}, \quad (2.32)$$

and the reduced global force vector,

$$\bar{\mathbf{f}} = \mathbf{H}^T [\mathbf{f} - \mathbf{M} \mathbf{g}]. \quad (2.33)$$

The time derivative of the second part of the state vector,  $\mathbf{q}^d$ , is obviously the first part of the state vector itself. The time derivative of the generalized kinematic coordinates,  $\mathbf{q}^k$ , as found in (2.21), can in general be expressed as

$$\dot{\mathbf{q}}^k = \mathbf{A}(\mathbf{q}, t) \dot{\mathbf{q}}^d + \mathbf{b}(\mathbf{q}, t), \quad (2.34)$$

where the matrix  $\mathbf{A}$  and the velocity vector  $\mathbf{b}$ , which represents the velocities of the rheonomic constraints, are given by

$$\mathbf{A} = -(\mathbf{V} \mathbf{F}_{,\mathbf{q}^k})^{-1} \mathbf{V} \mathbf{F}_{,\mathbf{q}^d}, \quad \text{and} \quad \mathbf{b} = -(\mathbf{V} \mathbf{F}_{,\mathbf{q}^k})^{-1} \mathbf{V} \mathbf{F}_{,t}. \quad (2.35)$$

Note in both expressions the presence of the inverse of the Jacobian (2.24).

We summarize by writing down the time derivative of the state vector or the state equations as

$$\frac{d}{dt} \begin{bmatrix} \dot{\mathbf{q}}^d \\ \mathbf{q}^d \\ \mathbf{q}^k \end{bmatrix} = \begin{bmatrix} \bar{\mathbf{M}}^{-1} \bar{\mathbf{f}} \\ \dot{\mathbf{q}}^d \\ \mathbf{A} \dot{\mathbf{q}}^d + \mathbf{b} \end{bmatrix} \quad (2.36)$$

### 2.4.2 Linearized Equations of Motion

To describe the small vibrations or motions which are superimposed on the non-linear rigid body motion we have to linearize the dynamical equations (2.36) in the undeformed state with respect to deformation mode coordinates of those elements we assume deformable and the generalized kinematic coordinates. The deformation mode coordinates are chosen to be the degrees of freedom  $\mathbf{q}^d$ . Linearization of the first part of the state equations (2.36), the reduced equations of motion (2.31), results in

$$\bar{\mathbf{M}} \Delta \ddot{\mathbf{q}}^d + \bar{\mathbf{C}} \Delta \dot{\mathbf{q}}^d + \bar{\mathbf{K}}^d \Delta \mathbf{q}^d + \bar{\mathbf{K}}^k \Delta \mathbf{q}^k = -\mathbf{f}^d, \quad (2.37)$$

where the prefix  $\Delta$  denotes a small increment. The case of additional forces  $\mathbf{f}_a^d$  as in (2.11) will not be considered here. The linearization is done in the undeformed state which is characterized by  $(\dot{\mathbf{q}}^d, \mathbf{q}^d, \mathbf{q}^k) = (\mathbf{0}, \mathbf{0}, \mathbf{q}_0^k)$ , where  $\mathbf{q}_0^k$  stands for the kinematic coordinates in the reference state.  $\bar{\mathbf{M}}$  is the reduced mass matrix as in (2.32),  $\bar{\mathbf{C}}$  is the velocity sensitivity matrix which contains terms resulting from damping and gyroscopic effects,  $\bar{\mathbf{K}}^d$  and  $\bar{\mathbf{K}}^k$  are the total stiffness matrices. Note that the variation of these kinematic coordinates gives rise to an extra stiffness term in comparison with the pure holonomic case (2.11). The forcing,  $-\mathbf{f}^d$ , on right-hand side of the equations results from the rigid body fundamental solution. In order to maintain the prescribed values for the deformations and the kinematic coordinates during this motion, additional forces have to be introduced in the right-hand side of the reduced equations of motion (2.31). The sum of the reduced forces has to be zero, as in

$$\mathbf{H}^T [\mathbf{f} - \mathbf{M}\mathbf{g}] + \mathbf{f}^d = 0, \quad (2.38)$$

from which the forces  $\mathbf{f}^d$  are found.

The matrices of the linearized equations are determined in the following way. First for all elements and nodes the contribution to the global stiffness matrix  $\mathbf{K}$  and the global velocity matrix  $\mathbf{C}$  are determined as

$$\mathbf{C}^e = -(\mathbf{f}^e)_{,\dot{\mathbf{x}}^e} \quad \text{and} \quad \mathbf{K}^e = (\mathbf{M}^e \ddot{\mathbf{x}}^e - \mathbf{f}^e)_{,\mathbf{x}^e}. \quad (2.39)$$

These global matrices having been determined, the matrices in the linearized equations are given by

$$\begin{aligned}\bar{\mathbf{C}} &= \mathbf{H}^T \mathbf{C} \mathbf{H} + \mathbf{H}^T \mathbf{M} \mathbf{g}_{,\dot{\mathbf{q}}^d}, \\ \bar{\mathbf{K}} &= [\bar{\mathbf{K}}^d \ \bar{\mathbf{K}}^k] = \mathbf{H}^T \mathbf{K} \mathbf{F}_{,\mathbf{q}} + \mathbf{H}_{,\mathbf{q}}^T [\mathbf{M} \ddot{\mathbf{x}} - \mathbf{f}] + \mathbf{H}^T [\mathbf{M} \mathbf{g}_{,\mathbf{q}} + \mathbf{C} \mathbf{v}_{,\mathbf{q}}].\end{aligned}\quad (2.40)$$

Note that all matrices are generally a function of time due to the non-linear rigid body motion. Linearization of the second part of equation (2.36) is trivial. The last part, the linearization of the rate of the generalized kinematic coordinates is derived from (2.34) as

$$\Delta \dot{\mathbf{q}}^k = \mathbf{A}(\mathbf{q}, t) \Delta \dot{\mathbf{q}}^d + \mathbf{B}^d(\mathbf{q}, t) \Delta \mathbf{q}^d + \mathbf{B}^k(\mathbf{q}, t) \Delta \mathbf{q}^k. \quad (2.41)$$

The  $\mathbf{B}$ -matrices express the sensitivity of the generalized kinematic velocities with respect to the generalized coordinates, and are given by

$$\mathbf{B}^d(\mathbf{q}, t) = \mathbf{b}_{,\mathbf{q}^d} \quad \text{and} \quad \mathbf{B}^k(\mathbf{q}, t) = \mathbf{b}_{,\mathbf{q}^k} \quad (2.42)$$

We conclude by summarizing the linearization of the state equations in matrix vector form as

$$\begin{bmatrix} \bar{\mathbf{M}} & \mathbf{0} & \mathbf{0} \\ \mathbf{0} & \mathbf{I} & \mathbf{0} \\ \mathbf{0} & \mathbf{0} & \mathbf{I} \end{bmatrix} \begin{bmatrix} \Delta \ddot{\mathbf{q}}^d \\ \Delta \dot{\mathbf{q}}^d \\ \Delta \dot{\mathbf{q}}^k \end{bmatrix} + \begin{bmatrix} \bar{\mathbf{C}} & \bar{\mathbf{K}}^d & \bar{\mathbf{K}}^k \\ -\mathbf{I} & \mathbf{0} & \mathbf{0} \\ -\mathbf{A} & -\mathbf{B}^d & -\mathbf{B}^k \end{bmatrix} \begin{bmatrix} \Delta \dot{\mathbf{q}}^d \\ \Delta \mathbf{q}^d \\ \Delta \mathbf{q}^k \end{bmatrix} = \begin{bmatrix} -\bar{\mathbf{f}}^d \\ \mathbf{0} \\ \mathbf{0} \end{bmatrix}. \quad (2.43)$$

The stability of a system in steady motion can be investigated by the homogeneous linearized state equation from (2.43). Under the usual assumption of an exponential motion with respect to time for the small variations  $(\Delta \dot{\mathbf{q}}^d, \Delta \mathbf{q}^d, \Delta \mathbf{q}^k)^T$  we end up with a characteristic equation for the unknown exponents. The stability of an equilibrium state, the case of zero steady motion as investigated by Bottema [4], corresponds to vanishing  $\mathbf{B}$ -matrices and evidently results in vanishing roots, as many as there are kinematic coordinates or non-holonomic constraints. An example of the stability analysis of a steady motion is the application to a swivel wheel, as presented in the chapter on special finite elements, in Section 3.5.2.



## Chapter 3

# Special Finite Elements

... ‘and what is the use of a book,’ thought Alice, ‘without pictures or conversation?’

(Lewis Carroll, *Alice’s Adventures in Wonderland*)

With the help of a rather limited number of element types it is possible to model in a finite element approach, a wide class of flexible multibody systems. Typical types of elements are beam, truss and hinge elements, while more specialized elements can be used to model joint connections, transmissions of motion or rolling contact. In this chapter an extension to the typical set is presented. These special finite elements are: the planar cylindrical bearing, the planar belt and pulley pair, the planar gear pair, the spatial hinge, and the disk rolling on an arbitrary surface, both in planar and spatial version. Every element type is illustrated by a suitable example problem.

### 3.1 Cylindrical Bearing

The planar cylindrical bearing element is very useful for the modelling of multibody systems having a compliant joint or joint clearance. Usually the relative displacements in the joint are small in comparison with the overall dimension of the mechanism. By the introduction of a bearing element in a joint the effect of these displacements on the kinematic and dynamic behaviour of the mechanism can be analysed.

The layout of a planar cylindrical bearing element is shown in Figure 3.1. The position and orientation of the sleeve are given by the coordinates  $x_p$  and  $y_p$  and the angle  $\beta_p + \beta_p^0$ , expressed in a global inertial system  $Oxy$ . For the

journal these are respectively  $x_q, y_q$  and  $\beta_q + \beta_q^0$ . The angles  $\beta_p^0$  and  $\beta_q^0$  represent the initial orientations of the sleeve and the journal. The bearing element,

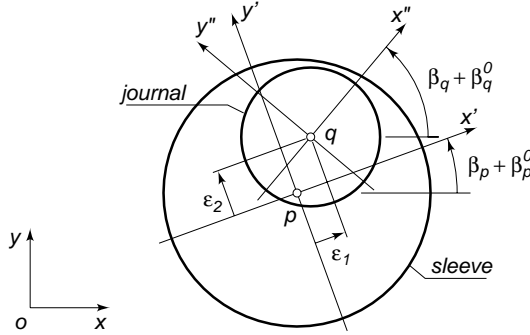


Figure 3.1: Planar cylindrical bearing element.

consisting of the journal and the sleeve, has 3 degrees of freedom as a rigid body, while the positions and orientations of the nodes, grouped together in a vector  $\mathbf{x}^T = (x_p, y_p, \beta_p, x_q, y_q, \beta_q)$ , represent 6 degrees of freedom. Hence the deformation of the element can be defined by 3 independent generalized strains, which are functions of the positions and orientations of the nodes  $p$  and  $q$ . We define these strains,  $\boldsymbol{\varepsilon} = \mathbf{D}(\mathbf{x})$ , as

$$\begin{aligned}\varepsilon_1 &= (x_q - x_p) \cos(\beta_p + \beta_p^0) + (y_q - y_p) \sin(\beta_p + \beta_p^0), \\ \varepsilon_2 &= (y_q - y_p) \cos(\beta_p + \beta_p^0) - (x_q - x_p) \sin(\beta_p + \beta_p^0), \\ \varepsilon_3 &= (\beta_q + \beta_q^0) - (\beta_p + \beta_p^0).\end{aligned}\quad (3.1)$$

The first generalized strain,  $\varepsilon_1$ , is the horizontal displacement of the journal relative to the moving frame of the sleeve. The second strain,  $\varepsilon_2$ , is the corresponding vertical displacement. The relative rotation of the journal with respect to the sleeve is the third generalized strain. A rotational joint without clearance can now be modelled by a bearing element with  $\varepsilon_1$  and  $\varepsilon_2$  set to zero and  $\varepsilon_3$  let free to deform. The first two generalized strains, the relative displacements in the joint, can also be very useful in the analysis of the effect of small joint clearance on the behaviour of a multibody system.

The dual quantities of the generalized strains  $\boldsymbol{\varepsilon}$ , are the generalized stresses  $\boldsymbol{\sigma}$ , and can be interpreted from the element equilibrium conditions  $\mathbf{f} = \mathbf{D}_{,\mathbf{x}}^T \boldsymbol{\sigma}$ . The first two generalized stresses  $\sigma_1$  and  $\sigma_2$  are the horizontal and the vertical bearing force with respect to the moving frame of the sleeve. The third stress,

$\sigma_3$ , is the torsion moment in the bearing. Each individual strain can be assumed either zero or non-zero, representing respectively the rigid and the deformable case. In the deformable case, or in the case of a lubricated bearing, a constitutive equation for  $\sigma$  has to be applied.

An example of the application of the planar cylindrical bearing element is the analysis of the slider-crank mechanism with joint clearance from Section 4.4.5. Another, more widespread application of the element with different types of constitutive behaviour, can be found in Chapter 5; it presents a study on the effect of joint clearance on the dynamic behaviour of mechanisms and machines.

### 3.2 Belt and Pulley Pair

The planar belt and pulley pair element consists of two pulleys with constant radius and one half, or open, belt as shown in Figure 3.2. The definition of an

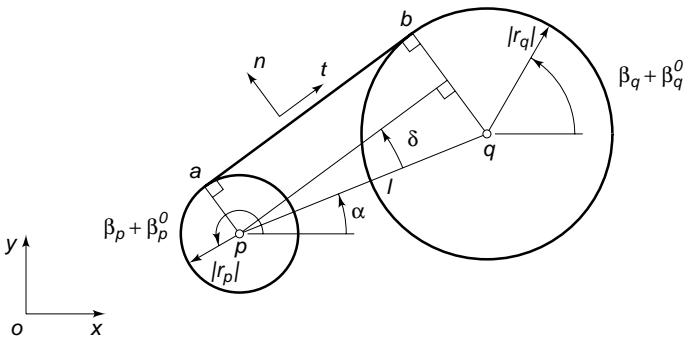


Figure 3.2: Planar belt and pulley pair element.

open belt makes it possible to create serpentine belt systems by putting the belt and pulley pair elements in series. The serpentine belt system can be closed by taking at the start and at the end of the serpentine belt the same nodal position, orientation, and pulley radii. The open belt configuration can also be looked upon as a straight cable running on and off two cable drums.

The configuration of the element is defined by the positions and orientations of the two pulleys and the initial belt length. The position and orientation of pulley  $p$  are given by the coordinates  $x_p$  and  $y_p$ , and the angle  $\beta_p + \beta_p^0$ , expressed in a global inertial system  $Oxy$ . For pulley  $q$  these are respectively  $x_q, y_q$  and  $\beta_q + \beta_q^0$ . The angles  $\beta_p^0$  and  $\beta_q^0$  describe the initial orientations of the pulleys.

The element, consisting of two pulleys and an inextensible belt, has 3 degrees of freedom as a rigid body, while the positions and orientations of the nodes, grouped together in a vector  $\mathbf{x}^T = (x_p, y_p, \beta_p, x_q, y_q, \beta_q)$ , represent 6 degrees of freedom. Hence the deformation of the element can be defined by 3 independent generalized strains. However, we only define one strain, the elongation of the belt between the two pulleys. The fixation, if needed, of the two remaining deformation modes, like for instance the fixation of the distance between  $p$  and  $q$  and a fixed orientation of pulley  $p$ , can be achieved by other construction elements. The belt is assumed to come into contact with pulley  $p$  at  $a$  and leave pulley  $q$  at  $b$  or vice versa, and we assume no slip. From this configuration two angles and one distance can be calculated, the angle  $\alpha$  between the centre line and the  $x$ -axis, the angle  $\delta$  between the belt and the centre line and the distance  $l$  between the two pulley centres, see Figure 3.2, as

$$\tan \alpha = \frac{y_q - y_p}{x_q - x_p}, \quad \sin \delta = \frac{r_q - r_p}{l}, \quad \text{and} \quad l = \sqrt{(x_q - x_p)^2 + (y_q - y_p)^2}. \quad (3.2)$$

The configuration for positive pulley radii  $r_p$  and  $r_q$  is shown in Figure 3.2, whereas a change of sign in the radii changes the configuration from upper to lower belt or with only one radius negative, to a cross-belt situation. With no slip, the rate of change of length of the belt between the pulleys, which is the velocity difference in the tangential direction  $t$  of the belt of point  $a$  and  $b$ , is

$$\dot{\varepsilon} = \cos(\alpha + \delta)(\dot{x}_q - \dot{x}_p) + \sin(\alpha + \delta)(\dot{y}_q - \dot{y}_p) - \dot{\beta}_q r_q + \dot{\beta}_p r_p. \quad (3.3)$$

If this generalized strain rate originates from a holonomic condition then the partial derivatives according to  $\dot{\varepsilon} = (\partial\varepsilon/\partial x_i)\dot{x}_i$  must be

$$\frac{\partial \varepsilon}{\partial x_i} = D_{,i} = (-\cos(\alpha + \delta), -\sin(\alpha + \delta), r_p, \cos(\alpha + \delta), \sin(\alpha + \delta), -r_q). \quad (3.4)$$

It is easily checked that the second order partial derivatives of  $\varepsilon$  are symmetric,  $\varepsilon_{,ij} = \varepsilon_{,ji}$  which is a sufficient proof that  $\varepsilon$  is a holonomic condition. The expression for  $\varepsilon$  can be found by partial integration of equation (3.4). In this way we come up with the following definition of the generalized strain for the belt and pulley pair element,

$$\varepsilon = \sqrt{(x_q - x_p)^2 + (y_q - y_p)^2 - (r_q - r_p)^2} + r_p \beta_p - r_q \beta_q + (r_q - r_p)(\alpha + \delta) - l_0^*. \quad (3.5)$$

The value of  $l_0^*$  is a constant determined in the initial configuration such that  $\varepsilon$  equals zero; it is a kind of initial belt length. In the generalized strain definition

of equation (3.5) we clearly distinguish the first part as the distance between point  $a$  and  $b$ ,

$$l_{ab} = \sqrt{(x_q - x_p)^2 + (y_q - y_p)^2 - (r_q - r_p)^2}. \quad (3.6)$$

The second part,  $r_p\beta_p - r_q\beta_q$ , is the change in belt length due to the rotation of the two pulleys. The last part,  $(r_q - r_p)(\alpha + \delta)$ , describes the effect on the belt length due to the change of orientation of the element as a whole at constant pulley orientation. The generalized strain from equation (3.5) is invariant under arbitrary rigid body motions, and it describes the amount of elongation in the non-slipping belt between the two pulleys.

The generalized stress  $\sigma$ , the dual of  $\dot{\varepsilon}$ , can be interpreted from the element equilibrium condition  $\mathbf{f} = D_{,\mathbf{x}}^T \sigma$ . With the nodal force vector  $\mathbf{f}^T = (F_{xp}, F_{yp}, M_p, F_{xq}, F_{yq}, M_q)$  written out in components as

$$\begin{pmatrix} F_{xp} \\ F_{yp} \\ M_p \\ F_{xq} \\ F_{yq} \\ M_q \end{pmatrix} = \begin{pmatrix} -\cos(\alpha + \delta) \\ -\sin(\alpha + \delta) \\ r_p \\ \cos(\alpha + \delta) \\ \sin(\alpha + \delta) \\ -r_q \end{pmatrix} \sigma, \quad (3.7)$$

the generalized stress  $\sigma$  is interpreted as the tensile force in the belt.

The usual linear relation between the physical stress and strain in the belt can be applied to the belt between the contact points  $a$  and  $b$  yielding for the generalized stress

$$\sigma = S\varepsilon, \quad \text{with} \quad S = EA/l_{ab}. \quad (3.8)$$

Here,  $E$  is the modulus of elasticity (Young's modulus),  $A$  is the area of cross-section and  $l_{ab}$  the length of the belt between the two contact points  $a$  and  $b$  according to equation (3.6). Note that with this constitutive model there is no conservation of energy in the belt system. The elastic energy from a deformed belt with finite length wound under tension on a pulley is lost when the belt is subsequent unwound under zero tension. If on the other hand the belt is wound undeformed under zero tension and next unwound under tension, energy is gained. For a serpentine belt system the model is approximately right but care should be taken in other cases.

The derivation of the consistent mass formulation for the flexible belt and pulley pair element is based on the elastic line concept. This means that rotational inertia of the cross-section is neglected and moreover only the longitudinal

vibration of the belt is taken into account. If we want to describe the lateral vibration of the belt extra deformation modes and consequently extra coordinates have to be taken into account. In the inertia contribution we can distinguish two parts, the mass of the belt wound at pulley  $p$  and at pulley  $q$ , and the belt between the contact points  $a$  and  $b$ . We start with the latter. The interpolation on the elastic line between  $a$  and  $b$  is now taken to be

$$\mathbf{r}(\xi) = (1 - \xi)\mathbf{x}_a + \xi\mathbf{x}_b, \quad (3.9)$$

where  $\xi$  is a normalized material co-ordinate along the elastic line,  $0 \leq \xi \leq 1$ . The inertia terms are obtained by equating the virtual power integral of the distributed inertia forces with the nodal inertia forces for arbitrary virtual velocity fields, yielding

$$-\rho A l_{ab} \int_0^1 (\delta \dot{\mathbf{r}} \cdot \ddot{\mathbf{r}}) d\xi = \delta \dot{\mathbf{x}} \cdot \mathbf{f}_{in}. \quad (3.10)$$

Note that  $\rho A l_{ab}$  stands for the total mass of the cable between the contact points  $a$  and  $b$ . The nodal inertia forces according to d'Alembert,  $\mathbf{f}_{in}$ , are usually written as

$$\mathbf{f}_{in} = -(\mathbf{M}\ddot{\mathbf{x}} + \mathbf{h}), \quad (3.11)$$

where  $\mathbf{h}$  originates from the convective inertia terms. The velocity of a material point of the belt on the elastic line is according to (3.9) given by

$$\dot{\mathbf{r}}(\xi) = (1 - \xi)\dot{\mathbf{x}}_a + \xi\dot{\mathbf{x}}_b, \quad (3.12)$$

where the velocities of the belt at the contact points  $a$  and  $b$  expressed in terms of the nodal point velocities are determined by

$$\begin{aligned} \dot{\mathbf{x}}_a &= \dot{\mathbf{x}}_p - \dot{\beta}_p r_p \mathbf{e}_t \\ \dot{\mathbf{x}}_b &= \dot{\mathbf{x}}_q - \dot{\beta}_q r_q \mathbf{e}_t, \end{aligned} \quad (3.13)$$

with the unit tangent belt direction,  $\mathbf{e}_t$ , given by

$$\mathbf{e}_t^T = (\cos(\alpha + \delta), \sin(\alpha + \delta)). \quad (3.14)$$

From these results the accelerations  $\ddot{\mathbf{r}}(\xi)$  can be calculated and the integral (3.10) can be evaluated. Equating the result with (3.11) results in a mass matrix for the belt as

$$\mathbf{M}_{belt} = \frac{\rho A l_{ab}}{6} \begin{pmatrix} 2 & 0 & -2cr_p & 1 & 0 & -cr_q \\ & 2 & -2sr_p & 0 & 1 & -sr_q \\ & & 2r_p^2 & -cr_p & -sr_p & r_p r_q \\ & & & 2 & 0 & -2cr_q \\ & & & & 2 & -2sr_q \\ & & \text{sym.} & & & 2r_q^2 \end{pmatrix}, \quad (3.15)$$

and convective inertia forces

$$\mathbf{h}_{belt} = \frac{\rho A}{6} \begin{pmatrix} -sv_n(2r_p\dot{\beta}_p + r_q\dot{\beta}_q) \\ cv_n(2r_p\dot{\beta}_p + r_q\dot{\beta}_q) \\ 0 \\ -sv_n(r_p\dot{\beta}_p + 2r_q\dot{\beta}_q) \\ cv_n(r_p\dot{\beta}_p + 2r_q\dot{\beta}_q) \\ 0 \end{pmatrix}. \quad (3.16)$$

Here we have used the shorthand notation

$$s = \sin(\alpha + \delta), \quad \text{and} \quad c = \cos(\alpha + \delta), \quad (3.17)$$

and the component of the velocity of node  $q$  with respect to node  $p$  normal to the direction of the belt has been indicated as

$$v_n = s(\dot{x}_q - \dot{x}_p) - c(\dot{y}_q - \dot{y}_p). \quad (3.18)$$

The next step is the mass contribution of the belt wound on the two pulleys. Let us assume that in the initial state the amount of belt wound on pulley  $p$  measured from contact point  $a$ , counterclockwise, has a total length of  $r_p\kappa_p$  and for pulley  $q$  measured from contact point  $b$ , clockwise, a length of  $r_q\kappa_q$ . By using the same approach as in equation (3.10) this results for the pulleys  $p$  and  $q$  in a mass matrix

$$\mathbf{M}_{pulleys} = \rho A \begin{pmatrix} r_p\phi_p & 0 & -r_p^2cs_p & 0 & 0 & 0 \\ & r_p\phi_p & -r_p^2ss_p & 0 & 0 & 0 \\ & & r_p^3\phi_p & 0 & 0 & 0 \\ & & & -r_q\phi_q & 0 & r_q^2cs_q \\ & & & & -r_q\phi_q & r_q^2ss_q \\ & & \text{sym.} & & & -r_q^3\phi_q \end{pmatrix}, \quad (3.19)$$

and convective inertia forces

$$\mathbf{h}_{pulleys} = \rho A \begin{pmatrix} r_p^2ss_p\dot{\beta}_p^2 \\ -r_p^2cs_p\dot{\beta}_p^2 \\ 0 \\ -r_q^2ss_q\dot{\beta}_q^2 \\ r_q^2cs_q\dot{\beta}_q^2 \\ 0 \end{pmatrix}, \quad (3.20)$$

where

$$\begin{aligned}\phi_i &= \beta_i + \kappa_i - (\alpha + \delta) + (\alpha_0 + \delta_0), \\ cs_i &= 2 \cos(\phi_i/2 + (\alpha + \delta)) \sin(\phi_i/2), \\ ss_i &= 2 \sin(\phi_i/2 + (\alpha + \delta)) \sin(\phi_i/2), \quad i = (p, q).\end{aligned}\tag{3.21}$$

The orientation of the belt in the initial state is determined by  $\alpha_0 + \delta_0$ . The total mass matrix and convective inertia forces for the belt and pulley pair element are given by the sums  $\mathbf{M} = \mathbf{M}_{belt} + \mathbf{M}_{pulleys}$  and  $\mathbf{h} = \mathbf{h}_{belt} + \mathbf{h}_{pulleys}$ . Additional mass and inertia of the pulleys can be added to the system as lumped mass and inertia in the nodes. An alternative approach for the derivation of the inertia terms which makes use of the kinetic energy expression for the element can be found in Appendix A starting on page 109.

Note the effect of the individual mass matrices of the pulleys on the system mass matrix in the case of a serpentine belt and pulley system. Under the assumption of equal radii  $r$  and equal angle of revolution  $\phi$ , pulley  $q$  of element  $i$  gives a negative contribution on the main diagonal and pulley  $p$  from element  $i + 1$  has positive diagonal terms. The sum  $-r_q\phi_q + r_p\phi_p$ , which appears on the diagonal of the system mass matrix, is constant. Mass is created nor destroyed.

### 3.2.1 Cable Drum

The changing mass distribution in a belt and pulley pair system is illustrated by the rolling motion of an unwinding cable drum, see Figure 3.3. On a drum with radius  $r$ , a cable with mass  $m$  per revolution is wound. The drum can roll over a

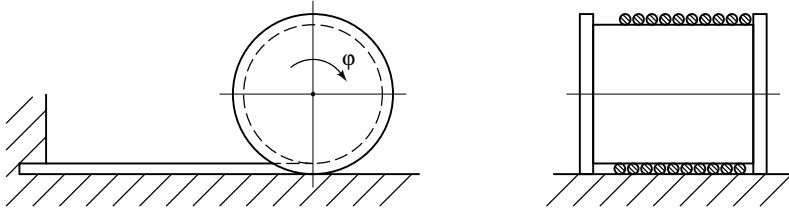


Figure 3.3: Rolling and unwinding cable drum.

horizontal plane while one end of the cable is fixed to the ground, resulting in the unwinding of the cable. Given an initial speed, the drum will lose mass and gain speed. To illustrate the effect of the changing mass distribution on the motion of the drum we neglect the mass of the drum and we do not consider gravity. The cable is modelled as inextensible. Under these assumptions the system is

energy conservative since the belt touches the ground with zero velocity during the unwinding motion.

The system is modelled by one belt and pulley pair element, with  $r_p = 0$  and  $r_q = -r$ . Node  $p$  is fixed in position and orientation while node  $q$  is only restricted in the vertical direction. Then the remaining coordinates, the horizontal position  $x$  of the drum centre and the rotation  $\varphi$  of the drum are constrained by the inextensible cable, which takes in this case the simple form of  $x = r\varphi$ . As a degree of freedom we take the angle  $\varphi$ . In the initial configuration the drum is wound with 10 turns of cable and the initial angular velocity of the drum is  $\omega_0$ .

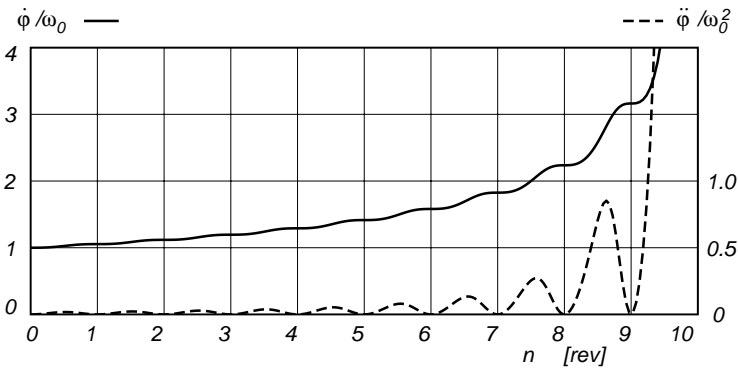


Figure 3.4: Angular velocity  $\dot{\varphi}$  and angular acceleration  $\ddot{\varphi}$  of the cable drum during unwinding as a function of the number of revolutions  $n$  of the drum, with initially 10 turns of cable on the drum and an initial angular speed of  $\omega_0$ .

The ever increasing angular velocity of the drum during unwinding of the cable is shown in Figure 3.4. At the end of the 10th turn of the drum its angular velocity goes to infinity since the drum itself has no mass. This result from the model can easily be checked with the conservation of kinetic energy of the system. Consider an infinitesimal part  $dm$  of the cable located at the angle  $\theta$ , counterclockwise and starting at the contact point. The square of the velocity of this particle is

$$v^2 = 2(\dot{\varphi}r)^2(1 - \cos \theta). \quad (3.22)$$

Summing up the kinetic energy contribution  $1/2v^2dm$  of all particles from  $\theta = 0$

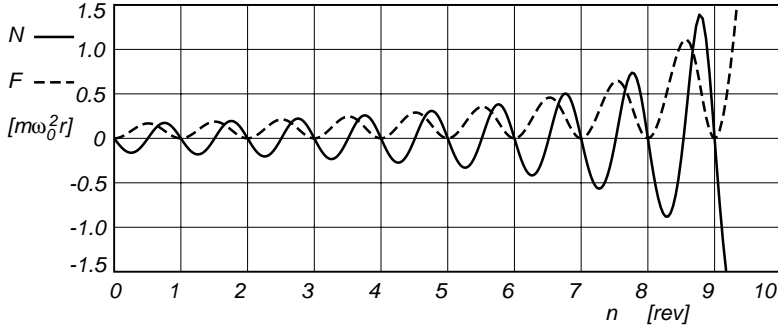


Figure 3.5: Cable tension  $F$  and normal force  $N$  exerted by the ground on the system during unwinding of the cable as a function of the number of revolutions  $n$  of the drum, with initially 10 turns of cable on the drum and an initial angular speed of  $\omega_0$ .

to  $\theta = 20\pi - \varphi$ , results in the total kinetic energy  $T$  of the system as

$$T = \left(10 - \frac{\varphi}{2\pi} + \frac{1}{2\pi} \sin \varphi\right) m r^2 \dot{\varphi}^2. \quad (3.23)$$

The angular acceleration of the drum in the model,  $\ddot{\varphi}$ , which is shown in the same figure, oscillates with increasing amplitude and is zero after each full turn. The forces exerted by the ground on the cable and the drum in the model are shown in Figure 3.5. The cable tension  $F$  exhibits of course the same behaviour as the angular acceleration while the normal force  $N$ , exerted by the ground on the drum, oscillates with ever increasing amplitude around zero. The negative values of this contact force can only be achieved by a slotted guide way or a gravitational pre-stress.

### 3.3 Gear Pair

An interesting thing happens when one of the radii of the belt and pulley pair element is negative, for instance  $r_p$ , and the other radius is positive. This configuration, which is shown in Figure 3.6, is a model of a spur gear pair with involute teeth. The radii of the base circles of the involute tooth profiles are given by  $|r_p|$  and  $|r_q|$ . The line of action or contact, is from  $a$  to  $b$  and the pressure angle  $\alpha_n$  is  $\pi/2 - \delta$ .

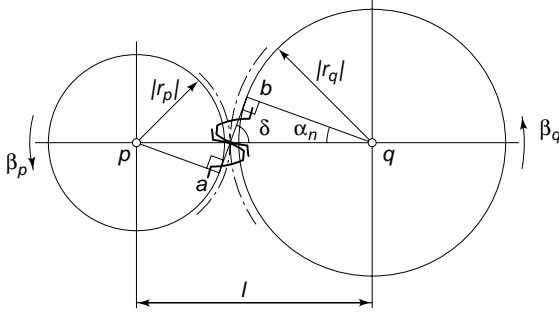


Figure 3.6: Spur gear pair with involute teeth.

For the generalized strain  $\varepsilon$ , which represents the deformation of the engaged teeth, we take the change of distance between point  $a$  and  $b$ . This definition of the generalized strain is the same as in the belt and pulley pair element, equation (3.5). In gear design we are used to the concept of transmission ratio  $i$ , pressure angle  $\alpha_n$  and centre distance  $l$ . From these parameters the two radii  $r_p$  and  $r_q$  can be calculated as,

$$r_p = \pm \frac{l \cos \alpha_n}{1 + i}, \quad \text{and} \quad r_q = -ir_p. \quad (3.24)$$

The generalized stress  $\sigma$  is the normal tooth force working along the line of action  $a$ - $b$ . If a tensile tooth force is found during the simulation, the sign of the pressure angle can be changed to obtain a compressive contact force. The line of action is then mirrored with respect to the centre line. The sign of the pressure angle can be changed by changing both signs of the base circle radii. The nodal forces expressed by the element equilibrium equations  $\mathbf{f} = D_{,x}^T \sigma$  (3.7), with the gear parameters  $i$  and  $\alpha_n$  from (3.24), and in the case of a horizontal centre line ( $\alpha = 0$ ), are given by

$$\begin{pmatrix} F_{xp} \\ F_{yp} \\ M_p \\ F_{xq} \\ F_{yq} \\ M_q \end{pmatrix} = \begin{pmatrix} -\sin \alpha_n \\ -\cos \alpha_n \\ r_p \\ \sin \alpha_n \\ \cos \alpha_n \\ ir_p \end{pmatrix} \sigma. \quad (3.25)$$

In these expressions we recognize the driving torques  $\sigma r_p$  and  $i\sigma r_p$ , and the horizontal force with magnitude  $\sigma \sin \alpha_n$ , which push the wheels apart. In the

case of deformable teeth, the stress-strain relation can for instance be described by a Hertzian contact model with an elliptic contact area.

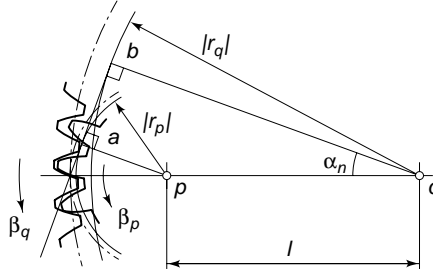


Figure 3.7: Spur gear pair with external (pinion) and internal (annulus) teeth.

Not only spur gear with external teeth but also internal gear, as shown in Figure 3.7, can be modelled by choosing the appropriate  $r_p, r_q$  and  $l$ . Note that in the general case of a pinion and annulus pair, as shown in Figure 3.7, the transmission ratio  $i$  is negative, and the base circle radii have the same sign.

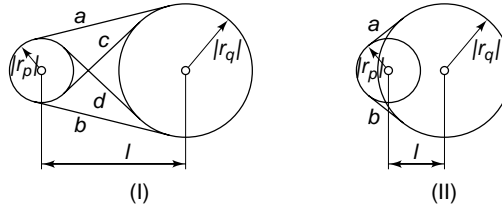


Figure 3.8: Belt drive and gear pair configurations, as summarized in Table 3.1.

	$r_p$	$r_q$	(I): $ r_p  +  r_q  < l$	(II): $ r_p - r_q  < l$
a	+	+	Belt	Internal Gear
b	-	-	Belt	Internal Gear
c	-	+	Belt or External Gear	-
d	+	-	Belt or External Gear	-

Table 3.1: Belt drive and gear pair configurations, as shown in Figure 3.8.

Potential belt drive and gear pair configurations are shown in Figure 3.8 and summarized in Table 3.1. The combination where one base or pulley circle is

completely enclosed by the other, as is the case for  $|r_q - r_p| > l$ , represents no physical belt drive or gear pair.

The mass and inertia of the individual gears can be added to the system as lumped mass and inertia in the nodes.

### 3.3.1 Application to a Step-Dwell Mechanism

As an example of the application of the belt and pulley pair and the gear pair element we will analyse the step-dwell mechanism with tooth belt as described by Rankers [61]. This mechanism has the advantage of a large displacement between two dwells in comparison with the overall dimension of the construction. The mechanism, which is shown in Figure 3.9, consists of a serpentine tooth

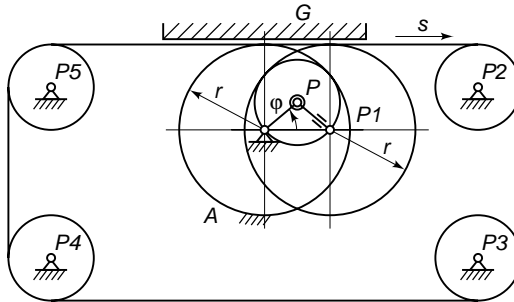


Figure 3.9: Step-dwell mechanism with tooth belt.

belt running over five pulleys  $P1$  to  $P5$ , driven by an isosceles slider-crank mechanism. The slider-crank mechanism is materialized by its dual form, a hypocycloidal gear pair with a transmission ratio of  $i = 2$ . The annulus  $A$ , with pitch radius  $r$ , is fixed and the centre path of the pinion  $P$ , with pitch radius  $r/2$ , is generated by a crank. The driven pulley  $P1$ , with radius  $r$ , is rigidly attached to the pinion in the imaginary slider position, in which manner it will move back and forth while rotating. The remaining four pulleys,  $P2$  to  $P5$  with radii  $r/2$ , are hinged to the base. A fixed guide way  $G$  prevents the tooth belt from disengaging. The tooth belt is assumed to be inextensible.

As a first result of the analysis, the belt displacement  $s$  as a function of the crank angle  $\varphi$  is shown in Figure 3.10a. Note the rest in the belt motion at  $\varphi = 90^\circ$  and the large displacement,  $2\pi r$ , after one crank revolution.

Secondly, the driving torque  $M$  and the normal tooth force  $\sigma$  in the gearing are shown in Figure 3.10b, in the case where the mechanism is driven by a

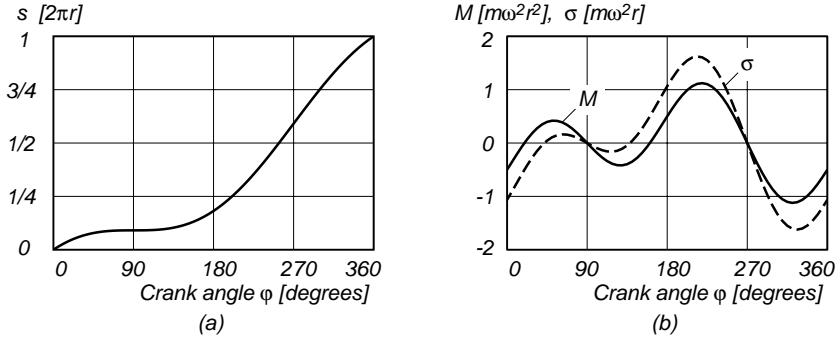


Figure 3.10: Belt displacement  $s$  (a), and crank driving torque  $M$  and normal tooth force  $\sigma$  in the gearing (b), as a function of the crank angle  $\varphi$  for a step-dwell mechanism.

constant angular velocity of  $\dot{\varphi} = \omega$ . The pinion and pulleys are assumed to be solid disks with equal thickness and density. The reference mass of pulley  $P1$  with radius  $r$  is  $m$ , whereas the pinion  $P$  and the pulleys  $P2$  to  $P5$  have radius  $r/2$  and consequently a mass of  $m/4$ . The moments of inertia about the mass centre are respectively  $1/2mr^2$  and  $1/32mr^2$ . The hypocycloidal gear pair has a pressure angle of  $\alpha_n = 20^\circ$ , and the tooth belt is assumed massless. The inextensible serpentine belt with fixed positioned pulleys  $P2$  to  $P5$  is a statically indeterminate system. The redundant constraint is removed by releasing one belt and pulley pair element, for instance the belt between pulley  $P3$  and  $P4$ .

### 3.4 Spatial Hinge

Whereas in the planar case a cylindrical joint between two elements can be established by those elements having one position node in common and having different orientations at that node, this is not possible in the spatial case. We would end up with a spherical joint which has three independent relative rotations. There is need for a spatial cylindrical joint which can describe large relative rotation, the hinge element.

The description of orientation in space, to be precise, the parameterizations of the three by three rotation matrix  $\mathbf{R}$ , has been given a long and intensive study by many authors over the last centuries. The choice of Euler parameters [5] seems very fruitful, they show no singularity and the rotation matrix

is a homogeneous quadratic function in the parameters. According to Euler's theorem on finite rotation, a rotation in space can always be described by a rotation along a certain axis over a certain angle. With the unit vector  $\mathbf{e}_\mu$  representing the axis and the angle of rotation  $\mu$ , right-handed positive, the four Euler parameters  $q = (q_0, q_1, q_2, q_3)$  can be interpreted as

$$q_0 = \cos(\mu/2) \quad \text{and} \quad \mathbf{q} = (q_1, q_2, q_3)^T = \sin(\mu/2)\mathbf{e}_\mu. \quad (3.26)$$

These four parameters are dependent and satisfy the constraint equation

$$q_0^2 + \mathbf{q} \cdot \mathbf{q} = 1. \quad (3.27)$$

Such a constraint is added to the system, for every spatial node, with a deformation parameter

$$\varepsilon_q = q_0^2 + \mathbf{q} \cdot \mathbf{q} - 1, \quad (3.28)$$

and putting this deformation equal to zero. Euler parameters are, due to their unit length defined by

$$|q| = \sqrt{q_0^2 + q_1^2 + q_2^2 + q_3^2}, \quad (3.29)$$

a special case of quaternions; they are unit quaternions. The Euler parameters for successive rotations are given by the quaternion product of the Euler parameters describing the individual rotations. The properties of quaternions and its calculus together with the application to finite rotations, as in the case of Euler parameters, and the derivation of the equations of motion for the rotation of a rigid body in terms of Euler parameters, is treated in Appendix B. Some results will be repeated here.

The hinge element describes the relative rotation between two spatial rotational nodes  $p$  and  $q$ . This element can be used to model a cylindrical joint between two parts. For this element, there are six independent nodal coordinates and three rigid body motions, so three independent deformations can be defined. If the rotations of the two nodes are described by means of the Euler parameters  $p = (p_0, \mathbf{p})$  and  $q = (q_0, \mathbf{q})$ , with the unit quaternion properties  $|p| = 1$  and  $|q| = 1$ , the relative rotation of node  $q$  with respect to node  $p$  can be described by the Euler parameters  $r = (r_0, \mathbf{r})$ . The sequence of rotation, first with  $r$  and then with  $p$ , is expressed in terms of the quaternion product, denoted by 'o', as

$$p \circ r = q. \quad (3.30)$$

The quaternion product is defined in terms of a combination of scalar and vector products as

$$p \circ r = (p_0 r_0 - \mathbf{p} \cdot \mathbf{r}, p_0 \mathbf{r} + r_0 \mathbf{p} + \mathbf{p} \times \mathbf{r}). \quad (3.31)$$

Note that this product is non-commutative. With the adjoint Euler parameters  $\bar{p} = (p_0, -\mathbf{p})$ , and the knowledge that  $\bar{p} \circ p = (1, \mathbf{0})$  is the unit element, the relative rotation  $r$  can be written as

$$r = \bar{p} \circ q. \quad (3.32)$$

These are the relative rotations expressed in components with respect to a global  $Oxyz$  reference frame. Usually the hinge is initially oriented according to a local reference frame  $(\mathbf{e}_x, \mathbf{e}_y, \mathbf{e}_z)$ . The Euler parameters expressed in this frame are given by

$$s = (s_0, \mathbf{s}) = (r_0, \mathbf{r} \cdot \mathbf{e}_x, \mathbf{r} \cdot \mathbf{e}_y, \mathbf{r} \cdot \mathbf{e}_z). \quad (3.33)$$

The three generalized strains of the hinge element are defined as

$$\begin{aligned} \varepsilon_1 &= 2 \arctan (s_1/s_0), \\ \varepsilon_2 &= 2(s_0 s_2 - s_1 s_3), \\ \varepsilon_3 &= 2(s_1 s_2 + s_0 s_3). \end{aligned} \quad (3.34)$$

If we use the hinge to model a cylindrical joint,  $\varepsilon_1$  represents the large relative rotation along the joint axis  $\mathbf{e}_x$ , and  $\varepsilon_2$  and  $\varepsilon_3$  represent the bending  $\psi$  of the joint axis with  $\sin \psi = \sqrt{\varepsilon_2^2 + \varepsilon_3^2}$  in a plane perpendicular to the joint axis. The relative rotation can be thought to be built up from two successive rotations. First, a rotation about the local  $\mathbf{e}_x$  axis over an angle  $\varphi$  and then a rotation over an angle  $\psi$  about a line perpendicular to the  $\mathbf{e}_x$  axis. This line can be denoted by the unit vector  $\mathbf{n} = (0, n_y, n_z)$  expressed in components along the rotated  $p$ -frame. The Euler parameters for the first rotation are given by  $u = (\cos(\varphi/2), \sin(\varphi/2), 0, 0)$  and for the second rotation by  $v = (\cos(\psi/2), 0, n_y \sin(\psi/2), n_z \sin(\psi/2))$ . The relative rotation of the hinge is given by

$$s = v \circ u = \begin{pmatrix} \cos(\psi/2) \cos(\varphi/2) \\ \cos(\psi/2) \sin(\varphi/2) \\ n_y \sin(\psi/2) \cos(\varphi/2) + n_z \sin(\psi/2) \sin(\varphi/2) \\ -n_y \sin(\psi/2) \sin(\varphi/2) + n_z \sin(\psi/2) \cos(\varphi/2) \end{pmatrix}. \quad (3.35)$$

From this relative rotation the generalized deformations according to equations (3.34) are calculated as  $\varepsilon_1 = \varphi$ , the rotation along the hinge axis, and  $\varepsilon_2 = n_y \sin \psi$  and  $\varepsilon_3 = n_z \sin \psi$ , the bending of the joint axis. It is interesting to see that a bended hinge can still rotate over an arbitrary angle.

The generalized stresses  $\boldsymbol{\sigma}$  can be identified as the joint moment  $\sigma_1$  along the joint axis and the bending moment  $(0, \sigma_2, \sigma_3)$  perpendicular to the joint axis.

### 3.4.1 Application to a Cardan Joint

An application of the hinge element is the Cardan joint. This joint, also known as Hooke’s joint or cross-type universal joint, has been used as a shaft coupling

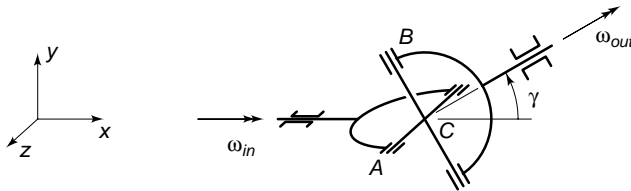


Figure 3.11: Cardan joint with an angular misalignment  $\gamma$  in the  $xy$ -plane.

in a wide range of machinery, which include locomotive as well as automotive drive lines. A drive line connected by a Cardan joint may exhibit torsional oscillations due to fluctuating angular velocity ratios, which are inherent to the system.

Figure 3.11 shows a one-degree-of-freedom shaft system incorporating a Cardan joint with an angular misalignment  $\gamma$  in the  $xy$ -plane. A straightforward model of the mechanism with four sequential hinges is shown in Figure 3.12a. The first hinge, marked *in*, describes the rotation of the input axle with respect

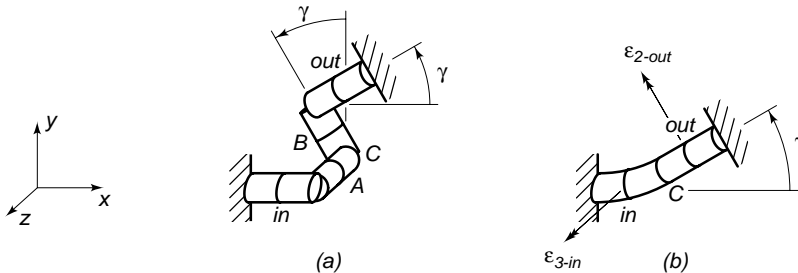


Figure 3.12: A straightforward (a) and an alternative (b) finite element model of a Cardan joint with an angular misalignment  $\gamma$  in the  $xy$ -plane.

to the inertia frame. The relative rotation of the cross  $ACB$  with the input and the output yoke is modelled by the hinges  $A$  and  $B$ . The rotation of the output shaft is modelled by the hinge marked *out*. The rotations of the hinges  $A$ ,  $B$

and *out* are released in their principal joint direction.

An alternative model of the mechanism with only two flexible hinges is shown in Figure 3.12*b*. The bending deformation of the input hinge along the local  $z$ -axis,  $\varepsilon_{3-in}$ , is released and takes over the function of hinge *A* from model *a*. Hinge *B* is replaced by the released bending deformation of the output hinge along the local  $y$ -axis,  $\varepsilon_{2-out}$ . The motion of the cross *ACB* is described by the coordinate frame in *C*. Since the hinge deformations are expressed in the principal directions of the frame attached to the first node of the element, the first node for both the input and the output hinge is in *C*.

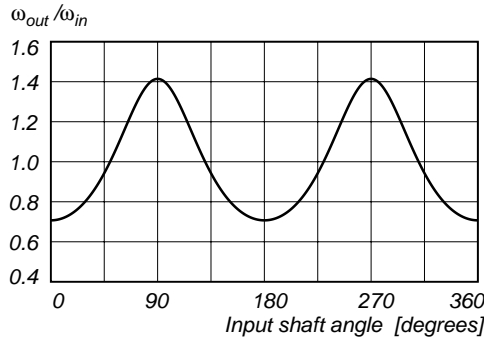


Figure 3.13: Angular velocity ratio  $\omega_{out}/\omega_{in}$  as a function of the input shaft angle for a Cardan joint with an angular misalignment of  $\gamma = 45^\circ$ .

The angular velocity ratio,  $\omega_{out}/\omega_{in}$ , for this last model is shown in Figure 3.13, and corresponds fully with the results as obtained for the straightforward model with four hinges. The joint rotations for the hinges *A* and *B*, representing the rotation of the cross with respect to the input and the output yoke, is shown in Figure 3.14*a*. The corresponding bending strains from the alternative model are shown in Figure 3.14*b*, and, according to the element description from the previous section, are equal to the sine of the joint rotations in the hinges *A* and *B*.

### 3.5 Two-Dimensional Wheel

The two-dimensional finite wheel element is a model of an infinitesimally thin disk with constant radius  $r$  standing upright on a horizontal plane. The position and orientation of the wheel can be described by the position of the centre of

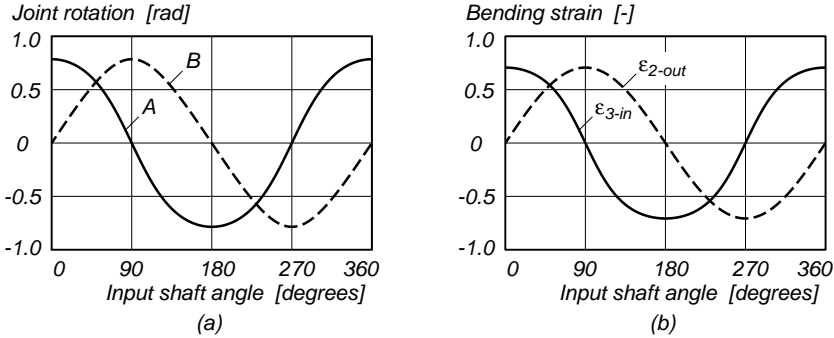


Figure 3.14: Joint rotations (a) of hinge  $A$  and  $B$  as in model  $a$  and bending strains (b) of the input and output shaft for model  $b$  as a function of the input shaft angle of a Cardan joint with an angular misalignment of  $\gamma = 45^\circ$ .

the wheel axis  $\mathbf{x}_c = (x_c, y_c)$ , the orientation angle  $\beta$  of the wheel axle and the rotation angle  $\gamma$  about the wheel axle. In the case of pure rolling, we need four

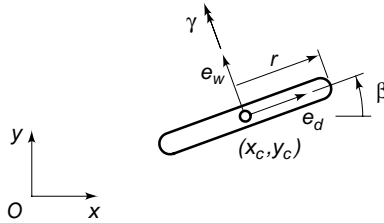


Figure 3.15: Two-dimensional wheel element.

coordinates to describe the position and orientation, while the contact condition imposes two non-holonomic constraints on the velocities. Hence the separate element has two degrees of freedom. The non-holonomic conditions will be described in terms of zero slip. In this way we can easily treat the case of a skidding or slipping wheel by releasing the non-holonomic constraints. With the rotated unit vectors  $\mathbf{e}_w$  in the direction of the wheel axle and  $\mathbf{e}_d$  in the driving direction as described by the transformation from body fixed frame to inertia frame as in  $\mathbf{e} = \mathbf{R}(\beta)\bar{\mathbf{e}}$ , where the rotation matrix is given by

$$\mathbf{R}(\beta) = \begin{pmatrix} \cos \beta & -\sin \beta \\ \sin \beta & \cos \beta \end{pmatrix}, \quad (3.36)$$

the slips are defined as

$$\begin{aligned} s_1 &= (\mathbf{e}_d)^T \dot{\mathbf{x}}_c - \dot{\gamma}r \\ s_2 &= (\mathbf{e}_w)^T \dot{\mathbf{x}}_c \end{aligned} \quad (3.37)$$

The first,  $s_1$ , is the longitudinal slip and the second,  $s_2$ , is the lateral one. The slip is in general a function of the position and orientation of the wheel and linear in the velocity. If the coordinates which describe the position and orientations are grouped together in a vector  $\mathbf{x}^T = (x_c, y_c, \beta, \gamma)$ , and the vector of slips is denoted by  $\mathbf{s}$ , the expressions for the slip can be written symbolically as

$$\mathbf{s} = \mathbf{V}(\mathbf{x})\dot{\mathbf{x}}. \quad (3.38)$$

Pure rolling is described by zero slips,  $\mathbf{s} = \mathbf{0}$ .

The dual quantities of the slips  $\mathbf{s}$  are the generalized forces  $\boldsymbol{\lambda}$ . They are defined by the balance of the external and internal virtual power of the element. The external virtual power is given by  $\mathbf{f}^T \delta \dot{\mathbf{x}}$  with the nodal force vector  $\mathbf{f}^T = (F_{x_c}, F_{y_c}, M_\beta, M_\gamma)$  while the internal virtual power is defined as  $\boldsymbol{\lambda}^T \delta \mathbf{s}$ . Equilibrium is expressed by the balance of these two,

$$\mathbf{f}^T \delta \dot{\mathbf{x}} = \boldsymbol{\lambda}^T \delta \mathbf{s}, \quad (3.39)$$

for arbitrary variations  $\delta \dot{\mathbf{x}}$  and corresponding variation of the slip components (3.38) and the equilibrium conditions become

$$\mathbf{f} = \mathbf{V}^T \boldsymbol{\lambda}. \quad (3.40)$$

From these equations the generalized forces  $\lambda_1$  and  $\lambda_2$  can be interpreted as the longitudinal and the lateral contact forces. In the case of longitudinal slip and/or lateral slip, any type of constitutive behaviour of the form  $\boldsymbol{\lambda} = \boldsymbol{\lambda}(\mathbf{s})$  can be applied.

### 3.5.1 Application to a Planimeter

A kinematic application of the planar wheel element is the Von Amsler (1854) polar planimeter. This measuring instrument can be used to determine the area enclosed by a contour and has found its application in major industry. This device, among many other mathematical instruments, is treated in the excellent book by Meyer zur Capellen [50]. The mathematical treatment of the non-holonomic aspects of such kinematic integrating mechanisms can be found for example in the works of Neřmark and Fufaev [55].

The polar planimeter, Figure 3.16, consists of three major parts; the pole rod  $PQ$  with fixed pole  $P$ , the moving arm  $MQF$  with pointer  $F$ , and the measure wheel attached perpendicular to the arm in  $M$ . The wheel can slide in the lateral direction but rolls without slipping in the longitudinal direction. To

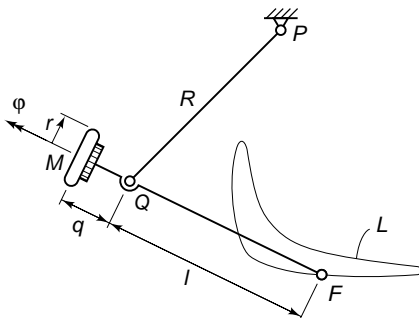


Figure 3.16: Polar planimeter.

measure the area enclosed by the contour  $L$ , for example an indicator diagram of a two-stroke cycle in a diesel engine as shown in Figure 3.16, one must guide the pointer  $F$  around the contour  $L$ . The rotation,  $\varphi$ , of the measure wheel along the wheel axis is proportional to the enclosed area and can be read off the drum attached to the wheel. If the pole  $P$  lies outside the contour  $L$ , which is usually the case, then the enclosed area  $A$  is given by

$$A = lr\varphi, \quad (3.41)$$

with moving arm length  $l$  and measure wheel radius  $r$ . When the pole lies within the contour we have to add a circular area with radius  $g$  which is not indicated by the measure wheel, in which case the desired area is obviously

$$A = lr\varphi + \pi g^2. \quad (3.42)$$

The radius  $g$  is the distance from the pole  $P$  to the pointer  $F$  in the configuration where the line  $PM$  is perpendicular to the rotation axis  $FM$  of the wheel. If the planimeter is now rotated as a rigid body around the pole, the measure wheel will not rotate. In this arrangement the square of the radius  $g$  is given by

$$g^2 = R^2 + l^2 + 2lq. \quad (3.43)$$

The finite element model of the planimeter consists of a rigid truss element, two rigid beam elements ( $QF$  and  $QM$ ), and a wheel element. The three independent coordinates of the system are the horizontal and vertical position  $x$  and  $y$  of the pointer  $F$ , and the rotation,  $\varphi$ , of the wheel. There is one non-holonomic condition; the wheel is assumed to roll without slipping in the longitudinal direction,  $s_1 = 0$ , while the lateral slip constraint,  $s_2$ , is released (3.37). Obviously the system has two degrees of freedom,  $x$  and  $y$ , and one kinematic coordinate,  $\varphi$ .

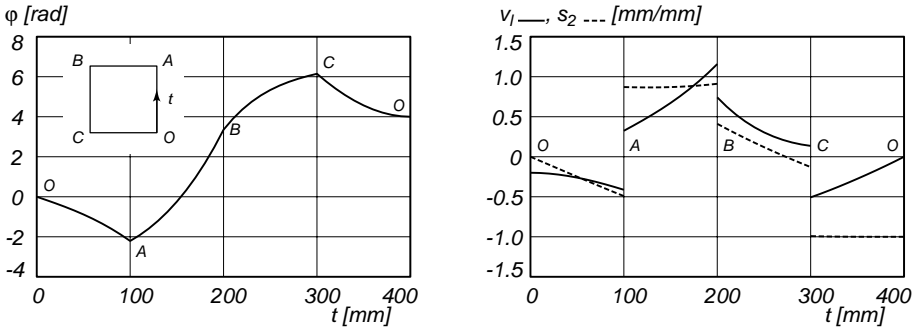


Figure 3.17: Rotation  $\varphi$  of the planimeter measure wheel as a function of the travelled distance  $t$  along the contour of the square  $OABC$ , left figure, and longitudinal rate,  $v_l = r d\varphi/dt$ , of the wheel centre and lateral slip of the wheel,  $s_2$ , as a function of the contour distance  $t$ , right figure.

As an example we will measure the area of a square  $OABC$  of  $100 \times 100$  [mm]. The dimensions of the mechanism, see Figure 3.16, are a pole length of  $R = 200$  [mm], a measure arm with  $l = 200$  [mm], and a wheel with radius  $r = 12.5$  [mm] at a distance  $q = 40$  [mm] from the pole hinge  $A$ . In the initial configuration the vertical pole rod is perpendicular to the horizontal measure arm, and the rotation of the measure wheel is set to zero. The pointer  $F$  is at the lower-right corner of the horizontally aligned square and the contour is travelled counter-clockwise. In the left part of Figure 3.17 the rotation  $\varphi$  of the measure wheel is presented as a function of the travelled distance  $t$  along the contour. The rotation of the measure wheel after one contour travel is  $3.9998$  [rad] making the area of the square equal to  $9999.5$  [mm<sup>2</sup>] which is within  $0.005\%$  of the correct answer. The numerical integration was done by the explicit predictor/corrector algorithm as described (and coded in FORTRAN) by Shampine and Gordon [77], where the absolute local error for all variables

was set to  $10^{-3}$ . The finite element model was expressed in the units [m] and [rad]. The numerical integration took a total of 125 function evaluations, which indicates an average stepsize of  $dt = 3.2$  [mm]. The lateral slip,  $s_2$ , and the longitudinal rate of the wheel,  $v_l = rd\varphi/dt$ , both in [mm/mm], are shown in the right part of Figure 3.17. They clearly demonstrate the skidding ( $s_2$ ) of the rolling ( $v_l$ ) wheel. Note the jumps in the differential ratios at the corners of the square, they are caused by the discontinuous direction of  $t$  at these corners.

### 3.5.2 Swivel Wheel Shimmy

To illustrate the general method for the derivation of the state equations of a non-holonomic system and its linearization we shall revisit the shimmy problem of an aircraft landing gear as treated by Den Hartog [12]. He simplified the problem in order to show the principal mechanism responsible for the shimmy phenomenon. The mass and stiffness of the airplane are assumed large with respect to those of the swivel landing wheel, so that the attachment point of the swivel axis to the airplane may be assumed to move forward with a constant speed. The tire is assumed to be rigid and the inertia along the axis of rotation of the wheel is not taken into account. Then in Figure 3.18, which is a plan

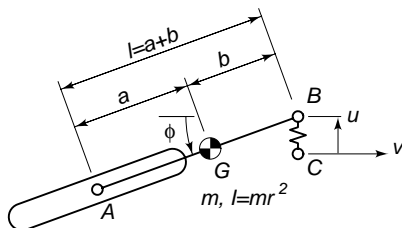


Figure 3.18: Swivel wheel

view of the shimmying wheel seen from above, point  $C$  is the point where the wheel strut is built into the airplane. Point  $B$  is the bottom point of the strut; normally  $B$  is right under  $C$ , but while shimmying the strut is assumed to flex sideways through distance  $u$  at a stiffness  $k$ . The wheel is behind  $B$  with angle  $\phi$ , the shimmy angle, which is zero for normal ideal operation.  $A$  is the centre of the wheel, and  $G$  is the centre of gravity of the combined landing gear. The finite element model consists of a wheel element attached in point  $A$  to a rigid beam. The wheel has zero lateral slip which is the non-holonomic condition in

the system. The beam is connected in point  $B$  to a cylindrical bearing element. The bearing is rigid in the longitudinal and flexible in the lateral and rotational direction and the generalized deformations are denoted by  $u$  and  $\phi$ . The lateral stiffness is  $k$  while the rotational stiffness is assumed to be zero. The bearing is moved forward with a constant speed of  $v$ . The generalized coordinates of the system are given by  $\mathbf{q} = (u, \phi)$ . The zero lateral slip condition on the wheel reduces the coordinates to the degree of freedom  $\mathbf{q}^d = (u)$  and the kinematic coordinate  $\mathbf{q}^k = (\phi)$ . The steady state undeformed motion is characterized by  $(\dot{u}, u, \phi) = (0, 0, 0)$ . With the variations  $\Delta \dot{\mathbf{q}}^d = \Delta \dot{u}$ ,  $\Delta \mathbf{q}^d = \Delta u$  and  $\Delta \mathbf{q}^k = \Delta \phi$ , the coefficients of the linearized state derivatives according to (2.43) are

$$\begin{aligned} \bar{\mathbf{M}} &= m\left(\frac{a^2 + r^2}{l^2}\right), \\ \bar{\mathbf{C}} &= m\left(\frac{ab - r^2}{l^2}\right)\frac{v}{l}, & \mathbf{A} &= \frac{1}{l}, \\ \bar{\mathbf{K}}^d &= k, & \mathbf{B}^d &= 0, \\ \bar{\mathbf{K}}^k &= -m\left(\frac{ab - r^2}{l^2}\right)\frac{v^2}{l}, & \mathbf{B}^k &= -\frac{v}{l}, \\ \bar{\mathbf{f}} &= 0. \end{aligned} \tag{3.44}$$

These coefficients are usually numerically calculated by the program but we present them here in an analytical form so we can compare them with the approach as presented by Den Hartog [12]. His ad hoc analysis leads to an eigenvalue problem. The systematically derived linearized state derivatives (3.44) lead to the same eigenvalue problem and consequently to the same prediction of unstable shimmy behaviour.

To investigate the shimmy motion we start with the usual assumption of an exponential motion for the small variations  $\Delta \mathbf{q}$  of the form  $\Delta \mathbf{q}_0 \exp(\lambda t)$ . The characteristic equation of the eigenvalue problem from (2.43) with the coefficients from (3.44) is

$$\lambda^3 + (1 + \mu)\omega\lambda^2 + \omega_n^2\lambda + \omega\omega_n^2 = 0, \tag{3.45}$$

with the mass distribution factor  $\mu = (ab - r^2)/(a^2 + r^2)$ , the driving frequency  $\omega = v/l$  and the natural frequency  $\omega_n = \sqrt{kl^2/(m(a^2 + r^2))}$ . A necessary and sufficient condition for asymptotic stability is given by the requirement that all roots of (3.45) have negative real parts. Application of Hurwitz's theorem on the characteristic equation (3.45) yields

$$\omega > 0 \quad \text{and} \quad \mu > 0. \tag{3.46}$$

In other words, the motion is stable if the driving speed  $v$  is positive and the centre of mass is positioned such that  $a(l - a) > r^2$ . The latter corresponds to a region of  $\pm\sqrt{(l/2)^2 - r^2}$  around the midpoint  $a = l/2$ . For the critical case, where  $a(l - a) = r^2$ , there is one real eigenvalue  $\lambda_1 = -\omega$  describing the non-oscillating decaying motion and a pair of conjugated imaginary values  $\lambda_{2,3} = \pm\omega_n i$  which describe the undamped oscillatory solution. This critical case corresponds to a mass distribution where point  $B$  is the centre of percussion or in other words, if a lateral force is applied in  $B$  then the lateral reaction force in the contact point  $A$  of the wheel will be zero.

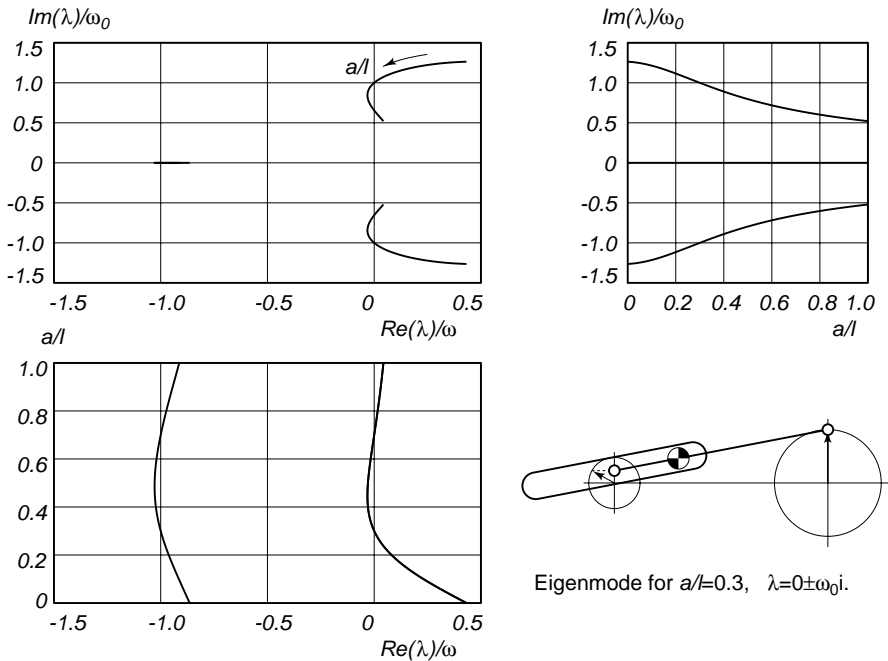


Figure 3.19: Root loci of the eigenvalues  $\lambda$  for the swivel wheel with moment of inertia  $I = 0.21ml^2$  in the centre of mass position range of  $0 \leq a/l \leq 1$  and eigenmode for the undamped oscillatory case  $a/l = 0.3$ , with driving frequency  $\omega = v/l$  and undamped eigenfrequency  $\omega_0 = \sqrt{k/(0.3m)}$ .

The general solution for the eigenvalues can be found by solving the characteristic equation (3.45). However, the general solution of a cubic equation,

as first published by Cardano [80], leads to lengthy expressions and give little insight in the nature of the solution. To illustrate the behaviour of the system at the non-critical cases, consider a swivel wheel with mass moment of inertia  $I = 0.21ml^2$ . The motion is stable if the centre of mass position  $a$  is between  $0.3l$  and  $0.7l$ . The root loci for this example in range of  $0 \leq a/l \leq 1$  are shown in Figure 3.19 together with the eigenmode for the undamped oscillatory case  $a/l = 0.3$ . The lateral displacement of the attachment point  $B$ ,  $u$ , and the lateral displacement of the centre of the wheel  $A$ , denoted by  $w$ , are illustrated in the figure by the vertical projection of the rotating arrows. Note that the lateral displacements are not in phase. The phase angle,  $\psi$ , and the amplitude ratio,  $\Delta w_0/\Delta u_0$ , are for given eigenvalue  $\lambda = \gamma_0 + \omega_0 i$  uniquely determined by the kinematic rate equation (2.41) and read

$$\tan \psi = -\frac{\omega_0}{\omega + \gamma_0} \quad \text{and} \quad \frac{\Delta w_0}{\Delta u_0} = \frac{\omega}{\sqrt{(\omega + \gamma_0)^2 + \omega_0^2}}. \quad (3.47)$$

The wheel centre and the attachment point are always out of phase, even in the undamped oscillatory case where  $\gamma_0 = 0$ .

### 3.6 Three-Dimensional Wheel

The three-dimensional flexible wheel element is a model of a disk bounded by a sharp edge with radius  $r$ , which can roll over a fixed surface. The position and orientation of the wheel will be described by the position of the wheel centre  $\mathbf{w}$ , the orientation of the wheel axle  $\mathbf{e}_w$ , specified by the four Euler parameters  $q = (q_0, \mathbf{q})$ , and the position of the contact point  $\mathbf{c}$  as shown in Figure 3.20. Note that the contact point is a geometric point, it is not a fixed material point of the wheel nor of the surface. In the case of pure rolling as a rigid body the element has three degrees of freedom, while we have ten coordinates describing the position and orientation. Hence we have to impose seven constraints upon the velocities. Only two of these constraints are non-holonomic constraints, all other velocity constraints are time derivatives of holonomic conditions originating from the rigidity conditions.

The first two generalized strains for the wheel element are defined as

$$\begin{aligned} \varepsilon_1 &= \frac{1}{2}(\mathbf{r}^T \mathbf{r} - r_0^2)/r_0 \\ \varepsilon_2 &= \mathbf{e}_w^T \mathbf{r} \end{aligned} \quad (3.48)$$

with the radius vector  $\mathbf{r} = \mathbf{c} - \mathbf{w}$ , the undeformed radius length  $r_0$  and the rotated wheel axle  $\mathbf{e}_w = \mathbf{R}(q)\bar{\mathbf{e}}_w$ , see Figure 3.20. The rotation matrix  $\mathbf{R}(q)$  in



parameters is described in Appendix B, and can be derived from the quaternion product of the adjoint quaternion  $\bar{q} = (q_0, -\mathbf{q})$  and the velocity  $\dot{q} = (\dot{q}_0, \dot{\mathbf{q}})$  represented by  $(\dot{q} \circ \bar{q}) = \frac{1}{2}(0, \boldsymbol{\omega})$  (B.13). Note that the scalar part of this quaternion product is zero only when the norm of the quaternion is constant, as in  $|q| = 1$ . In the contact point the two orthogonal surface tangents are the longitudinal direction  $(\mathbf{r} \times \mathbf{e}_w)$  and the lateral one  $(\mathbf{n} \times (\mathbf{r} \times \mathbf{e}_w))$ . With these directions the longitudinal and lateral slip are defined as

$$\begin{aligned} s_1 &= (\mathbf{r} \times \mathbf{e}_w)^T (\dot{\mathbf{w}} + \boldsymbol{\omega} \times \mathbf{r}) \\ s_2 &= (\mathbf{n} \times (\mathbf{r} \times \mathbf{e}_w))^T \dot{\mathbf{c}} \end{aligned} \quad (3.51)$$

Since  $\mathbf{v}_\varepsilon$  is perpendicular to the longitudinal direction it is not included in the definition of  $s_1$ . If the generalized coordinates which describe the positions and orientation of the element are grouped together in a vector  $\mathbf{x}^T = (\mathbf{w}^T, \mathbf{c}^T, q_0, \mathbf{q}^T)$ , and the vector of slips is denoted by  $\mathbf{s}$ , the expressions for the slip can be written symbolically as

$$\mathbf{s} = \mathbf{V}(\mathbf{x})\dot{\mathbf{x}}. \quad (3.52)$$

Pure rolling is described by zero slips,  $\mathbf{s} = \mathbf{0}$ .

With the vector of element strains expressed as  $\boldsymbol{\varepsilon} = \mathbf{D}(\mathbf{x})$ , the generalized stresses  $\boldsymbol{\sigma}$  and forces  $\boldsymbol{\lambda}$  dual to the slips can be interpreted from the element equilibrium equation,

$$\mathbf{f} = \mathbf{D}_{,\mathbf{x}}^T \boldsymbol{\sigma} + \mathbf{V}^T \boldsymbol{\lambda}. \quad (3.53)$$

The first two generalized stresses  $\sigma_1$  and  $\sigma_2$  are the radial force and the lateral bending force. The third stress,  $\sigma_3$  is the force in the contact point exerted on the wheel perpendicular to the surface. The fourth stress, dual to the tangent condition  $\varepsilon_4 = 0$ , can be interpreted as a torque divided by the radius of the wheel acting in the contact point along the  $s_2$  direction. This torque is always zero under normal loading. Only when forces are applied in the contact point  $\mathbf{c}$ , which is unrealistic since this node is a non-material point, the torque will be non-zero. The generalized forces dual to the slip can be interpreted as  $\lambda_1$  being the longitudinal contact force divided by the actual radius length  $|\mathbf{r}|$  and  $\lambda_2$  the lateral force divided by the actual radius and normal vector length  $|\mathbf{r}||\mathbf{n}|$ . This scaling seems awkward but excluding normalization in the slip definitions (3.51) results in much simpler first and higher order partial derivatives.

Each individual strain can be assumed either zero or non-zero, representing respectively the rigid and the deformable case. In the deformable case a constitutive equation relating  $\boldsymbol{\sigma}$  to  $\boldsymbol{\varepsilon}$  has to be applied. The same holds for a longitudinally and/or laterally slipping wheel. In this case the generalized

stresses, in particular the normal stress  $\sigma_3$ , are usually incorporated in the constitutive behaviour, taking the form  $\boldsymbol{\lambda} = \boldsymbol{\lambda}(\mathbf{s}, \boldsymbol{\sigma})$ . A detailed description of the constitutive behaviour of three-dimensional elastic bodies in rolling contact can be found in the books by Kalker [35] and Johnson [28].

### 3.6.1 The Rolling Disk

One of the simplest and most intriguing examples of a spatial non-holonomic system is a disk rolling without slip on a horizontal plane. From experience we know that such an object, if given enough initial speed, shows stable motion which is quite different from the behaviour at low speed. We will investigate the stability of the rectilinear motion with the help of the wheel element from Chapter 3.6. The rolling of a disk on a horizontal plane has in detail been studied by for example Neĭmark and Fufaev [55] and we shall compare the results. The finite element model of the system consists of a wheel element,

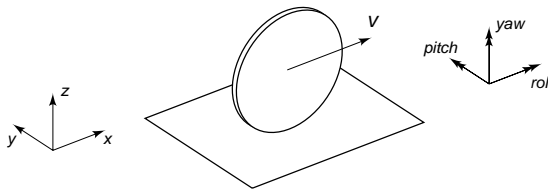


Figure 3.21: Disk rolling on a horizontal plane.

rolling on a horizontal plane  $z = 0$ , and three orthogonal hinges attached to the wheel centre to describe the three degrees of freedom: pitch, roll and yaw (Figure 3.21). The two kinematic coordinates are the  $x$  and  $y$  position of the point of contact in the plane. We will assume that the infinitesimally thin disk has uniformly distributed unit mass  $m$ , unit radius  $r$  and a unit gravitational force field  $g$  in the downward direction.

The stability of the rectilinear motion at longitudinal speed  $v$  is investigated by the determination of the eigenvalues of the linearized equations of motion as described in Section 2.4.2 by equation (2.43). The dimension of the eigenvalue problem is eight; namely two times the number of degrees of freedom plus the number of kinematic coordinates. Beforehand we know that there are six zero eigenvalues. The first two pairs are a consequence of the two cyclic coordinates, the pitch and the yaw, in the system. The potential energy is only a function

of the rotation along the longitudinal axis, the roll angle. The last two zero eigenvalues describe the kinematic motion of the point of contact  $(x, y)$ . The remaining two non-zero eigenvalues of the perturbed rectilinear motion in the speed range of  $0 \leq v \leq 1$ , where speed scales according to  $\sqrt{gr}$ , are shown in Figure 3.22. At low speed there are two equal and opposite real eigenvalues

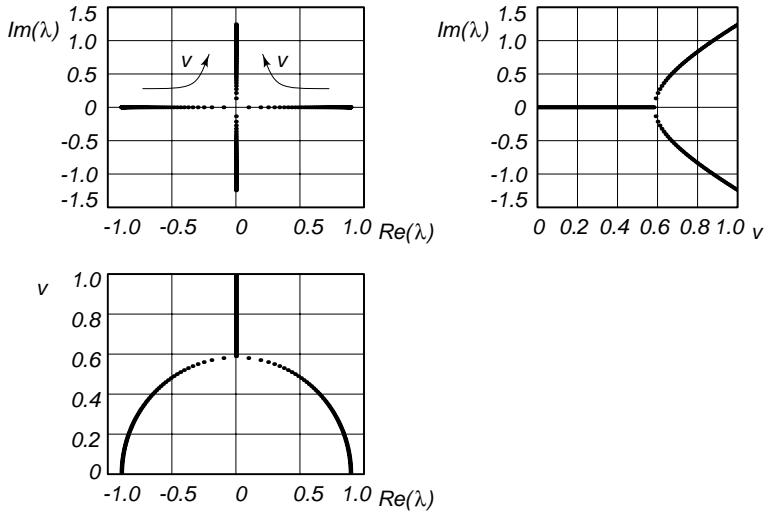


Figure 3.22: Root loci of the eigenvalues  $\lambda$  for the rectilinear motion of a rolling disk on a horizontal plane in the speed range of  $0 \leq v \leq 1$ .

describing unstable perturbed motion, just like an inverted pendulum. At increasing speed these eigenvalues move to zero, where at the critical speed [55],  $v = 1/\sqrt{3} \approx 0.58$ , they change into a pair of conjugated imaginary values which describe an undamped oscillatory motion. The corresponding eigenmode is of the slalom type and can best be characterised by a  $90^\circ$  phase angle between the roll and the yaw motion. Further increase of the speed shows an approximately linear increase in the eigenvalues.

The unstable perturbed motion, below the critical speed, is illustrated by a transient analysis. The initial conditions are a vertical position with a forward speed of  $v = 0.4116$ , an angular roll velocity of  $-0.01$  and a zero yaw rate. The path of the centre of the disk and the path of the contact point in the plane are shown in Figure 3.23 for the time period of 87 units, where one time unit scales according to  $\sqrt{r/g}$ . The low roll velocity starts the initially exponen-

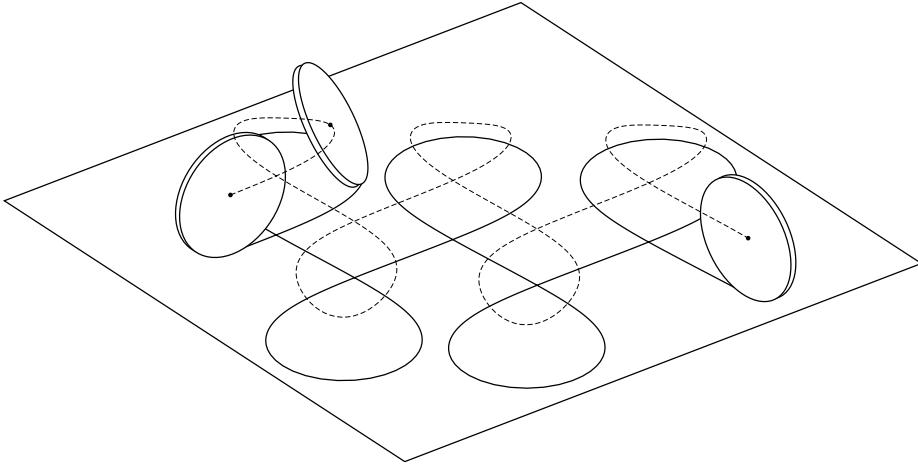


Figure 3.23: Path of a rolling disk on a horizontal plane at subcritical speed for a time period of 87 units, with an initial forward velocity 0.4116 and a roll velocity  $-0.01$ .

tially increasing inclination of the disk, after which it makes a sharp turn and rises up again to the vertical position. This motion is repeated at equal time intervals and in alternating turning directions. The unstable rectilinear motion is transformed into a quasi periodic motion where the disk continues to wobble forward.

The forces in the contact point exerted by the wheel on the plane for this quasi periodic motion are shown in Figure 3.24. During cornering the lateral and normal force increase in magnitude whereas the longitudinal contact force shows a short oscillation indicating an accelerating and decelerating longitudinal motion. The ratio of the in-plane contact force to the normal contact force during cornering is at most 0.52. The friction coefficient must be above this value to ensure rolling without slipping.

However, if we assume a force contact model which is linear in the slip velocities at the contact point then the disk on a smooth surface will slip into an almost cyclic motion during the first turn. In this motion the centre of mass mainly moves in the downward direction while the rotation of the point of contact increases rapidly. The disk eventually will come to the singular horizontal rest position in a finite time. Compare this to the behaviour of the

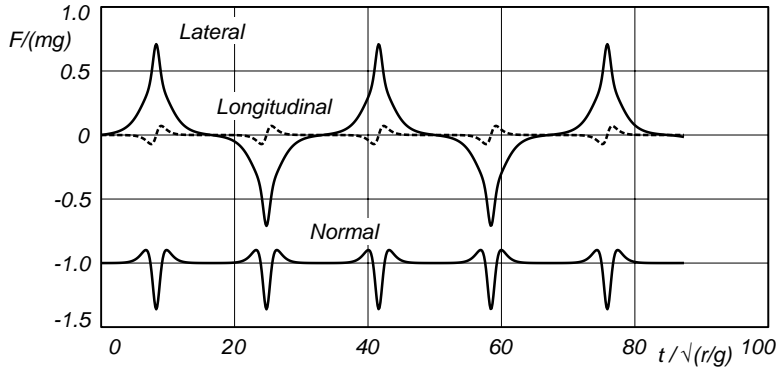


Figure 3.24: Forces in the contact point of a rolling disk on a horizontal plane at subcritical speed for a time period of 87 units, with an initial forward velocity 0.4116 and a roll velocity -0.01.

contemporary executive toy known as “Euler’s disk”; a smooth edged disk on a slight concave supporting bowl which whirrs and shudders to a horizontal rest [52].

### 3.6.2 Bombardier-ILTIS Road Vehicle

The wheel element and the formulation of the dynamic equations for flexible non-holonomic systems are applied to the analysis of the dynamic behaviour of the Bombardier-ILTIS road vehicle. At the 1990 IAVSD workshop on Multibody

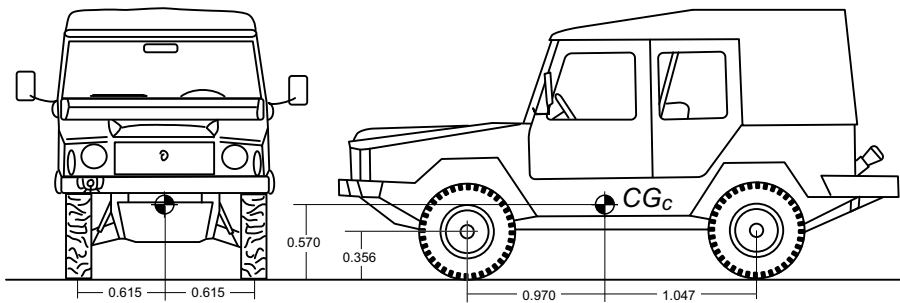


Figure 3.25: The Bombardier Iltis vehicle.

System Analysis Methods and Computer Codes held in Herbertov, Czechoslovakia, this vehicle was chosen for benchmark purpose. The complete benchmark problem together with the results as calculated by some major computer codes are presented in the book by Kortüm and Sharp [38]. On page 32 Sharp describes the model as:

The ILTIS problem involves a rigid cabin structure with six degrees of freedom connected to its four independently suspended wheels by specified links. Track rods connect the steering rack to the wheel carriers at the front, while, at the rear, a similar arrangement applies except that the inner joints are fixed to the cabin structure. The tyres have radial flexibility and are able to generate longitudinal force by interaction of the radial elasticity with sloping ground but not by longitudinal slip. The tyres can sideslip and a detailed tyre lateral force model (for no longitudinal slip) gives the side force and aligning moment as functions of the wheel load, sideslip angle and camber angle.

We interpret this that the longitudinal slip is zero. Front and rear suspension are depicted in Figure 3.26, showing the rear suspension to be a mirror image of that of the front, while the right front suspension is shown in detail in Figure 3.27. Application of the formalism presented in this thesis on the ILTIS problem resulted in a finite element model with 85 elements, 239 generalized deformations, 70 nodes, 226 generalized coordinates, 14 independent coordinates and 10 degrees of freedom.

The first test, the computation of the equilibrium state, was applied to this model and the results are presented in Table 3.2; for comparison the values as calculated by two major computer codes as presented in [38] are listed in the same table. The computed values show a good correspondence with those obtained by the NEWEUL and the SIMPACK program.

In addition the first handling performance test was applied to our model. This test involves a ramp-to-step steer manoeuvre with a forward velocity of 30 [m/s]. The steering rack is displaced with a constant velocity during 0.5 seconds and kept at a constant position for the rest of the simulation time. In the tyre model (CALSPAN), as described in the benchmark [38], it is assumed that the radial compliant tyres roll without longitudinal slip when the vehicle is moving. The lateral tyre force is described as a non-linear function of the radial tyre force, the sideslip, the camber angle, and the tyre velocity. In addition to this force a vertical non-linear aligning torque, originating from the finite contact area, is applied to the tyre. For the tire model two cases have been considered.

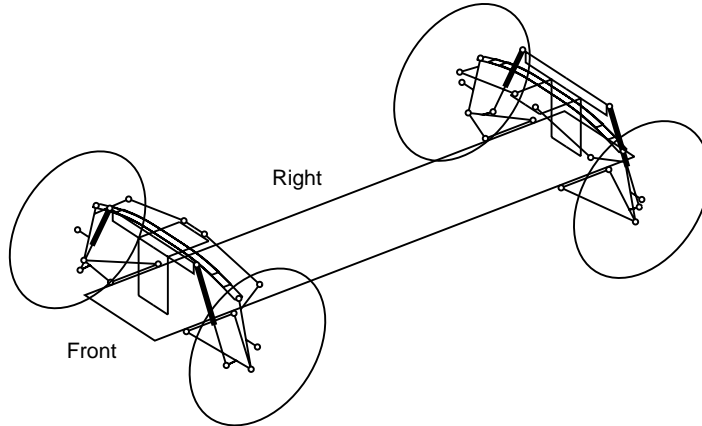


Figure 3.26: Layout of the ILTIS vehicle with front and rear suspensions.

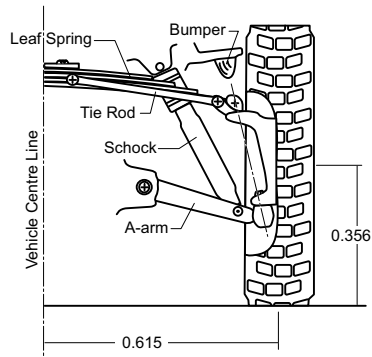


Figure 3.27: Right front wheel suspension details.

<i>Interaction</i>	<i>Dim.</i>	SPACAR	NEWEUL	SIMPACK
cabin: vert. displacement	mm	-7.111	-7.100	-7.094
cabin: pitch angle	°	0.1503	0.1509	0.1468
right front tyre	N	-3835.02	-3834.63	-3831.32
right rear tyre	N	-3588.81	-3588.60	-3591.91
shock absorber right front	N	-337.51	-336.54	-335.51
shock absorber right rear	N	-240.35	-240.43	-241.76
leaf spring right front (spring)	N	-3071.87	-3071.13	-3069.15
leaf spring right front (rod)	N	-1422.45	-1406.13	-1404.68
leaf spring right rear (spring)	N	-2883.87	-2883.07	-2885.75
leaf spring right rear (rod)	N	-1310.38	-1331.68	-1333.80

Table 3.2: Static equilibrium results for the ILTIS vehicle; the results of the present study with SPACAR and those from [38] are given for comparison.

First a simplified version of the model as defined in the benchmark was used. The simplification neglects the minor influence of camber and the tire aligning torque since the wheel element as described in Section 3.6 has no generalized spin defined in the contact point. The resulting yaw rate of the vehicle is shown in Figure 3.28 as the solid line, and is in moderate agreement with the results as computed by the SIMPACK program, represented by the dotted line in the same figure. Second the case is considered in which the lateral slip of the tires is constrained to zero, as in the case of pure rolling. The result for the yaw rate is shown by the dashed line in Figure 3.28. We see that the finite tire stiffness reduces the stationary yaw rate of the vehicle. Note the transient behaviour after the steering rack is held at a constant position.

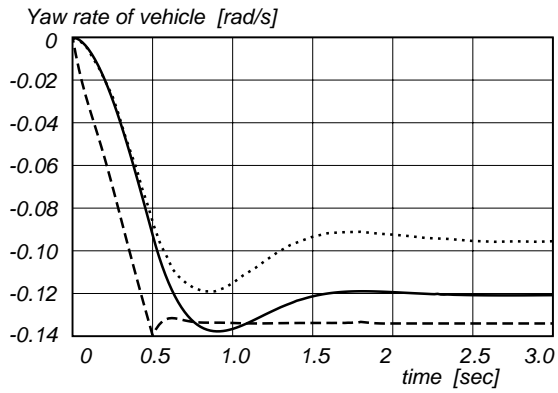


Figure 3.28: Yaw rate of the ILTIS vehicle for  $v = 30$  [m/s], solid line is with simplified tire model, dashed line is with zero lateral slip, dotted line is with complete tyre model as computed by SIMPACK [38] for comparison.

## Chapter 4

# Solution Techniques for Small Vibrations

John Franklin war schon zehn Jahre alt und noch immer so langsam, daß er keinen Ball fangen konnte. . . . Er sah nicht genau, wann der Ball die Erde berührte. Er wußte nicht genau, ob es wirklich der Ball war, was gerade einer fing, oder ob der, bei dem er landete, ihn fing, oder nur die Hände hinhielt.

(Sten Nadolny, *Die Entdeckung der Langsamkeit*)

A number of formalisms for deriving the equations of motion of rigid and flexible multibody systems are available [65, 76] and have nowadays been implemented in computer codes [66] such as ADAMS, DADS, and SIMPACK. With these codes it is possible to make simulations of the motion of the systems under consideration. The simulation is made by numerical integration of the equations of motion, that is, by performing a transient analysis with a specific set of initial conditions. Some codes provide tools for finding equilibrium configurations and calculating eigenfrequencies and eigenmodes.

For many applications to engineering problems a model in which all structural elements are assumed to be rigid suffices for a quick judgement about the motion and forces in the system. However, in cases where a high accuracy is required, for instance in positioning mechanisms, or when the structural elements are rather compliant, vibrations due to deformation can become important and have to be considered. Incorporation of these deformations in the dynamic analysis of the system enlarges the number of degrees of freedom, the frequency range to be considered, and the stiffness of the differential equations, which results in a longer simulation time.

To reduce the simulation time and to gain more insight in the vibration phenomena at hand we propose to superimpose small linear vibrations on the nominal non-linear rigid body motion. This idea has been inspired by the computational results from simulations of flexible multibody systems where one often recognizes a gross rigid motion with small-amplitude nearly harmonic vibrations added. This idea can at least be traced back to Cleghorn *et al.* [10], who use an ad-hoc Lagrangian approach and only describe the periodic solutions. The stability of these solutions and the transient solutions are not considered.

The method of superimposition as presented here systematically leads to a system of linear differential equations with time-varying coefficients and time-varying forcing. In particular, if the nominal reference motion is periodic, the coefficients and forcing are also periodic. The structure of the solutions of the equations with periodic coefficients is given by the Floquet theory [15]. Most books on this subject, for instance Yakubovich & Starzhinskii [89], deal almost exclusively with the homogeneous system and the determination of boundaries of regions with stable solutions in a parameter space. The book by Bolotin [3] is more directed towards applications in mechanics and includes a discussion of forced systems and the influence of non-linear terms, as is relevant to the subject of the present study.

Numerical methods for the direct determination of stationary and periodic solutions of the system, the investigation of the stability of these solutions and the continuation of these solutions if a parameter, for instance the driving speed of a mechanism, is varied, are given by Meijaard [43, 45]. He uses a simple shooting method for the determination of the periodic solutions. The stability of these solutions is investigated by examining the eigenvalues of the monodromy matrix, the matrix in which every column represents the state after one period for a unit initial condition. Overviews of some other numerical methods for analysing the systems are given by Friedmann [16] and Aannaque *et al.* [1]. They base their methods on the efficient numerical computation of the transition matrix, or monodromy matrix. We propose to use a harmonic balance method for determining periodic solutions, a kind of averaging method for transient solutions and a method directly based on the Floquet theory for stability analysis.

There are several ways to interpret the superimposition procedure. It can be seen as a first step in a regular perturbation expansion of the solution, or as a first step in an iterative solution procedure as proposed by Ling and Wu [42] and applied by Cardona *et al.* [8]. Our main point of view is that it should be interpreted as a first step of a Newton-Kantorovich iteration method [36]. This method has the advantage that no small parameter has to be identified in advance and that it is robust, so in each step the linearization and the solution

of the linearized problem has only to be carried out to a certain precision and remaining errors can be accounted for in the next step. Quadratic convergence is guaranteed if the initial approximation is sufficiently close to a solution, the non-linearity is small and the linear operator is not nearly singular.

The complete solution of the motion of a flexible multibody system is approximated by the nominal rigid body motion, and a periodic solution and a transient of the linearized equations superimposed on it. The nominal rigid body motion of the system is described in Section 2.2. In this chapter, approximate methods for finding the periodic and transient solutions for the small vibrations and a method for determining their stability will be discussed.

This chapter is organized as follows. The solution techniques for periodic solutions of the small vibrations are discussed in Section 4.1. The transient solution, which must be added to the total solution to satisfy the initial conditions, is treated in the next section. The stability of the solutions, which are investigated by a method directly based on the theory of Floquet, are treated in Section 4.3. Finally, in the last Section, four examples are presented to illustrate the techniques: first, a pendulum with prescribed elliptic motion of its support point, which leads to a forced Mathieu equation; second, a slider-crank mechanism with flexible connecting rod; third, a rotor dynamic system with isotropic bearings; and fourth, the dynamic analysis of a flexible drive shaft connected by two universal joints.

## 4.1 Periodic Solution

The starting point for the periodic solution of the small vibration is the linearized equation of motion (2.11) with the excitation  $-\mathbf{f}^d$ , left over from the nominal solution, on the right-hand side

$$\bar{\mathbf{M}}(t_j)\Delta\ddot{\mathbf{q}}^d + \bar{\mathbf{C}}(t_j)\Delta\dot{\mathbf{q}}^d + \bar{\mathbf{K}}(t_j)\Delta\mathbf{q}^d = -\mathbf{f}^d(t_j). \quad (4.1)$$

Additional forces  $\mathbf{f}_a^d$  are assumed to have been absorbed in  $-\mathbf{f}^d$  if they are present. Here  $t_j$  denote the discrete times with  $j = 0, \dots, p$  and  $p$  being the total number of discrete positions in which the system is calculated. The period of the system is  $T = (t_p - t_0) = 2\pi/\omega$ .

As a periodic solution of these equations we propose a truncated Fourier series for  $\Delta\mathbf{q}^d$  with the same fundamental frequency  $\omega$  as the nominal gross motion,

$$\Delta\mathbf{q}^d = \sum_{l=-m}^m \Delta\tilde{\mathbf{q}}_l^d e^{il\omega t}. \quad (4.2)$$

Here  $m$  is the number of frequencies that is expected to determine the solution to the required accuracy, which is usually much less than  $p/2$ . The unknown coefficients  $\Delta\tilde{\mathbf{q}}_l^d$  are calculated as follows. First, the linearized equation (4.1) is transformed for every discrete moment in time as

$$\Delta\ddot{\mathbf{q}}^d + \mathbf{P}(t_j)\Delta\dot{\mathbf{q}}^d + \mathbf{Q}(t_j)\Delta\mathbf{q}^d = \mathbf{r}(t_j), \quad (4.3)$$

with

$$\begin{aligned} \mathbf{P}(t_j) &= \bar{\mathbf{M}}^{-1}(t_j)\bar{\mathbf{C}}(t_j), \\ \mathbf{Q}(t_j) &= \bar{\mathbf{M}}^{-1}(t_j)\bar{\mathbf{K}}(t_j), \\ \mathbf{r}(t_j) &= -\bar{\mathbf{M}}^{-1}(t_j)\mathbf{f}^d(t_j). \end{aligned} \quad (4.4)$$

Second, the coefficients of this equation are transformed into Fourier series [7] as in

$$\Delta\ddot{\mathbf{q}}^d + \left( \sum_k \tilde{\mathbf{P}}_k e^{ik\omega t} \right) \Delta\dot{\mathbf{q}}^d + \left( \sum_k \tilde{\mathbf{Q}}_k e^{ik\omega t} \right) \Delta\mathbf{q}^d = \sum_k \tilde{\mathbf{r}}_k e^{ik\omega t}. \quad (4.5)$$

Here, the summation over  $k$  extends from  $-(p-1)/2$  to  $(p-1)/2$  for odd  $p$  and from  $-(p-2)/2$  to  $(p-2)/2$  for even  $p$ . Third, the truncated Fourier series for  $\Delta\mathbf{q}^d$  (4.2) is substituted in the differential equations (4.5) and every individual harmonic is balanced. This means that the convolutions are determined and the coefficients of  $\exp(ik\omega t)$ , ( $k = -m, \dots, m$ ) on both sides of the equation are balanced. This results in a set of  $(2m+1)n$  linear equations of the form

$$\begin{pmatrix} \ddots & & & & & \ddots \\ \cdots & \tilde{\mathbf{Q}}_0 - i\omega\tilde{\mathbf{P}}_0 - \omega^2\mathbf{I} & \tilde{\mathbf{Q}}_{-1} & \tilde{\mathbf{Q}}_{-2} + i\omega\tilde{\mathbf{P}}_{-2} & \cdots & \\ \cdots & \tilde{\mathbf{Q}}_1 - i\omega\tilde{\mathbf{P}}_1 & \tilde{\mathbf{Q}}_0 & \tilde{\mathbf{Q}}_{-1} + i\omega\tilde{\mathbf{P}}_{-1} & \cdots & \\ \cdots & \tilde{\mathbf{Q}}_2 - i\omega\tilde{\mathbf{P}}_2 & \tilde{\mathbf{Q}}_1 & \tilde{\mathbf{Q}}_0 + i\omega\tilde{\mathbf{P}}_0 - \omega^2\mathbf{I} & \cdots & \\ \ddots & & & & & \ddots \end{pmatrix} \begin{pmatrix} \vdots \\ \Delta\tilde{\mathbf{q}}_{-1}^d \\ \Delta\tilde{\mathbf{q}}_0^d \\ \Delta\tilde{\mathbf{q}}_1^d \\ \vdots \end{pmatrix} = \begin{pmatrix} \vdots \\ \tilde{\mathbf{r}}_{-1} \\ \tilde{\mathbf{r}}_0 \\ \tilde{\mathbf{r}}_1 \\ \vdots \end{pmatrix}, \quad (4.6)$$

or in compact notation

$$\sum_l \{ \tilde{\mathbf{Q}}_{k-l} + (il\omega)\tilde{\mathbf{P}}_{k-l} - (l\omega)^2\delta_{kl}\mathbf{I} \} \Delta\tilde{\mathbf{q}}_l^d = \tilde{\mathbf{r}}_k, \quad (4.7)$$

with  $n$  the dimension of the deformation mode coordinate vector  $\Delta\mathbf{q}^d$  and  $k$  and  $l$  extend from  $-m$  to  $m$ . If  $k-l$  falls outside the range, the matrices  $\tilde{\mathbf{Q}}_{k-l}$  and  $\tilde{\mathbf{P}}_{k-l}$  are replaced by zero matrices. From this harmonic balance (4.7) the coefficients  $\Delta\tilde{\mathbf{q}}_l^d$  can be solved. These coefficients are the harmonics of the periodic solution and tell us how each frequency is present in the response. Finally, the result can be interpreted in the time domain as in equation (4.2).

## 4.2 Transient Solution

The complete solution of the linearized equations consists of a periodic solution as determined in the previous section and a transient solution that is added to it in order to satisfy the initial conditions. The transient solution is constructed with the help of the method of slowly varying coefficients and averaging, as described for instance by Verhulst [85, Chapter 11]. This transient solution has to satisfy the homogeneous equations corresponding to (2.11), which are rewritten as a system of first-order differential equations, as in

$$\dot{\mathbf{y}} = \mathbf{A}(t)\mathbf{y}, \quad \text{with} \quad \mathbf{y} = \begin{bmatrix} \Delta \mathbf{q}^d \\ \Delta \dot{\mathbf{q}}^d \end{bmatrix}, \quad (4.8)$$

$$\mathbf{A}(t) = \begin{bmatrix} \mathbf{0} & \mathbf{I} \\ -\bar{\mathbf{M}}^{-1}(t)\bar{\mathbf{K}}(t) & -\bar{\mathbf{M}}^{-1}(t)\bar{\mathbf{C}}(t) \end{bmatrix}.$$

The matrix  $\mathbf{A}(t)$  from (4.8) is periodic with period  $T = 2\pi/\omega$  as stated in the previous section, and can be written as the sum of a constant part,  $\mathbf{A}_0$ , and a periodic part, with average equal to zero,  $\tilde{\mathbf{A}}(t)$ . The differential equations are transformed on the basis of eigenvectors of the matrix  $\mathbf{A}_0$ , which results in

$$\dot{\mathbf{z}} = [\mathbf{J}_0 + \tilde{\mathbf{J}}(t)]\mathbf{z}, \quad (4.9)$$

where  $\mathbf{Y}$  is the matrix of eigenvectors and

$$\mathbf{J}_0 = \mathbf{Y}^{-1}\mathbf{A}_0\mathbf{Y}, \quad \tilde{\mathbf{J}}(t) = \mathbf{Y}^{-1}\tilde{\mathbf{A}}(t)\mathbf{Y}. \quad (4.10)$$

If we assume that all eigenvalues of  $\mathbf{A}_0$  are distinct, the matrix  $\mathbf{J}_0$  is diagonal and  $\tilde{\mathbf{J}}(t)$  is in general a full time dependent matrix with period  $T$ , whose entries are assumed to be small with respect to the diagonal terms of  $\mathbf{J}_0$ . A second transformation writes the differential equations on the basis of eigensolutions according to the diagonal matrix  $\mathbf{J}_0$  with slowly varying coefficients  $\mathbf{a}(t)$ . With

$$\mathbf{z} = e^{\mathbf{J}_0 t}\mathbf{a}, \quad (4.11)$$

this results in a set of differential equations for the amplitudes  $\mathbf{a}$  as

$$\dot{\mathbf{a}} = [e^{-\mathbf{J}_0 t}\tilde{\mathbf{J}}(t)e^{\mathbf{J}_0 t}]\mathbf{a}. \quad (4.12)$$

This equation is still fully equivalent to (4.8). Now if it is assumed that  $\mathbf{J}_0$  contains only well separated damped eigenfrequencies with a corresponding period that is small in comparison with  $T$ , that is, the diagonal elements of  $\mathbf{J}_0$  have

negative real parts, while their imaginary parts are much larger than  $\omega = 2\pi/T$ , and have relatively large differences, then only the diagonal terms of  $\tilde{\mathbf{J}}(t)$  yield significant contributions after averaging. The off-diagonal terms give rise to oscillating terms of the form  $\tilde{J}_{ij} \exp[-J_{0ii} + J_{0jj}]t$  ( $i \neq j$ ) which disappear in the process of averaging. The solution of the amplitudes becomes

$$a_i(t) = a_i(0) e^{\int_0^t \tilde{J}_{ii}(\tau) d\tau}. \quad (4.13)$$

Given the Fourier series of  $\mathbf{A}(t)$  and of  $\tilde{\mathbf{J}}(t)$ , it would be tempting to try and find the Fourier series of  $\mathbf{a}(t)$ . Owing to the non-linear operator  $\exp(\int \dots dt)$  this is not straightforward and we propose to solve for the transient solution according to (4.13) and, if necessary, to calculate the Fourier series of the result.

If the assumptions are fulfilled, the first order averaging appears to have a sufficient accuracy for our application. In other cases or when a higher accuracy is required, direct numerical integration of the linearized equations can be used.

### 4.3 Stability of the Solutions

The stability of the solutions can be investigated by analysing the homogeneous equations. Several methods can be used. For instance, if the method of slowly varying amplitude and averaging is used, as in the previous section, the stability is directly determined by the eigenvalues of  $\mathbf{A}_0$ , as can be seen from (4.11) and (4.12). If they have all negative parts, stability is expected if the approximation is sufficiently accurate and the stability margin is sufficiently large. This method, however, is not always reliable.

Another more exact method used by Meijaard [43, 45], first calculates the monodromy matrix, the matrix in which every column represents the state after one period for a unit initial condition, after which the characteristic multipliers are determined as the eigenvalues of this matrix. If all eigenvalues have a modulus that is smaller than one, the periodic solution is stable and if some eigenvalue has a modulus larger than one, the periodic solution is unstable. If some eigenvalue has a modulus equal to one, we are in a bifurcation point.

Yet another approach is proposed here, which is directly based on the theory of Floquet [15]. This theory states that the solution of the homogeneous system consists of a sum of  $2n$  ( $2n$  is the number of first order differential equations as in equation 4.8) fundamental solutions of the form of a periodic function multiplied by an exponential function (in the generic case of distinct characteristic multipliers). From these, the characteristic exponents and hence the stability

can directly be read. The relation between a characteristic exponent  $\lambda$  and a characteristic multiplier  $\rho$  is the exponential function  $e^{\lambda T} = \rho$ , where  $T$  is the period of the solution.

We assume fundamental solutions of the form

$$\Delta \mathbf{q}^d = e^{\lambda t} \sum_{l=-m}^m \Delta \tilde{\mathbf{q}}_l^d e^{il\omega t}, \quad (4.14)$$

where  $\lambda$  is a characteristic exponent. This expression can be substituted in the homogeneous equations (4.5) or an equivalent system of first-order equations (4.8). By collecting terms with equal exponentials and equating the coefficients of  $\exp(\lambda t + il\omega t)$  ( $l = -m, \dots, m$ ) to zero, we obtain a set of homogeneous linear algebraic equations for the values of  $\Delta \tilde{\mathbf{q}}_l^d$  as

$$\sum_l \{ \lambda^2 \delta_{kl} \mathbf{I} + \lambda \mathbf{V}_{kl} + \mathbf{W}_{kl} \} \Delta \tilde{\mathbf{q}}_l^d = \mathbf{0}, \quad (4.15)$$

with  $k$  and  $l$  ranging from  $-m$  to  $m$ . The structure of the contribution of  $\mathbf{V}$  and  $\mathbf{W}$  in this set of equations is

$$\mathbf{V} = \begin{pmatrix} \ddots & \vdots & \vdots & \vdots & \ddots \\ \cdots & \tilde{\mathbf{P}}_0 - 2i\omega \mathbf{I} & \tilde{\mathbf{P}}_{-1} & \tilde{\mathbf{P}}_{-2} & \cdots \\ \cdots & \tilde{\mathbf{P}}_1 & \tilde{\mathbf{P}}_0 & \tilde{\mathbf{P}}_{-1} & \cdots \\ \cdots & \tilde{\mathbf{P}}_2 & \tilde{\mathbf{P}}_1 & \tilde{\mathbf{P}}_0 + 2i\omega \mathbf{I} & \cdots \\ \ddots & \vdots & \vdots & \vdots & \ddots \end{pmatrix},$$

and

$$\mathbf{W} = \begin{pmatrix} \ddots & \vdots & \vdots & \vdots & \ddots \\ \cdots & \tilde{\mathbf{Q}}_0 - i\omega \tilde{\mathbf{P}}_0 - \omega^2 \mathbf{I} & \tilde{\mathbf{Q}}_{-1} & \tilde{\mathbf{Q}}_{-2} + i\omega \tilde{\mathbf{P}}_{-2} & \cdots \\ \cdots & \tilde{\mathbf{Q}}_1 - i\omega \tilde{\mathbf{P}}_1 & \tilde{\mathbf{Q}}_0 & \tilde{\mathbf{Q}}_{-1} + i\omega \tilde{\mathbf{P}}_{-1} & \cdots \\ \cdots & \tilde{\mathbf{Q}}_2 - i\omega \tilde{\mathbf{P}}_2 & \tilde{\mathbf{Q}}_1 & \tilde{\mathbf{Q}}_0 + i\omega \tilde{\mathbf{P}}_0 - \omega^2 \mathbf{I} & \cdots \\ \ddots & \vdots & \vdots & \vdots & \ddots \end{pmatrix},$$

with sub-matrices having a dimension of  $n \times n$ . These individual contributions can be expressed in a compact form as

$$\begin{aligned} \mathbf{V}_{kl} &= \tilde{\mathbf{P}}_{k-l} + 2(i\omega) \delta_{kl} \mathbf{I}, \\ \mathbf{W}_{kl} &= \tilde{\mathbf{Q}}_{k-l} - (l\omega)^2 \delta_{kl} \mathbf{I} + (i\omega) \tilde{\mathbf{P}}_{k-l}. \end{aligned} \quad (4.16)$$

Again, if  $k - l$  falls outside the range, the matrices  $\tilde{\mathbf{P}}_{k-l}$  and  $\tilde{\mathbf{Q}}_{k-l}$  are replaced by zero matrices. Note that the matrix  $\mathbf{W}$  is equal to the matrix from the harmonic balance (4.6) of the periodic solution. Non-trivial solutions for  $\Delta\tilde{\mathbf{q}}_l^d$  are only possible if the determinant of the coefficients of (4.15) is zero, which leads to an eigenvalue problem for the characteristic exponents  $\lambda$ .

Because this determinant has the order  $(2m + 1)2n$ , the number of characteristic exponents obtained in this way is  $(2m + 1)$  times as large as their true number. They appear in clusters of values which differ approximately by an integral multiple of  $i\omega$  and correspond to the same fundamental solution. From each cluster, only the exponent that has the smallest imaginary part is considered as an approximation for the true characteristic exponent. If all exponents have a negative real part, the periodic solution is stable and if some exponent has a positive real part, the periodic solution is unstable. The special case of a complex conjugated pair of exponents with zero real part can lead to bifurcation and usually needs closer investigation, as described by Meijaard [47]. Algorithms that calculate only a subset of the eigenvalues with the smallest absolute values [19] can be used to advantage.

This method of determining characteristic exponents can be seen as an extension of the method of truncated infinite determinants of Hill [25]. Also Bolotin [3] gives a description. Naab and Weyh [53] use a similar method.

## 4.4 Examples and Comparison

### 4.4.1 Parametrically Excited Pendulum

As a first example of the described method a pendulum with a forced elliptic motion of its support point is considered. Especially the cases of purely vertical motion and circular motion constitute well studied problems. The system, shown in Figure 4.1, consists of a rigidly modelled vertical pendulum of length  $l = 1.0$  [m] with a point mass at the bottom end. The top end moves on an ellipse. This path is generated by a hypocycloidal gear pair with a ratio of annulus over spur radius equal to 2. This gear pair is also known as ‘Cardan circles’. The top end of the pendulum is pin joined to the pinion at a distance  $er$  from the centre, in this way creating an ellipse with major axis  $2(1 + e)r$  and minor axis  $2(1 - e)r$ . In this example the pinion radius  $r$  is taken 0.5 [m] and the eccentricity factor  $e$  is 0.5. A crank with a uniform angular velocity  $\omega$  moves the centre of the pinion. In the joint between the pendulum and the pinion a viscous damping is assumed which results in 1% of critical damping

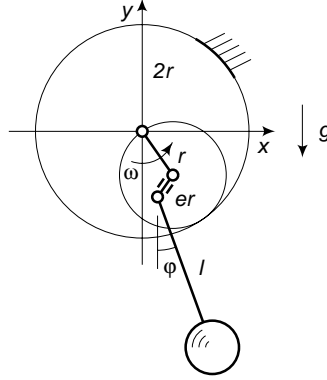


Figure 4.1: Pendulum with a forced elliptical motion of its support point.

in the linearized equations. The system operates in a gravitational field with  $g = 9.81$  [N/kg]. With the elliptical motion of the support point given by

$$\begin{aligned} x &= (1 - e)r \sin(\omega t) \\ y &= -(1 + e)r \cos(\omega t), \end{aligned} \quad (4.17)$$

the non-linear equation of motion for the pendulum can be derived as

$$\ddot{\varphi} + 2\zeta\omega_0(\dot{\varphi} + \omega) + \omega_0^2 \sin \varphi + \rho\omega^2[\sin(\varphi - \omega t) + e \sin(\varphi + \omega t)] = 0, \quad (4.18)$$

with the parameters  $\rho = r/l$ , the relative damping  $\zeta$  and the undamped eigenfrequency of the isolated pendulum  $\omega_0 = \sqrt{g/l}$ . The angle  $\varphi$  is measured from the down-hanging vertical position. The linearized equation of motion, which describes the small vibration  $\Delta\varphi$  around  $\varphi = 0$ , is

$$\Delta\ddot{\varphi} + 2\zeta\omega_0\Delta\dot{\varphi} + [\omega_0^2 + (1 + e)\rho\omega^2 \cos(\omega t)]\Delta\varphi = -2\zeta\omega_0\omega + (1 - e)\rho\omega^2 \sin(\omega t). \quad (4.19)$$

The periodic solution for  $\Delta\varphi$  is assumed to be a truncated Fourier series with the fundamental frequency equal to the driving frequency  $\omega$ . Notice that the periodic solution of  $\Delta\varphi$  will show a non-zero mean value due to the term related to the damping  $-2\zeta\omega_0\omega$  in the right-hand side of differential equation (4.19). A characteristic value for the periodic solution is the amplitude  $\Delta\hat{\varphi}$ , being  $\frac{1}{2}[(\Delta\varphi)_{max} - (\Delta\varphi)_{min}]$  (half of the range of  $\Delta\varphi$ ) over one period. This amplitude is shown in Figure 4.2 for a range of driving speeds  $\omega$ . Resonance

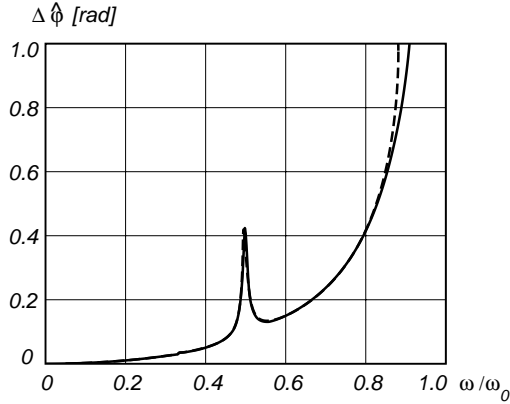


Figure 4.2: Amplitude  $\Delta\hat{\phi}$  of the periodic solution of the pendulum for damping  $\zeta = 0.01$  in the driving speed range of  $0 < \omega/\omega_0 < 0.9$ . The solid line is the linearized result, the dashed line is the full non-linear result.

clearly occurs at about  $1/2$  of the undamped eigenfrequency  $\omega_0$ . The  $1/3$  subresonance is just discernible. If we compare this with the full non-linear response curves, the dashed lines, we see approximately the same result; only the resonance peak bends slightly backward due to the non-linearity. The non-linear response was calculated with a shooting method as described by Meijaard [45].

Although we have shown the equation of motion and its linearization in an analytic form we must emphasize that all calculations presented here were done in a discrete and numeric way as described throughout this work. The finite element model of the system is straightforward. A rigid beam, acting as crank with length  $r$ , drives the centre of the spur of the hypocycloidal gear pair element. The annulus, with radius  $2r$ , is fixed in position and orientation. A second rigid beam, with length  $er$ , is rigidly attached to the centre of the spur and rotates with the spur. At the other end of this beam two hinges are mounted in series. A third rigid beam, acting as a pendulum with length  $l$ , is attached to the other end of these hinges. Finally, a concentrated mass and force is applied at the end of the pendulum beam. The first hinge rotation is released, whereas the middle node of the two hinges is fixed with respect to the inertia frame. In this way the relative rotation of the second hinge describes the orientation of the pendulum with respect to a fixed vertical and can be used as the degree of freedom,  $\mathbf{q}^d$ , the coordinate to be linearized. The periodic input,

one full rotation of the crank, was discretised into 32 evenly spaced intervals, and up to seven harmonics were included in the periodic solutions. The results from Figure 4.2 suggest that the inclusion of only three harmonics would have been accurate enough.

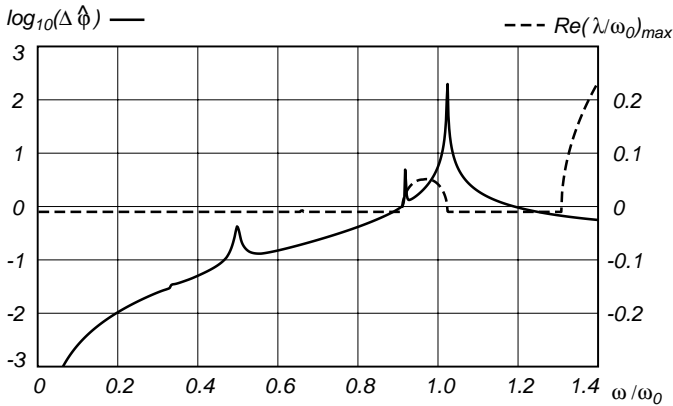


Figure 4.3: The solid line is the logarithmic amplitude  $\Delta\hat{\phi}$  for the periodic solution of the pendulum for damping  $\zeta = 0.01$  in the driving speed range  $0 < \omega/\omega_0 < 1.4$ . The dashed line is the maximum of the real part of the dimensionless characteristic exponents  $\lambda/\omega_0$ .

The same response as in Figure 4.2 but on a logarithmic scale over a wider range of driving speeds together with an indication upon the stability of the periodic solution is shown in Figure 4.3. If the maximal real part of the characteristic exponents  $\lambda$ , defined in (4.14), is negative, the solution is stable. From the figure we see that stable periodic solutions can be found within the driving speed ranges  $0 \leq \omega/\omega_0 < 0.91$  and  $1.02 < \omega/\omega_0 < 1.31$ . All periodic solutions within the range  $0.9 < \omega/\omega_0 < 1.2$  must be discarded due to the large amplitudes which are in contradiction with the assumption of small vibrations.

The nature of the instabilities of the periodic solutions is best demonstrated by a stability analysis were only two harmonics are considered. The characteristic exponents for this analysis are shown in Figure 4.4.1. The number of exponents obtained is  $(2 \times 2 + 1) = 5$  times as large as the number of first order differential equations, being 2, making a total of 10. The appearance in clusters of values which differ approximately by an integral multiple of  $i\omega$  is apparent.

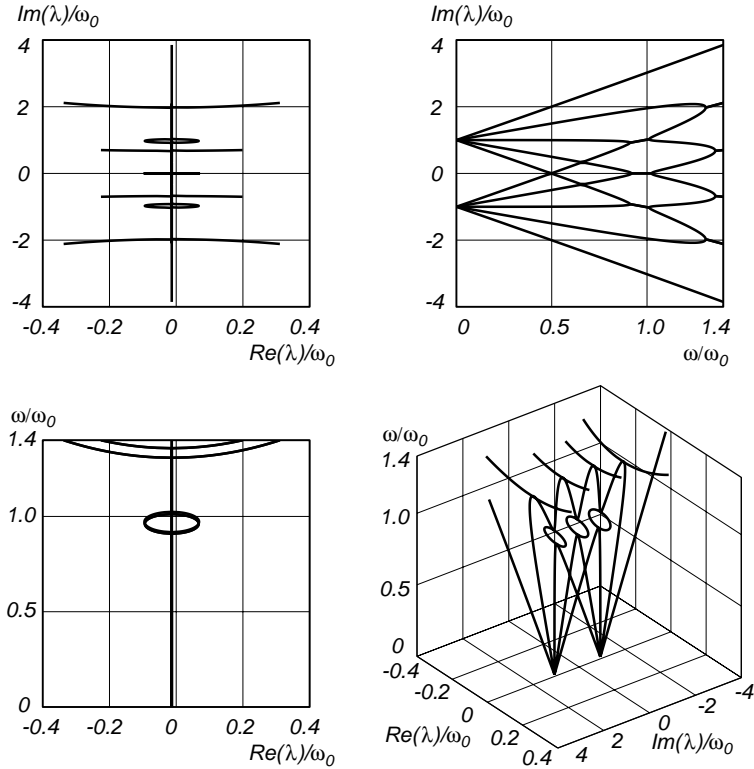


Figure 4.4: Three-dimensional plot of the dimensionless characteristic exponents  $\lambda/\omega_0$  indicating the stability of the periodic solutions with only 2 harmonics for the pendulum with damping  $\zeta = 0.01$ , in the driving speed range  $0 < \omega/\omega_0 < 1.4$ .

The instabilities near  $\omega/\omega_0 = 0.91$  and  $\omega/\omega_0 = 1.02$  are of the transcritical type, in which a characteristic exponent becomes zero and the resonance peaks become unbounded. The amplitudes as shown in Figure 4.3 remain bounded because the response was calculated for a finite number of discrete values of  $\omega$ . Near  $\omega/\omega_0 = 1.31$  a Neimark-Hopf bifurcation occurs, where a pair of complex conjugated characteristic exponents cross the imaginary axis and no resonance appears.

#### 4.4.2 Slider-Crank Mechanism

As a second and more engineering type of example a slider-crank mechanism is considered. The same mechanism has been used as an example in a series of publications by Song and Haug [78], Jonker [30] and Meijaard [45], among others. With [45] a comparison will be made.

The system consists of a rigidly modelled crank of length 0.15 [m], a flexible connecting rod of length 0.3 [m] and a plunger. The crank and the connecting rod have a uniform mass distribution of  $0.2225 \text{ [kgm}^{-1}\text{]}$ , the mass of the plunger is  $0.033375 \text{ [kg]}$ , the flexural rigidity of the connecting rod is  $EI = 12.72345 \text{ [Nm}^2\text{]}$  and the centre line is assumed inextensible. The crank rotates at a constant angular velocity  $\omega$ , so this system is periodically forced. Two values of material damping according to the Kelvin-Voigt model are considered, such that the damping in the connecting rod of the first eigenmode for small vibrations when the crank is fixed is 1% respectively 2% of critical damping. The connecting rod is modelled by two planar beam elements (4 dynamic degrees of freedom).

Figure 4.5 shows the periodic and the total, summed periodic and first period transient, response for  $\omega = 150 \text{ [rad/s]}$  of the dimensionless lateral deflection of the centre of the connecting rod, that is, the distance of the centre point of the rod to the line connecting the endpoints divided by the reference length of the rod. The deformations and deformation rates of the connecting rod are zero at  $t = 0$  and the shown solution corresponds to the 2% damping case. If we compare the linearized results with the results from Meijaard [45] we note the good agreement. However, in the transient response we see a small difference at the start, due to non-linearity and inaccuracy in the process of averaging.

Figure 4.6 shows the dimensionless maximal midpoint deflection for different values of the angular velocity of the crank for the periodic solution. Resonances occur at about  $1/5$ ,  $1/4$  and  $1/3$  of the first eigenfrequency. For the numerical model of the connecting rod with pinned joints and modelled by two beam elements, this frequency is  $832 \text{ [rad/s]}$ . If we compare this with the full non-

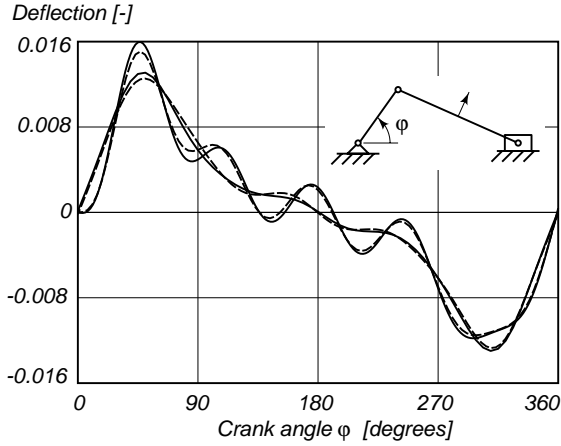


Figure 4.5: Dimensionless midpoint deflections of the connecting rod at  $\omega = 150$  [rad/s] and a damping of 2%. The smooth curves are the periodic solutions and the oscillating curves are the sum of the periodic and the transient solutions. The fully drawn lines are the linearized results, the dashed lines are the full non-linear results from Meijaard [45].

linear response curves, the dashed lines, we see that the resonance at  $1/5$  of the first eigenfrequency is not observed and the resonance peaks bend backwards owing to the non-linearity.

Figure 4.7 shows the amplitude of the first four harmonics of the periodic solutions as a function of the driving frequencies  $\omega$  in the same range as Figure 4.6. The dotted lines show the corresponding quasistatic forcing solution, i.e. the harmonic forcing multiplied by the inverse of the average stiffness matrix. It is clearly seen that the third harmonic has a resonance peak near  $1/3$  of the first eigenfrequency and also a secondary peak near  $1/4$  of this frequency. This phenomenon can be observed in nearly all harmonics. The most interesting one is the fourth harmonic, which shows a resonance peak near  $1/4$  of the first eigenfrequency, notwithstanding the fourth harmonic in the forcing is absent. In the non-linear analysis the lower solution around the backbones (Figure 4.6) is unstable and the jump phenomenon can occur. This is not present in the small vibrations model.

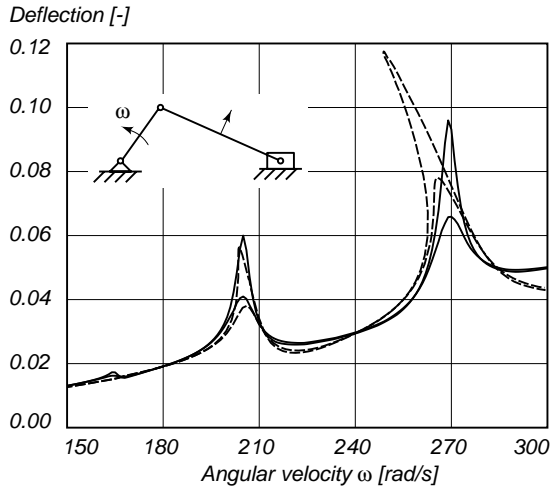


Figure 4.6: Maximal dimensionless midpoint deflections of the periodic solutions for 1% and 2% damping in the driving speed range of  $150 < \omega < 300$  [rad/s]. The drawn lines are the linearized results, the dashed lines are the full non-linear results from Meijaard [45].

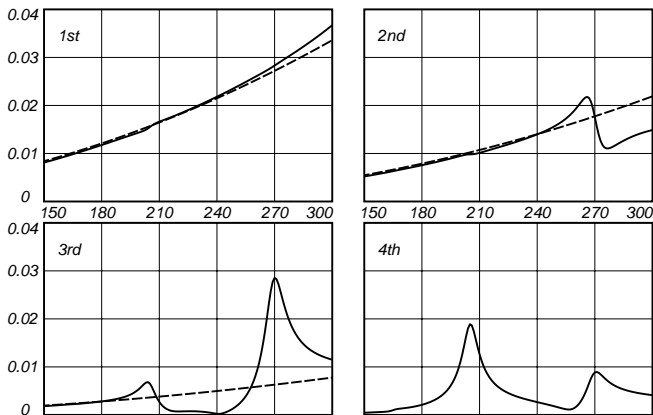


Figure 4.7: The amplitude scaled from 0 to 0.04 of the first four harmonics for 2% damping in the driving speed range of  $150 < \omega < 300$  [rad/s] from Figure 4.6. The dotted lines show the quasistatic forcing solution.

### 4.4.3 Rotor Dynamics Model [48]

The approach of this work can directly be applied to derive rotor dynamic models and to analyse their linearized behaviour. In order to assess the validity and accuracy of the models, a comparison with a problem from literature [81] is made.

By the linearization procedure the structural equations of the rotor system are obtained in a linearized form, and if the original non-linear model is comprehensive, all kinds of effects that give a contribution to the linearized equations, such as load-dependent terms, initial deflections, and mass unbalances, are automatically taken into account. The influence of the rotor speed can be distinguished in linear contributions to the velocity sensitivity matrix  $\mathbf{C}$  and quadratic contributions to the stiffness matrix  $\mathbf{K}$ . This speed dependency can be identified in detail in the individual contributions to the linearized equations of motion as summarized on page 122 of Appendix A. The kinematics of the additional elements such as bearings, seals, squeeze film dampers and air gaps, can be linearized in the same way, as shown in Chapter 2 by Equation (2.15). The constitutive equations of these elements can be added to the structural equations as explained by Equation (2.14). In the context of the present work, these have to be linearized.

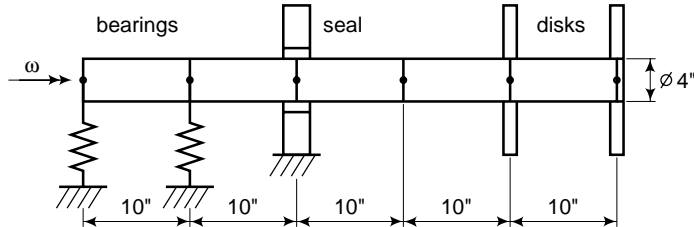


Figure 4.8: Rotor system consisting of a shaft, two isotropic linearly elastic bearings, a seal and two disks.

As the data for the example was originally given by Glasgow and Nelson [18] in imperial technical units, the following conversion factors have been used, where needed:  $1 \text{ [in]} = 0.0254 \text{ [m]}$ ;  $1 \text{ [lb]} = 0.45359237 \text{ [kg]}$ ;  $1 \text{ [lbf]} = 4.4482216 \text{ [N]}$ ; normal acceleration of gravity  $g_n = 9.80665 \text{ [N/kg]}$ .

The example system consists of a solid circular cylindrical shaft of length 50 [in] and diameter 4 [in] made of steel with density  $0.283 \text{ [lb/in}^3\text{]}$  and modulus of elasticity  $3.0 \cdot 10^7 \text{ [lbf/in}^2\text{]}$ , see Figure 4.8. This shaft is supported at one end

and at a position 10 [in] from the same end by isotropic bearings with stiffness 100 000 [lbf/in]. A liquid annular seal is placed 20 [in] from the same end. This seal is not included in the calculation of the nominal solution. The additional forces as in (2.11) exerted on the shaft are given by the linearized equations

$$\begin{bmatrix} f_y \\ f_z \end{bmatrix} = - \begin{bmatrix} K & k \\ -k & K \end{bmatrix} \begin{bmatrix} \Delta y \\ \Delta z \end{bmatrix} - \begin{bmatrix} C & c \\ -c & C \end{bmatrix} \begin{bmatrix} \Delta \dot{y} \\ \Delta \dot{z} \end{bmatrix}. \quad (4.20)$$

Here,  $f_y$  and  $f_z$  are the lateral forces on the shaft,  $\Delta y$  and  $\Delta z$  are the lateral displacements, and  $K = 89\,542$  [lbf/in],  $k = 27\,028$  [lbf/in],  $C = 171.42$  [lbf s/in] and  $c = 12$  [lbf s/in] are the stiffness and damping parameters of the seal. The constitutive equations are the same in a co-rotating reference frame. In addition a part of the mass of the seal, 6.68 [kg], is added to the shaft at the position of the seal. Two disks with mass 0.028 [lbf s<sup>2</sup>/in], axial moment of inertia 0.224 [lbf s<sup>2</sup>in] and transverse moment of inertia 0.114 [lbf s<sup>2</sup>in] are placed at the other end and 10 [in] away from that end.

forward/backward	present	from [81]
forward	-7.97 + 223.62 i	-8.04 + 224.13 i
backward	-45.93 + 226.44 i	-45.87 + 226.05 i
backward	-277.46 + 988.02 i	-277.95 + 988.32 i
forward	-205.18 + 1030.30 i	-205.31 + 1031.00 i
backward	-44.45 + 1893.45 i	-44.30 + 1893.95 i
forward	-45.51 + 1921.67 i	-45.77 + 1922.70 i
backward	-158.01 + 4232.13 i	-158.48 + 4233.10 i
forward	-153.39 + 4302.12 i	-153.89 + 4305.32 i

Table 4.1: Eigenvalues (in [rad/s]) of an example rotor system; the results of the present study and those from [81] are given for comparison.

The eigenfrequencies when the shaft turns at 4000 revolutions per minute are calculated. The shaft is modelled with five finite beam elements of equal length with neglected shear deformations but with inclusion of the rotary inertia of the cross-section of the shaft. As the eigenfrequencies are determined with respect to a co-rotating frame of reference in the present study, the corresponding frequencies with respect to an inertia frame are determined by adding the rotary speed to the frequencies of forward whirling modes and subtracting this speed from the frequencies of backward whirling modes. The first eight eigenvalues are given in Table 4.1; for comparison, the values from [81] are listed in the same table. The differences are less than one percent, despite some difference

in modelling. Note that for the first pair of modes, the forward whirling mode has a lower frequency than the corresponding backward whirling mode.

#### 4.4.4 Cardan Drive Shaft

The dynamic analysis of a flexible drive shaft connected by two universal (or Cardan, or Hooke's) joints is the subject of this example. The input and output shaft are assumed rigid, parallel and rigidly supported in lateral direction. The drive shaft is mounted in the plane of the input and output shaft under a misalignment angle  $\alpha$ . The two universal joints are mounted in such a way that, for a rigid drive shaft, the rotation of the output shaft equals the rotation of the input shaft, see Figure 4.9. The misalignment causes an uneven angular

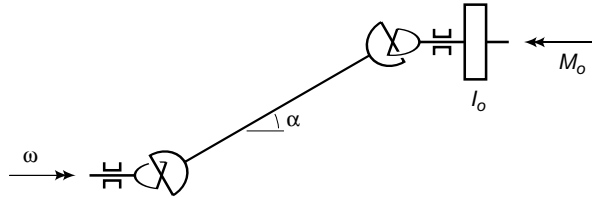


Figure 4.9: Drive shaft connected by two in-plane universal joints.

velocity of the drive shaft of

$$\omega' = \frac{\cos(\alpha)}{1 - \sin^2(\alpha) \sin^2(\omega t)} \omega \quad (4.21)$$

where  $\alpha$  is the angle of misalignment. The corresponding variation of the drive shaft torque at constant output torque  $M_0$  and no inertia is

$$M_t = \frac{1 - \sin^2(\alpha) \sin^2(\omega t)}{\cos(\alpha)} M_0. \quad (4.22)$$

In addition, a bending moment is induced in the drive shaft by the applied torque of

$$M_b = \tan(\alpha) \sin(\omega t) \sqrt{1 - \sin^2(\alpha) \sin^2(\omega t)} M_0. \quad (4.23)$$

These results can be found for instance in [57].

The drive shaft of length 1.0 [m] has a solid circular cross section with radius 0.03 [m]. The shaft made of the steel has a mass density of 7850 [kg/m<sup>3</sup>],

a modulus of elasticity  $E = 210 \cdot 10^9$  [N/m<sup>2</sup>] and Poisson's ratio  $\nu = 0.3$ . The centre line of the shaft is assumed inextensible. The material damping (Kelvin-Voigt) is such that the damping of the first eigenmode for small transverse and torsional vibrations is 1% of critical damping. The flexible shaft is modelled by two beam elements (no shear deflection). The misalignment angle  $\alpha$  is  $\pi/6$  [rad]. At the output side a concentrated moment of inertia  $I_o = 0.345\,555$  [kgm<sup>2</sup>] is attached, simulating the reduced moment of inertia of the driven system. The input shaft is driven at a constant angular velocity  $\omega$  while on the output shaft a constant torque  $M_o = 1060.288$  [Nm] is applied, opposed to the direction of rotation, creating a situation of power transmission. The first two bending eigenfrequencies of the undamped, pin jointed shaft are equal due to its symmetry and can be calculated as  $\omega_b = 766$  [rad/s]. The concentrated moment of inertia,  $I_o$ , is chosen in such a way that, if there is no misalignment, the first torsional eigenfrequency of the undamped shaft (with lumped rotary inertia) equals  $1/\sqrt{2}$  times the first bending eigenfrequency.

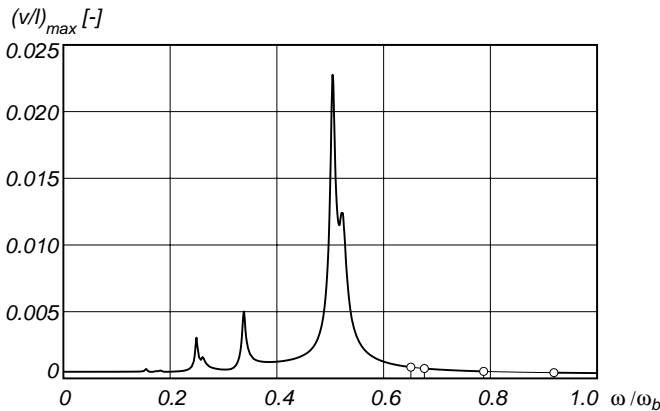


Figure 4.10: Maximal dimensionless midpoint deflection  $(v/l)_{max}$  for the periodic solution of the drive shaft in the driving speed range of  $0 < \omega/\omega_b < 1.0$ . The thin lines between circles are the regions of unstable periodic solutions.

Figure 4.10 shows the maximal dimensionless midpoint deflection of the drive shaft in the lateral plane for the periodic solution for different values of the driving speed  $\omega$ . Resonance occur at about  $1/2$ ,  $1/3$  and  $1/4$  of the first bending eigenfrequency and not at the eigenfrequency itself since the configuration of the shaft with symmetric cross-section has a period of  $\pi$ . It is interesting to see

that the resonances at  $1/2$  and  $1/4$  show two peaks close together: the two initially equal eigenmodes in the lateral plane are separated by the torque load in combination with the misalignment. The thin lines between the circles show the regions of unstable periodic solutions, these zones stretch from  $0.65$  unto  $0.68$  and from  $0.78$  unto  $0.92$ . At the boundaries, a pair of complex conjugate characteristic exponents crosses the imaginary axis and Neimark-Hopf bifurcations occur.

The computational effort for calculating, at every individual driving speed, the gross motion, the linearized equations, and the periodic solution was in the order of one second whereas the effort for determining the stability of the solution, by calculating the characteristic exponents according to (4.15), was in the order of one minute. Algorithms that calculate only a subset of the eigenvalues would speed up the stability analysis.

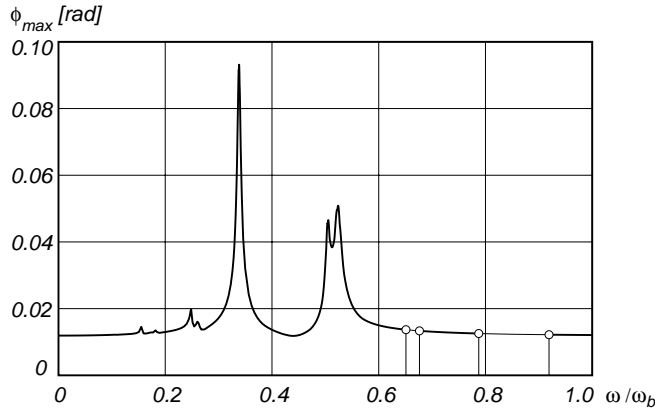


Figure 4.11: Maximal twist angle  $\phi_{max}$  for the periodic solution of the drive shaft in the driving speed range of  $0 < \omega/\omega_b < 1.0$ . The thin lines between circles are the regions of unstable periodic solutions.

Figure 4.11 shows the maximal twist angle between the input and the output end of the shaft for the periodic solution for different values of the driving speed  $\omega$ . Keeping in mind that the first torsional eigenfrequency equals  $1/\sqrt{2}$  times the first bending eigenfrequency  $\omega_b$  we see that resonance clearly occurs at about  $1/2$ ,  $1/3$  and  $1/4$  of the first torsional eigenfrequency. Again resonance at the eigenfrequency itself is not present. The resonance at  $1/2$  of the first bending eigenfrequency is due to the coupling between the bending and the

torsion modes. The maximal twist angle at minimum and maximum driving speed is 0.012 [rad], which is about 20 % higher than the static twist angle at zero misalignment.

Figure 4.12 shows the amplitude on a logarithmic scale of the first seven harmonics of the dimensionless midpoint deflection of the shaft for the periodic solution as a function of the driving speed  $\omega$  in the same range as Figure 4.10.

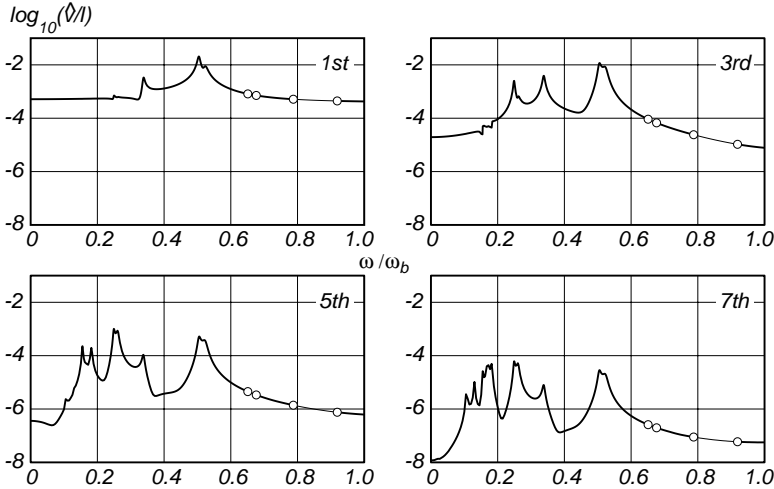


Figure 4.12: The logarithmic amplitude of the first seven harmonics for the dimensionless midpoint deflection  $v/l$  of the drive shaft from Figure 4.10 in the driving speed range of  $0 < \omega/\omega_b < 1.0$ .

All even harmonics are zero due to the symmetry of the system. First of all the coupling between bending and torsion is visible in the deflection at zero speed. Second we clearly see all subharmonics resonance with decreasing amplitudes at increasing harmonics. Figure 4.13 shows the same presentation for the twist angle. Now all odd harmonics are zero due to the symmetry of the system. Harmonic number zero shows the average twist angle which is about constant over the range of speeds. In the second harmonic we clearly see the resonance at  $1/2$  of the first bending eigenfrequency together with resonance at  $1/2$  of the first torsion eigenfrequency. Note the high amplitude contribution of the 4th harmonic at  $\omega_b/2$ .

All results presented here show hardly any difference with full non-linear results.

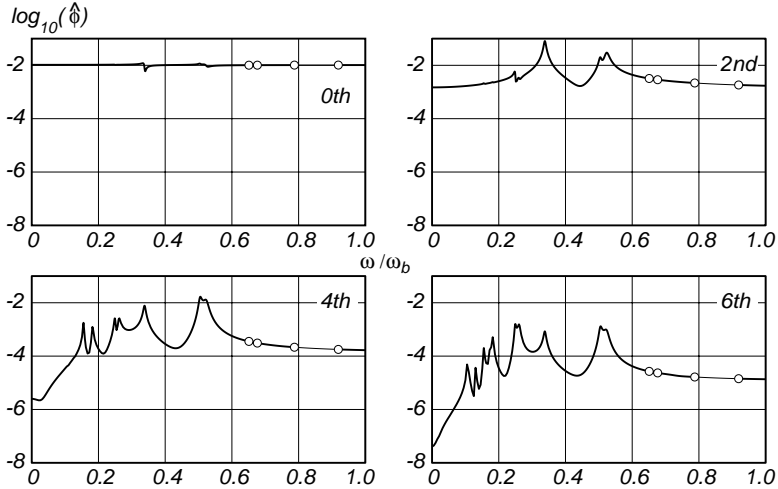


Figure 4.13: The logarithmic amplitude of the first seven harmonics for the twist angle  $\hat{\phi}$  of the drive shaft from Figure 4.11 in the driving speed range of  $0 < \omega/\omega_b < 1.0$ .

#### 4.4.5 Slider-Crank Mechanism with Joint Clearance

In this last example the effect of joint clearance on the dynamic response of an offset slider-crank mechanism is considered. This example illustrates the application of additional applied non-linear forces to the linearized equations of motion that were not included in the calculation of the nominal solution. In this case the non-linear forces originate from the unilateral contact in the clearance joint. The mechanism originates from a publication by Rogers and Andrews [64].

The system, as shown in Figure 4.14, consists of a crank of length 0.0508 [m], a connecting rod of length 0.1524 [m], and a horizontally moving plunger with a vertical offset of 0.0508 [m]. The crank and the connecting rod are modelled as rigid elements. The uniformly distributed mass of the crank and the connecting rod are respectively 0.1366 [kg] and 0.3406 [kg]. The mass of the plunger is 0.3406 [kg]. The joint between the crank and the connecting rod with journal radius 3.18 [mm] has a radial clearance of  $c = 51$  [ $\mu\text{m}$ ]. The contact between the steel journal of the connecting rod and the babbit bearing wall of the crank is approximated linearly with a stiffness of  $1.09 \cdot 10^8$  [N/m] and a material damping

of 100 [Ns/m] according to the Kelvin-Voigt model. Starting from a horizontal position, the crank rotates anticlockwise at a constant angular velocity of  $\dot{\theta} = 150$  [rad/s].

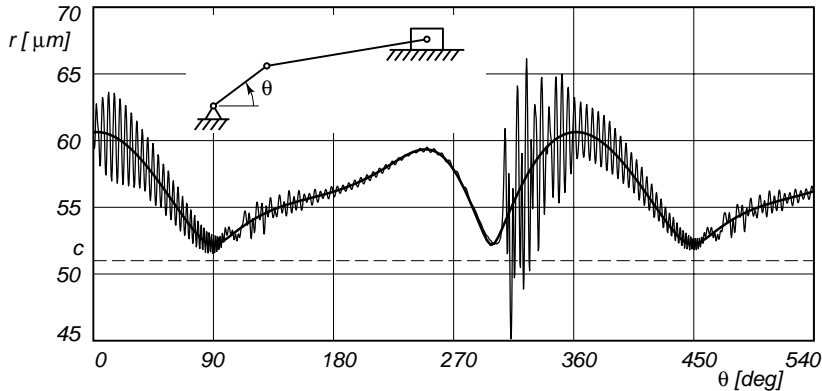


Figure 4.14: Radial journal displacement  $r$  with respect to the crank bearing as a function of the crank angle  $\theta$  for the first one and a half crank revolutions in an offset slider-crank mechanism. The strongly oscillating curve is the total response and the smooth curve represents the periodic solution at zero clearance but with compliance, drawn relative to  $r = c$ .

The effect of the small joint clearance on the dynamic behaviour of the mechanism can be described by the superimposed motion of the journal with respect to the crank bearing. This leads, for the small vibration analysis, to a system with two degrees of freedom, the horizontal and vertical displacement of the journal with respect to the crank bearing reference frame. The forces exerted in the elastic bearing with clearance can be modelled in this small vibration analysis as additional applied non-linear forces.

In a first analysis the dynamic response is calculated taking into account the clearance and compliance in the joint. The nominal motion of the system is with zero clearance and no compliance. The analysis is done by numerical integration of the equations of motion for the small vibration problem with the additional non-linear forces from the unilateral compliant contact in the clearance joint added on the right-hand side. The result of this transient analysis is the strongly oscillating curve in Figure 4.14. The strong oscillation clearly takes place around a smooth curve. This curve represents the periodic solution of the system where the joint is modelled without clearance but with compliance. In the model with

clearance the first contact loss appears at a crank angle of  $312^\circ$  after which several impacts with high amplitudes in the displacement start off the transient again, resulting in a kind of periodic transient behaviour. The contact loss is

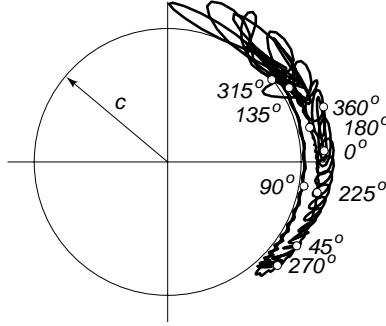


Figure 4.15: Journal centre path with respect to the crank bearing reference frame. Dots with numbers indicate the crank orientation in degrees starting from a horizontal position  $\theta = 0^\circ$ . The first complete revolution is shown.

visualised by the journal centre path with respect to the crank bearing centre in Figure 4.15. This shows that the bearing is only loaded at the outer region and that the contact loss happens due to the sudden change in vertical bearing force after  $\theta = 270^\circ$ . The transient behaviour corresponds very well with the full non-linear results from Rogers and Andrews [64].

In a second analysis the system is even more simplified. The clearance in the compliant joint is disregarded and the periodic solution of the linearized equations of motion is calculated. This result is shown in Figure 4.14 and Figure 4.16 as the smooth curve relative to the horizontal axis  $c$ . The heavily oscillating curve in Figure 4.16 is the total dynamic response, the summed periodic and transient solution. The initial conditions for the transient solution are all taken zero except for the horizontal relative displacement in the bearing being  $3.5 [\mu\text{m}]$  with respect to the periodic solution at  $\theta = 0^\circ$ . This approximates the initial transient of the non-linear analysis from Figure 4.14. There are two grounds for discarding the approximated transient response from Figure 4.16 in comparison with the non-linear results as presented in Figure 4.14. First, there is no onset of transient due to the several impacts at  $\theta = 312^\circ$ . Second, after low force level, around  $\theta = 90^\circ$ , the amplitude of the vibration sustains while in the response of the non-linear model the elastic vibration mode is transformed to a pendulum motion of the journal in the bearing.

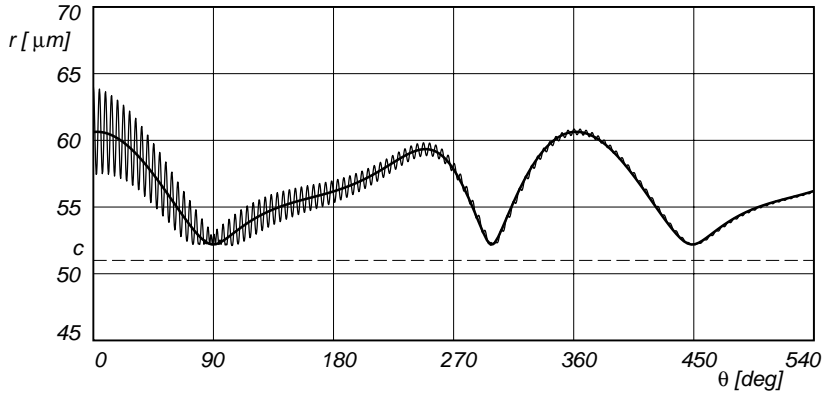


Figure 4.16: Radial journal displacement  $r$  with respect to the crank bearing as a function of the crank angle  $\theta$  for the first one and a half crank revolutions. The smooth curve represents the periodic solution at zero clearance but with compliance, the heavily oscillating curve is the sum of the periodic and the transient solution. Both curves are drawn relative to  $r = c$ .

We conclude by remarking that the approximate periodic solution from the second analysis, at zero clearance but with compliance, can predict the average bearing displacement together with the frequency of the periodic transient. The onset and amplitudes of this transient can not be predicted by this linear model. However, the non-linear vibration analysis on the two degrees of freedom model for small vibrations is far more efficient in computation time than the full analysis on the complete system.



## Chapter 5

# Joint Clearance

ZENO: But in that very short flash, the Tortoise has managed to inch ahead by ever so little, and so Achilles is still behind. Now you see that in order for Achilles to catch the Tortoise, this game of “try-to-catch-me” will have to be played an INFINITE number of times—and therefore Achilles can NEVER catch up with the Tortoise!

TORTOISE: Heh heh heh heh!

ACHILLES: Hmm ...hmm ... hmm ...hmm ...hmm ... That argument sounds wrong to me. And yet, I can't quite make out what's wrong with it.

ZENO: Isn't it a teaser? It's my favorite paradox.

(Douglas R. Hofstadter, *Gödel, Escher, Bach*)

Joint clearances due to manufacturing tolerances and wear can seriously affect the dynamic response of mechanical systems. In unlubricated joints it is usually accompanied by rattling, excessive wear and noise, which is caused by peak contact forces. A critical factor in the precise prediction of the peak forces is the contact model being used. In the past a considerable amount of experimental and theoretical work has been done to study the effect of joint clearances on the dynamic response of mechanical systems. An overview of the English language literature on this subject up to 1980 is given by Haines [21]. In an early German study Hain [20] discusses the effect of radial joint clearance on the forces in an experimental set-up of a scotch-yoke mechanism. After 1980 Soong and Thompson [79] did experimental work on a slider-crank mechanism with revolute joint clearance between the connecting rod and the slider and they made a comparison with calculated results from a rigid-link model. A spatial manipulator with

joint clearance was modelled by Kakizaki *et al.* [34], who included the effects of elastic links and the control system. Deck and Dubowsky [11] published results from experiments on a spatial slider-crank mechanism. The possibility of occurrence of chaotic motion was shown by Seneviratne and Earles [75]. Finally, the treatment of unilateral constraints in a multibody system is described in detail in the book by Pfeiffer and Glocker [59].

This chapter will focus on the modelling of joint clearances in a computer code environment for dynamic analysis of mechanical systems. First of all the kinematics of a planar journal bearing will be discussed. In the subsequent section two continuous contact force models are treated, a Hertzian contact model with dissipation and a lubricated, hydrodynamic bearing model. Both models are applied in illustrative examples. In Section 5.3 the basic equations for a discontinuous contact force model (impact with rebound) in a mechanical system are derived. The numerical aspects of such an analysis are treated in depth and an estimate for the maximum contact force during impact is presented. The various contact models are illustrated for a high-speed slider-crank mechanism with a revolute joint clearance between the connecting rod and the slider. The results for the case of rigid links and Hertzian contact forces obtained with a finite element based multibody software system are compared with results as presented by Ravn [62].

## 5.1 Joint Clearance Model

Joint clearance in a planar revolute joint, see Figure 5.1, is usually modelled by the introduction of two extra degrees of freedom, the horizontal and the vertical displacements,  $x$  and  $y$ , of the journal centre relative to the sleeve centre. If the planar cylindrical bearing element from Section 3.1 is used to model the joint then these displacements are represented by the first two generalized strains  $\varepsilon_1$  and  $\varepsilon_2$  (3.1). Since for a revolute joint the relative rotation is unconstrained, this means that in a non-contact condition, no constraints are introduced by the joint. During contact, the interaction between the two parts in the joint is solely achieved by normal and tangential contact forces. The kinematic contact condition for a revolute joint with radial clearance  $c$  and relative displacements  $x$  and  $y$  is given by

$$g_N = c - \sqrt{x^2 + y^2} \leq 0. \quad (5.1)$$

A situation without contact corresponds to  $g_N > 0$ , whereas contact with local deformation near the contact zone, to be indicated as penetration, is indicated by a negative value of  $g_N$ . When the journal comes into contact with the sleeve

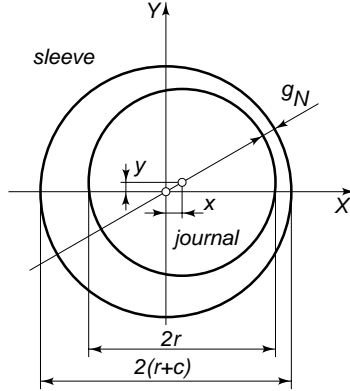


Figure 5.1: Planar revolute joint with clearance.

and the contact is assumed rigid, one degree of freedom is removed from the system. The two remaining degrees of freedom are a relative rotation of the two parts and a rotation of the journal centre around the sleeve centre. In the case of friction in the contact region there is a possibility of sticking. When sticking occurs, again a degree of freedom is removed and there is only one possible relative motion in which the cylindrical surface of the journal rolls without slip along the inner sleeve surface.

## 5.2 Continuous Contact Force Models

### 5.2.1 Hertzian Contact Force Model with Dissipation

Since the primary interest is not the shape nor any other detail of the contact region, we are in need of a global contact model with few parameters. For an unlubricated joint the Hertzian contact force model is an appropriate choice. Whereas the original Hertzian model does not include any energy dissipation, an extension by Lankarani and Nikravesh [40, 41] includes energy loss due to internal damping. In this model the compressive contact force  $F_N$  in terms of the penetration depth  $\delta = -g_N$ , and velocity  $\dot{\delta} = -\dot{g}_N$ , is given by

$$F_N = \begin{cases} K\delta^n + D\dot{\delta} & \delta > 0 \\ 0 & \delta \leq 0 \end{cases} . \quad (5.2)$$

For the frictionless Hertzian contact between two spheres the exponent  $n = 3/2$  and the stiffness parameter  $K$  is given by [23]

$$K = \frac{4}{3\pi(h_1 + h_2)} \sqrt{\bar{R}}, \quad (5.3)$$

where

$$\bar{R} = \frac{R_1 R_2}{R_1 + R_2}; \quad h_i = \frac{1 - \nu_i^2}{\pi E_i} \quad i = 1, 2;$$

with radius  $R_i$ , Poisson's ratio  $\nu_i$  and Young's modulus  $E_i$  associated with each sphere. A form for the hysteretic damping coefficient according to

$$D = H\delta^n, \quad (5.4)$$

was proposed by Hunt and Crossley [27]. The so-called hysteresis damping factor  $H$  can be estimated from a comparison of the energy loss in a central impact of a sphere with a rigid barrier, using Newton's impact law and the present model. The energy loss after impact of a sphere with mass  $m$  at a penetration velocity  $\dot{\delta}^-$  just before impact, and with coefficient of restitution  $e$  according to Newton's impact law, is

$$\Delta T = -\frac{1}{2}(1 - e^2)m(\dot{\delta}^-)^2. \quad (5.5)$$

On the other hand, this energy loss can be expressed by integration of the contact force of the present model (5.2), over one hysteresis loop as

$$\Delta T = -\oint F_N d\delta = -\oint H\delta^n \dot{\delta} d\delta. \quad (5.6)$$

For small energy dissipation, the motion of the sphere can be approximated by the fully elastic motion as

$$\dot{\delta}^2 = \frac{2}{n+1} \frac{K}{m} (\delta_{max}^{n+1} - \delta^{n+1}), \quad (5.7)$$

with the maximum penetration  $\delta_{max}$  as in

$$(\dot{\delta}^-)^2 = \frac{2}{n+1} \frac{K}{m} \delta_{max}^{n+1}. \quad (5.8)$$

Substitution of this motion in the contour integral and evaluation yields

$$\Delta T = -\oint H\delta^n \dot{\delta} d\delta \approx -2 \int_0^{\delta_{max}} H\delta^n \dot{\delta} d\delta = -\frac{2}{3} \frac{H}{K} m (\dot{\delta}^-)^3. \quad (5.9)$$

Equating this with the Newtonian impact law result (5.5), approximates the hysteresis damping factor  $H$  for small energy dissipation as

$$H = \frac{3(1 - e^2)K}{4\dot{\delta}^-}. \quad (5.10)$$

A major drawback of this model is the dependency of the hysteresis damping factor  $H$  on the impact velocity  $\dot{\delta}^-$ . In finding this we have to track down the precise moment of impact which makes the continuous model partly non-smooth. Furthermore it can be shown that the approximate model underestimates the amount of dissipated energy, and consequently results in a higher velocity after impact. For a restitution factor  $e$  of 0.75 and above, the error in the velocity after impact is less than 10%, while the error in the dissipated energy is less than 25%. This contact law is derived for colliding spheres having circular contact regions. In the case of a planar revolute joint we have to deal with cylindrical line contact. This line contact will only be present when we have two extremely precise aligned long cylinders. This is usually not the case and therefore Harris [22] proposes the sphere contact model should be used. According to Ravn [62] this is reasonably close to the more complicated force-displacement relation for cylindrical line contact.

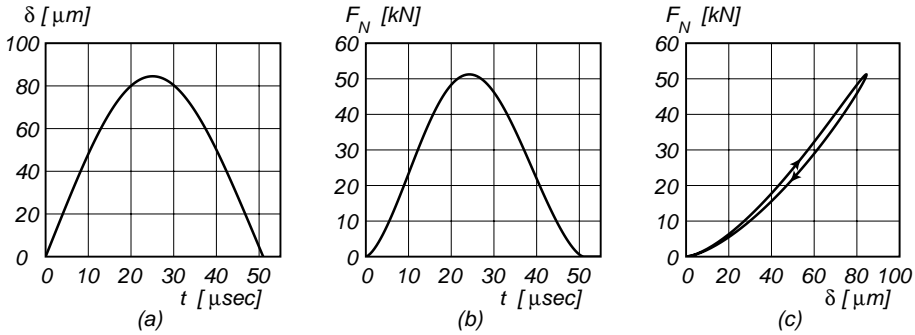


Figure 5.2: Hertzian contact law according to (5.2) with penetration depth  $\delta$ , contact force  $F_N$  and hysteresis loop of an elastic sphere impacting an elastic barrier;  $m = 0.145$  [kg];  $\dot{\delta}^- = 5$  [m/s];  $K = 65.8 \cdot 10^9$  [N/m<sup>1.5</sup>];  $e = 0.95$ .

An illustrative example of the dissipative Hertzian contact force model is an elastic sphere impacting an elastic barrier. The parameters for this example are chosen in conformity with those of the slider-crank example to be discussed in

Section 5.4. The sphere with radius  $R_1 = 9.5$  [mm] and mass  $m = 0.145$  [kg] has an initial velocity just before impact of  $\dot{\delta}^- = 5$  [m/s]. The fixed barrier has a concave spherical curvature with radius  $R_2 = -10.0$  [mm]. The materials in contact have the properties of steel with Young's modulus  $E = 2.06 \cdot 10^{11}$  [N/m<sup>2</sup>], Poisson's ratio  $\nu = 0.3$  and coefficient of restitution  $e = 0.95$ . Figure 5.2 shows the penetration depth, the contact force and the hysteresis loop for a representative impact.

## 5.2.2 Hydrodynamic Contact Force Model

Since most of the joint clearances in mechanisms and machines are in lubricated bearings, a model is needed for this type of bearing. The simplest type of fluid film bearing for a revolute joint is the plane full journal bearing. Rogers and Andrews [64] are among the few who incorporate a simple empirical hydrodynamic bearing model in a linkage dynamic analysis. In the work of Moes *et al.* [51] simple but nevertheless accurate closed-form analytical expressions for the load carrying properties of fluid film bearings are introduced. These solutions are based upon the Reynolds equation for a thin film. Incorporated is the effect of cavitation and the finite length of the bearing. An algorithmic interpretation of their expressions for the determination of the bearing force as a function of the relative position and speed of the journal and the physical parameters of the bearing is presented in Appendix C. This straightforward algorithm can be coded in any numerical procedure. It returns the forces exerted by the fluid film on the sleeve expressed in the Cartesian reference frame  $Oxy$  of the sleeve as

$$\begin{bmatrix} F_x \\ F_y \end{bmatrix} = 2\mu l \left(\frac{r}{c}\right)^3 v_s \begin{bmatrix} \cos \varphi & -\sin \varphi \\ \sin \varphi & \cos \varphi \end{bmatrix} \begin{bmatrix} W_x \\ W_y \end{bmatrix}, \quad (\text{C.11})$$

with journal radius  $r$ , radial clearance  $c$ , bearing length  $l$ , lubricant dynamic viscosity  $\mu$ , pure-squeeze velocity magnitude  $v_s$  and orientation  $\varphi$ , and impedance vector components or dimensionless damping coefficients  $W_x$  and  $W_y$  which are a function of the shape and the state of motion of the bearing.

An example of the quasi-static load carrying capacity of such a lubricated journal bearing is shown in Figure 5.3. The sleeve is fixed and the journal rotates with a constant angular velocity. The bearing force with respect to the fixed frame is calculated as a function of the scaled horizontal position  $x/c$ . In every position the velocities  $\dot{x}$  and  $\dot{y}$  are zero (quasi-static). The bearing dimensions are the same as those of the slider-crank example to be discussed in Section 5.4. From this example a major characteristic of the bearing model is immediately clear: when the journal approaches the sleeve, e.g.  $x/c > 0.95$ , the bearing force

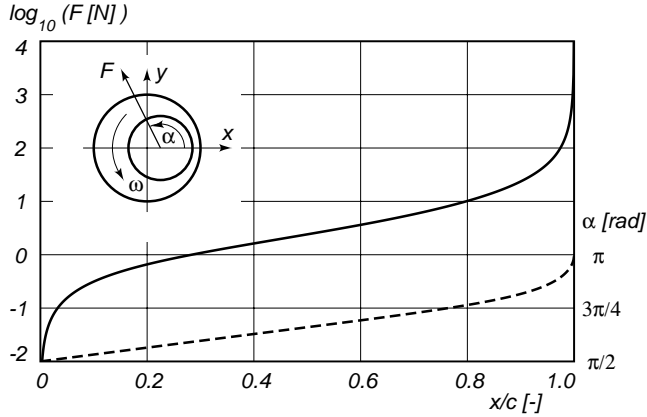


Figure 5.3: Bearing force  $\mathbf{F}$  in magnitude (solid line) and orientation (dashed line) exerted by the lubricant on the journal as a function of the eccentricity  $x/c$  ( $y = 0$ ) for the quasi-static case ( $\dot{x} = 0$  and  $\dot{y} = 0$ ), with a hydrodynamic lubricated bearing according to the model by Moes *et al.* [51];  $\omega = 163.62$  [rad/s];  $r = 10.0$  [mm];  $c = 0.5$  [mm];  $l = 2r$ ;  $\mu = 0.1$  [Ns/m<sup>2</sup>].

increases very rapidly; note the logarithmic scale used. The bearing becomes stiff and the numerical analysis will be sensitive to small errors in the relative journal positions  $x$  and  $y$ .

## 5.3 Discontinuous Contact Force Model

### 5.3.1 Impulse Equations

In the discontinuous contact force model the duration of contact is assumed to be very short in comparison with the time scale of the problem at hand. Under this assumption the change in velocity may be considered as instantaneous and we speak of an impact. The velocity jump is enforced by a very high value of the contact force acting only during a small time interval of contact. In the limit case the force is infinite and the time interval is zero. The integral of the force with respect to time over the duration of the impact, the impulse, has a finite value which is the cause of the velocity jump. While the impact takes place all positions remain constant and all non-impulsive forces of the mechanical system can be neglected. The impact is usually divided into a compression and

an expansion phase. Newton's impact law links these two phases by stating that the relative speed after impact equals  $e$  times the relative speed before impact but it has the opposite direction. The factor  $e$  is the coefficient of restitution. A value of  $e = 1$  corresponds with a fully elastic impact whereas the value of  $e = 0$  represents a completely inelastic impact in which the two parts "stick" together after impact. For an unconstrained mechanical system the equations of motion can be written as

$$\mathbf{M}\ddot{\mathbf{q}} = \mathbf{f}, \quad (5.11)$$

with mass matrix  $\mathbf{M}$ , the accelerations  $\ddot{\mathbf{q}}$  of the generalized coordinates  $\mathbf{q}$  and the sum of all generalized forces  $\mathbf{f}$ . When contact occurs possibly at a number of points, indicated by the vector equation  $\mathbf{g}_N(\mathbf{q}) = \mathbf{0}$ , the system becomes constrained and the equations of motion become

$$\mathbf{M}\ddot{\mathbf{q}} + \mathbf{g}'_N{}^T \boldsymbol{\lambda}_N = \mathbf{f}, \quad (5.12)$$

with the partial derivatives  $\mathbf{g}'_N = \partial \mathbf{g}_N / \partial \mathbf{q}$  and the multipliers  $\boldsymbol{\lambda}_N$  dual to the relative contact velocities  $\dot{\mathbf{g}}_N$ . These multipliers can be interpreted as the contact forces. Integration of these equations of motion over the time of impact and taking the limit case yields

$$\lim_{t^- \uparrow t^+} \int_{t^-}^{t^+} (\mathbf{M}\ddot{\mathbf{q}} + \mathbf{g}'_N{}^T \boldsymbol{\lambda}_N) dt = \mathbf{0}. \quad (5.13)$$

The generalized forces  $\mathbf{f}$  only contain non-impulsive forces and therefore the right-hand side vanishes. Under the introduction of the contact impulses,

$$\mathbf{s}_N = \lim_{t^- \uparrow t^+} \int_{t^-}^{t^+} \boldsymbol{\lambda}_N dt, \quad (5.14)$$

and noting that the mass matrix, in general a function of the generalized coordinates, stays constant during impact, the momentum equations for the mechanical system become

$$\mathbf{M}\dot{\mathbf{q}}^+ + \mathbf{g}'_N{}^T \mathbf{s}_N = \mathbf{M}\dot{\mathbf{q}}^-, \quad (5.15)$$

with  $\dot{\mathbf{q}}^-$  the generalized velocities before and  $\dot{\mathbf{q}}^+$  the generalized velocities after impact. Together with Newton's impact law,

$$\dot{\mathbf{g}}_N^+ = -e\dot{\mathbf{g}}_N^-, \quad \text{or} \quad \mathbf{g}'_N \dot{\mathbf{q}}^+ = -e\mathbf{g}'_N \dot{\mathbf{q}}^-, \quad (5.16)$$

we have a complete set of linear equations reading

$$\begin{bmatrix} \mathbf{M} & \mathbf{g}'_N{}^T \\ \mathbf{g}'_N & \mathbf{0} \end{bmatrix} \begin{bmatrix} \dot{\mathbf{q}}^+ \\ \mathbf{s}_N \end{bmatrix} = \begin{bmatrix} \mathbf{M}\dot{\mathbf{q}}^- \\ -e\mathbf{g}'_N\dot{\mathbf{q}}^- \end{bmatrix}. \quad (5.17)$$

From these equations the velocities after impact  $\dot{\mathbf{q}}^+$  together with the contact impulses  $\mathbf{s}_N$  can be found. Because Newton's impact law (5.16) is often contradicted experimentally in case of multiple impacts, a restriction to simple impacts is made. With one impact occurring at a time the resulting contact impulse can be solved as

$$\mathbf{s}_N = (1 + e)m_e\mathbf{g}'_N\dot{\mathbf{q}}^-, \quad (5.18)$$

where the effective mass  $m_e$  is given by the expression

$$m_e = 1/(\mathbf{g}'_N\mathbf{M}^{-1}\mathbf{g}'_N{}^T). \quad (5.19)$$

The velocities after impact are given by

$$\dot{\mathbf{q}}^+ = \dot{\mathbf{q}}^- - \mathbf{M}^{-1}\mathbf{g}'_N{}^T\mathbf{s}_N. \quad (5.20)$$

The change of energy during impact is equal to the difference of the kinetic energy before and after the impact yielding

$$\Delta T = -\frac{1}{2}(1 - e^2)m_e(\dot{g}_N^-)^2. \quad (5.21)$$

Since the coefficient of restitution  $e$  is between zero and one, the impact will always be dissipative except for the limit case  $e = 1$ , where we have energy conservation.

### 5.3.2 Numerical Aspects of Impact Analysis

In a joint having a clearance three distinct states are to be observed: free flight where there is no contact between the two parts, impact and permanent contact. In doing the numerical calculations it is very important to find the precise moment in time of transition between these different states. If not, there will be a build-up of errors and the final results are inaccurate. If we rely on the integration routine to do this job it has to step back and take smaller steps until a step is taken within the error tolerance. The transition from an impacting motion to permanent contact leads to an infinite number of impacts in a finite period of time, a so-called finite time singularity. Very slowly we shall

reach the moment where the journal will come into permanent contact with the sleeve. Compare this to the Achilles and tortoise argument of Zeno of Elea [37]. In the next three subsections the handling of the different transitions will be treated.

### Contact Detection

Usually coming into contact is detected by a change of sign in the distance  $g_N$  between the discrete moments in time  $t_n$  and  $t_{n+1}$ ,

$$g_N(\mathbf{q}(t_n))g_N(\mathbf{q}(t_{n+1})) < 0. \quad (5.22)$$

This zero crossing of  $g_N(\mathbf{q}(t))$  can be found with the help of a bisection or a Newton-Raphson procedure. In both cases we need to calculate intermediate values of  $\mathbf{q}(t)$ . A fast and accurate approach, as proposed by Meijaard [46], uses a third-order interpolation polynomial between the already calculated positions and velocities at  $t_n$  and  $t_{n+1}$ . This interpolation reads

$$\begin{aligned} \mathbf{q}(t) = & (1 - 3\xi^2 + 2\xi^3)\mathbf{q}(t_n) + (\xi - 2\xi^2 + \xi^3)h\dot{\mathbf{q}}(t_n) \\ & + (3\xi^2 - 2\xi^3)\mathbf{q}(t_{n+1}) + (-\xi^2 + \xi^3)h\dot{\mathbf{q}}(t_{n+1}), \end{aligned} \quad (5.23)$$

with  $\xi = (t - t_n)/h$  and  $h = t_{n+1} - t_n$ . By interpolation of the generalized coordinates  $\mathbf{q}(t)$  and evaluation of the distance function  $g_N(\mathbf{q}(t))$  the moment of contact can be calculated within a given error tolerance. We thus avoid repetitive calculation of the accelerations from the system equations to find the zero crossing.

### Permanent Contact

Just as with a bouncing ball on a horizontal plane, the journal may tend to stay in permanent contact with the sleeve. In the analysis this is often recognized as a rapidly increasing number of impacts with decreasing impulses. On the basis of slowly varying forces the motion, after impact with such a low impact velocity, can be estimated by a constant acceleration flight,

$$g_N(t_n + h) = \dot{g}_N(t_n)h + \frac{1}{2}\ddot{g}_N(t_n)h^2. \quad (5.24)$$

The next moment of contact is estimated by setting  $g_N(t_n + h)$  to zero from which we come up with an estimated duration between contacts,

$$h_c = -2\frac{\dot{g}_N}{\ddot{g}_N}. \quad (5.25)$$

If this estimated duration is within the integration timestep, contact within one integration step is highly probable. The time in which permanent contact will occur can be estimated by assuming a number of subsequent impacts with coefficient of restitution  $e$ . After the first impact, the impact velocity is reduced by a factor  $e$  while the acceleration,  $\ddot{g}_N$ , more or less stays the same. The estimated duration for permanent contact is the sum of the infinite sequence of durations given by

$$h_\infty = h_c + eh_c + e^2h_c + \dots = \frac{1}{1-e}h_c. \quad (5.26)$$

If, at impact, this estimated  $h_\infty$  is less than the integration step size  $h$ , permanent contact is assumed. The configuration of the system at permanent contact is found by first interpolating the generalized positions and velocities at the time of impact,  $t = t_n + h_c$ , and then doing a fully inelastic impact calculation.

If the two parts are in permanent contact the equations of motion for this constrained mechanical system are according to (5.12). These together with the contact condition  $g_N = 0$  lead to a mixed set of ordinary differential and algebraic equations (DAEs).

$$\begin{bmatrix} \mathbf{M} & \mathbf{g}'_N{}^T \\ \mathbf{g}'_N & \mathbf{0} \end{bmatrix} \begin{bmatrix} \ddot{\mathbf{q}} \\ \lambda_N \end{bmatrix} = \begin{bmatrix} \mathbf{f} \\ -\mathbf{g}''_N \dot{\mathbf{q}} \dot{\mathbf{q}} \end{bmatrix} \quad (5.27)$$

These equations can be solved in various ways. In our approach the system equations are transformed in terms of independent coordinates. The resulting ordinary differential equations for the position and velocities of the independent coordinates can be numerically integrated by any scheme. A fast and accurate method, which exploits the second-order structure of the equations of motion, is the explicit one stage method as proposed by Meijaard [44]. With the second-order differential equations of the equations of motion given by  $\ddot{\mathbf{q}}(t, \mathbf{q}, \dot{\mathbf{q}})$ , where the set of independent coordinates is denoted by  $\mathbf{q}$ , the method can be described as

$$\begin{aligned} \mathbf{k}_1 &= \ddot{\mathbf{q}}(t_n + \frac{1}{2}h, \mathbf{q}_n + \frac{1}{2}h\dot{\mathbf{q}}_n, \dot{\mathbf{q}}_n) \\ \mathbf{q}_{n+1} &= \mathbf{q}_n + h\dot{\mathbf{q}}_n + \frac{1}{2}h^2\mathbf{k}_1 \\ \dot{\mathbf{q}}_{n+1} &= \dot{\mathbf{q}}_n + h\mathbf{k}_1. \end{aligned} \quad (5.28)$$

The order of the method is 1, but if the accelerations depend weakly on the velocities the scheme shows order 2 behaviour. Investigation of the stability of the method shows that undamped systems can be integrated in a numerically stable way for step sizes smaller than 2 over the largest eigenfrequency of the mechanical system. Other methods like the classical fourth-order Runge-Kutta

method or the explicit predictor/corrector algorithm as described (and coded) by Shampine and Gordon [77], have also been used with success.

### Loss of Contact

The loss of contact can be detected by monitoring the contact force  $\lambda_N$ . If this force becomes positive, i.e. tension in the contact region, the contact condition,  $g_N = 0$ , has to be dropped. In finding the zero crossing of the contact force intermediate values can be calculated with the mixed differential and algebraic equations from (5.27). For the intermediate values of  $\mathbf{q}$  and  $\dot{\mathbf{q}}$  the same third order interpolation polynomial as in (5.23) can be used. On the other hand, if a numeric integration scheme with intermediate steps is used, like for instance the classical fourth-order Runge-Kutta method, the intermediate values of the contact force can be used for direct interpolation in time. This is a fast and accurate method. In the case of having an intermediate value at the midpoint  $h/2$  the second order interpolation yields

$$\lambda_N(t) = (1 - 3\xi + 2\xi^2)\lambda_{N0} + (4\xi - 4\xi^2)\lambda_{Nh/2} + (-\xi + 2\xi^2)\lambda_{Nh} \quad (5.29)$$

with  $\xi = (t - t_n)/h$  and  $h = t_{n+1} - t_n$ , the contact force  $\lambda_{N0}$  at the beginning,  $\lambda_{Nh/2}$  at the midpoint, and  $\lambda_{Nh}$  at the end of the step.

### Maximum Contact Force Estimation

The maximum contact force can be estimated from the contact impulse  $s_N$  and the elastic material properties of the joint. We shall assume a non-dissipating contact force model according to

$$F_N = K\delta^n. \quad (5.30)$$

The maximum indentation is calculated from the balance of the kinetic energy just before impact and the elastic energy at maximum indentation,

$$\frac{1}{2}m_e(\dot{\delta}^-)^2 = \frac{1}{n+1}K\delta_{max}^{n+1}, \quad (5.31)$$

where  $m_e$  is the effective mass (5.19) of the mechanical system at the contact location. With the contact impulse  $s_N = m_e\dot{\delta}^-$  the maximum indentation yields

$$\delta_{max} = \left( \frac{n+1}{2} \frac{s_N^2}{m_e K} \right)^{\frac{1}{n+1}}, \quad (5.32)$$

and the estimated maximum contact force is given by

$$F_{Nmax} = \left( \frac{n+1}{2} \frac{K^{\frac{1}{n}}}{m_e} s_N^2 \right)^{\frac{n}{n+1}}. \quad (5.33)$$

In the case of a Hertzian contact,  $n = 3/2$  in the above expressions, whereas in the case of a linear spring the exponent  $n$  is one and the maximum contact force yields

$$F_{Nmax} = \omega_c s_N, \quad (5.34)$$

where we have introduced the natural contact frequency

$$\omega_c = \sqrt{\frac{K}{m_e}}. \quad (5.35)$$

In the expression for the contact force (5.34) we clearly recognize the impact  $s_N$  being a product of a high force  $F_{Nmax}$  and a short time period  $1/\omega_c$ . The approximation for the maximum contact force only holds for high contact frequencies in comparison to the other natural frequencies of the system.

## 5.4 Application to a Slider-Crank Mechanism

A slider-crank mechanism is used as an example to illustrate the effect of the different types of joint clearance models. The same mechanism has been used as an example by Ravn [62], which allows us to compare some results. The mechanism,

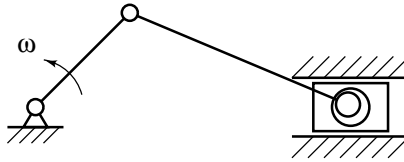


Figure 5.4: Slider-crank mechanism with radial clearance at the slider revolute joint.

as shown in Figure 5.4, consists of a rigid crank of length 0.05 [m], a rigid or elastic connecting rod of length 0.12 [m] and flexural rigidity  $EI = 6.2146 \cdot 10^3$  [Nm<sup>2</sup>], and a slider. The slider mass and the uniformly distributed mass of the connecting rod are both 0.145 [kg]. The crank rotates at a constant angular velocity

$\omega = 523.6$  [rad/s]. The revolute joint between the connecting rod and the slider is modelled with joint clearance. The journal radius is  $9.5$  [mm] while the sleeve radius is  $10.0$  [mm]. The width of the joint is  $20.0$  [mm]. The materials in contact have the properties of steel with Young's modulus  $E = 2.06 \cdot 10^{11}$  [N/m<sup>2</sup>], Poisson's ratio  $\nu = 0.3$ , coefficient of restitution  $e = 0.95$  and we assume no friction. For the fluid film lubricated journal bearing a lubricant dynamic viscosity of  $\mu = 0.1$  [Ns/m<sup>2</sup>] is used. In the initial configuration the slider is in the top dead centre and the journal centre displacements and velocities are taken to be zero. Four different cases will be considered. First, all links are considered to be rigid bodies and a Hertzian contact force model is used at the revolute slider joint. Second, again all links are rigid but an impact model at the revolute slider joint is used. Third, a rigid crank and an elastic connecting rod, and a Hertzian contact force model at the revolute slider joint are used. Fourth, all links are assumed to be rigid bodies and a hydrodynamic lubricated bearing at the revolute slider joint is used.

Since clearances are typically at least a hundred times smaller than link lengths the effect of the clearance can be treated as a small perturbation on the ideal kinematic motion. This same argument is used by Dubowsky and Gardner [13]. The perturbations, being the small displacements in the joint, are handled with the concept of small vibrations superimposed on non-linear rigid body motion as described in Chapter 4.

### 5.4.1 Continuous Hertzian Contact Force Model

In this first case the links are considered to be rigid bodies and the contact force model for the revolute joint at the slider is of the Hertzian type. This corresponds to the example as given by Ravn [62]. The line contact in the revolute joint will only be present for two cylinders aligned with extreme precision. Also, a uniform force distribution over the length of the joint can only be the case if we neglect the boundary effects. With these arguments we propose to use the Hertzian contact force law between two spheres. With the example parameters from above the Hertzian stiffness coefficient (5.3) can be calculated with  $R_1 = 9.5$  [mm] and  $R_2 = -10.0$  [mm] as  $K = 65.8 \cdot 10^9$  [N/m<sup>1.5</sup>]. The slider accelerations and velocities for the time interval of two crank revolutions, after the transient has died out, are shown in Figure 5.5. In the first half of the time interval the accelerations show smooth changes while in the second half they show high peak values which immediately drop back to zero. These zero accelerations indicate the free flight of the slider and consequently the occurrence of impacts in the joint. This is confirmed by step-like changes of the

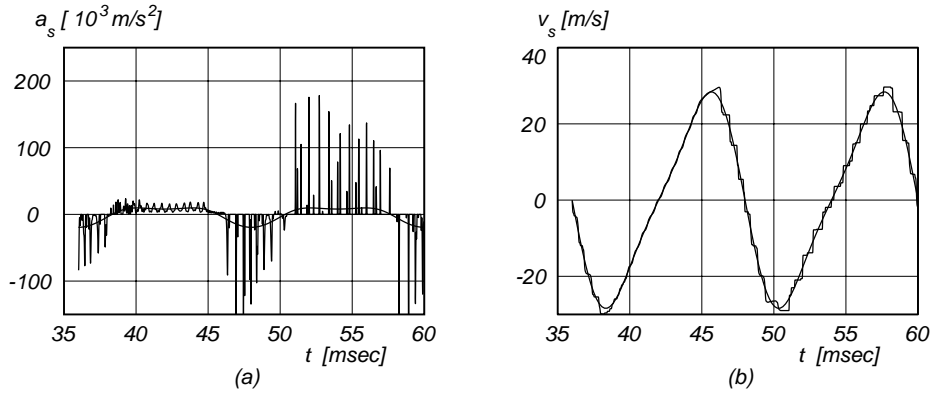


Figure 5.5: Acceleration (a) and velocity (b) of the slider for the case of rigid links and a Hertzian contact force model. The smooth curves correspond to the case without clearance. The shown time interval corresponds to two crank revolutions.

velocity during this second half of the interval. The torque applied to the crank to maintain constant angular velocity is shown in Figure 5.6. Here again we observe the high peak values due to the impacts. The rigid slider and crank propagate the high peak forces at the joint instantaneously to the crank. In the path of the journal centre as shown in Figure 5.6, we recognize the different contact modes: free flight, impact with rebound, and permanent contact. The excursions outside the clearance circle are due to the local Hertz deformations. The dots are plotted equidistantly in time. Results correspond well with those from Ravn [62].

#### 5.4.2 Impact Model with Estimated Maximum Contact Force

In this second case the links are again assumed rigid but the interaction in the revolute joint with clearance is modelled by elastic impacts with dissipation. These impacts give rise to discontinuous forces in the joint and jumps in the velocities of the system. The maximum contact force which occurs during the short period of impact is estimated with the simple model from Section 5.3.2. The slider acceleration and velocity for the time interval of two crank revolutions, after the transient has died out, are shown in Figure 5.7. The slider acceleration

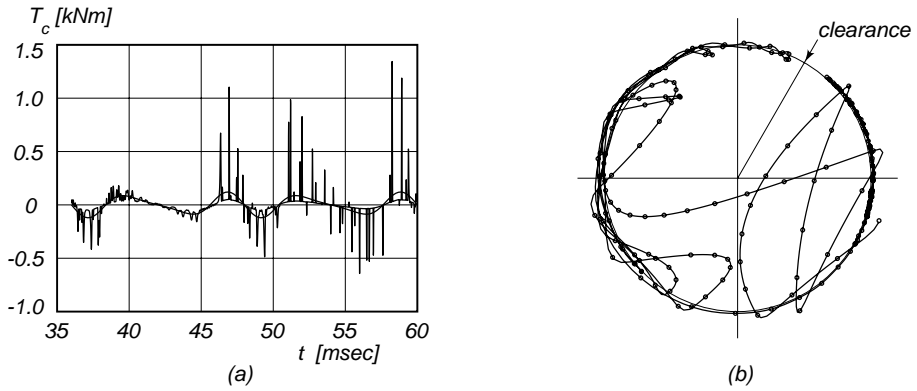


Figure 5.6: Torque acting on the crank (a) and journal centre path (b) for the case of rigid links and a Hertzian contact force model. The smooth curve corresponds to the case without clearance. The shown time interval corresponds to two crank revolutions.

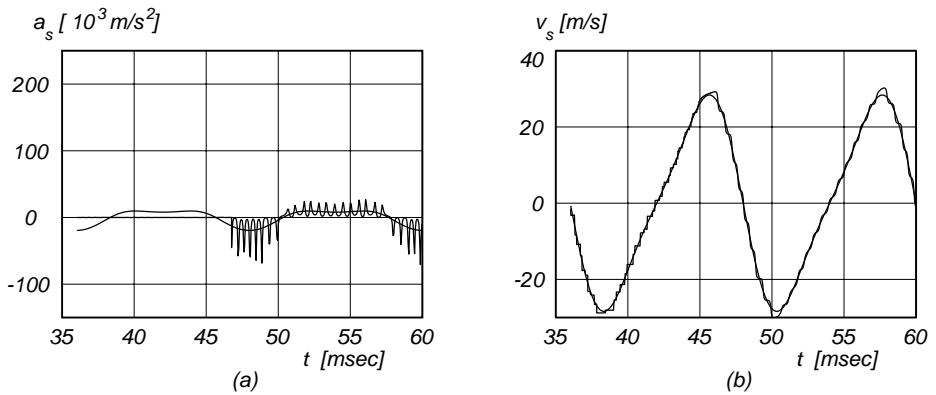


Figure 5.7: Acceleration (a) and velocity (b) of the slider for the case of rigid links and an impact contact model. The smooth curves correspond to the case without clearance. The shown time interval corresponds to two crank revolutions.

is zero during most of the first crank revolution. This means that the slider is solely moved by impacts. These impacts can clearly be seen in the staircase-like slider velocity during this first half of the time interval. The second half of the time interval shows permanent contact. The acceleration and velocity oscillate, owing to the tangential oscillation of the journal in the sleeve in the absence of friction, around the smooth curve of the rigid solution. In Figure 5.8 showing the torques acting on the crank, vertical lines are drawn representing the maximum torques due to the estimated maximum contact forces according to (5.34). These estimates match well in magnitude and in mutual distance with the high

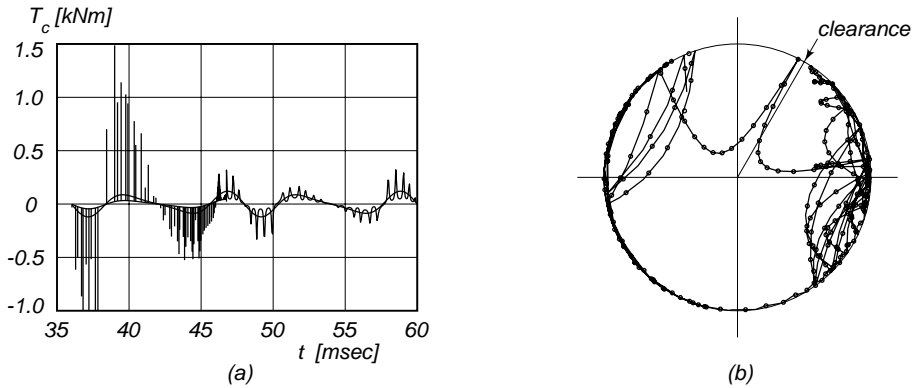


Figure 5.8: Torque acting on the crank (a) and journal centre path (b) for the case of rigid links and an impact contact model. In the left figure, the smooth curve corresponds to the case without clearance and the vertical lines indicate the contribution to the torque from the estimated maximum contact force during impact. The shown time interval corresponds to two crank revolutions.

torque peaks during the second half of the time interval for the Hertzian contact model from Figure 5.6. At the end of the first crank revolution in Figure 5.8, a smooth transition from the estimated maximum torque during impact in the permanent contact torque can be observed. In the path of the journal centre we recognize again the different contact modes: free flight, impact with immediate rebound, and permanent contact. The dots are plotted equidistantly in time. Note the zero penetration depths.

### 5.4.3 Continuous Hertzian Contact Force Model and Elastic Connecting Rod

In this third case we model the connecting rod as an elastic Euler-Bernoulli beam and the crank as a rigid body, and we use the Hertzian contact force model at the slider joint. The centre line of the connecting rod is assumed inextensible since the frequencies of the axial modes are considerably higher than the frequency of the first bending mode. The material damping in the connecting rod is considered such that the damping of the first eigenmode for small vibrations is 1% of the critical damping. The connecting rod is modelled by two planar beam elements. The model has six degrees of freedom; two degrees of freedom result from the joint clearance and four degrees of freedom describe the bending of the connecting rod. Results are shown in Figures 5.9 and 5.10. The elasticity of the connecting rod has a smoothing effect. Compared with the

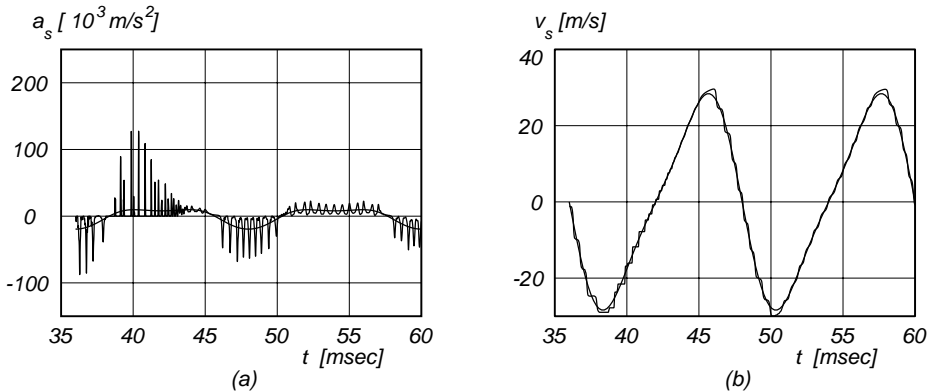


Figure 5.9: Acceleration (a) and velocity (b) of the slider for the case of an elastic connecting rod and a Hertzian contact force model. The smooth curves correspond to the case without clearance. The shown time interval corresponds to two crank revolutions.

case where the connecting rod is modelled as a rigid body (Section 5.4.1), the maximum acceleration is reduced from  $180 \cdot 10^3$  [m/s<sup>2</sup>] to  $120 \cdot 10^3$  [m/s<sup>2</sup>] and the maximum driving torque from 1.35 [kNm] to 0.85 [kNm]. The compliant elements act as a suspension. This effect of elasticity of the links was also noted by Dubowsky and Gardner [13]. During the first crank revolution a high-frequency response in the torque acting on the crank can be observed, see

Figure 5.10. This is due to high velocity impacts which excite the first and

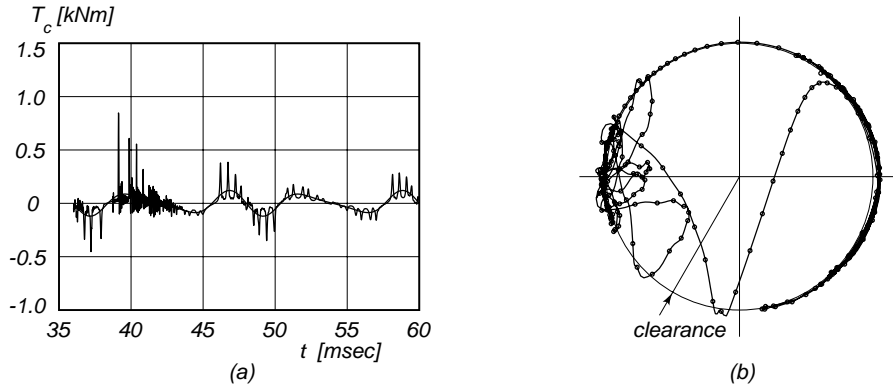


Figure 5.10: Torque acting on the crank (a) and journal centre path (b) for the case of an elastic connecting rod and a Hertzian contact force model. The smooth curve corresponds to the case without clearance. The shown time interval corresponds to two crank revolutions.

second bending eigenmode of the connecting rod. These eigenfrequencies can be estimated from a simply supported beam model as  $\omega_{b1} = 49 \cdot 10^3$  [rad/s] and  $\omega_{b2} = 197 \cdot 10^3$  [rad/s], and compared with the first eigenfrequency for axial vibrations  $\omega_a = 268 \cdot 10^3$  [rad/s] justify the assumption of the inextensible beam model. The natural contact frequency as in (5.35) is  $\omega_c = 80 \cdot 10^3$  [rad/s], and lies between the first and the second bending eigenfrequency of the rod. The recurring impacts with rebound can also be observed in the journal centre path.

#### 5.4.4 Continuous Contact Force Model with Hydrodynamic Lubricated Bearing

In this fourth case the links are considered rigid bodies and the revolute slider joint is modelled with a hydrodynamic lubricated fluid film bearing as presented in Appendix C. Looking at the results for this case, Figures 5.11 and 5.12, we see that they are almost the same as for the system without clearance, being the results for the nominal gross motion which are represented by the smoother curves in all figures. The responses differ only slightly when the slider acceleration has to change sign. The horizontal bearing force  $F_x$  has to change sign and the bearing can only supply this by a flight of the journal across the

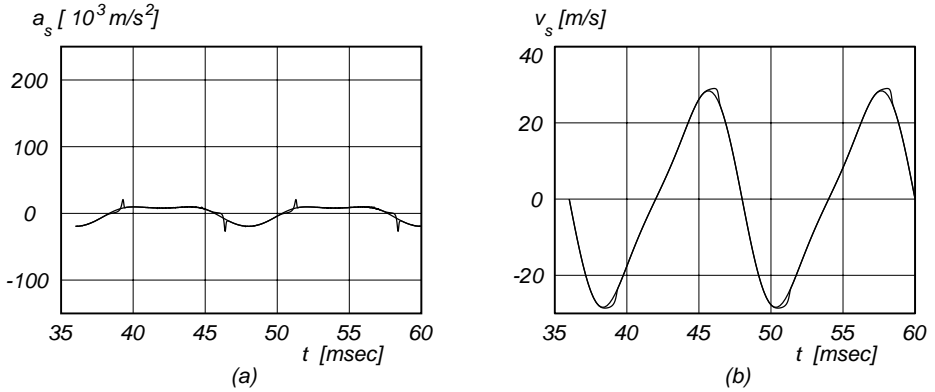


Figure 5.11: Acceleration (a) and velocity (b) of the slider for the case of rigid links and a hydrodynamic lubricated bearing model. The smoother curves correspond to the case without clearance. The shown time interval corresponds to two crank revolutions.

sleeve. This can be seen in the journal centre path diagram, Figure 5.12. This crossing will involve high journal centre speeds and subsequently will give rise to peak forces. The velocity of the slider shows clearly that at the extremes it has a tendency to lag behind. Note the steady state behaviour; the first and the second shown crank revolution are practically the same. In the bearing force locus, Figure 5.13, the peak force after a change of sign of the horizontal bearing force  $F_x$  is evident. The peak force at high velocity and the high stiffness at maximum radial displacement can be observed in Figure 5.14, the figure presents a 3-D diagram of the magnitude of the bearing force versus the radial displacement and the radial velocity.

## 5.5 Discussion

The results as obtained with the impact model compare well with those from the Hertzian contact force model. Both models can predict the dynamic response of mechanisms and machines having unlubricated revolute joint clearance, including the peak values of the forces and position and velocity deviations due to the clearance. However, the impact model requires much less computational effort.

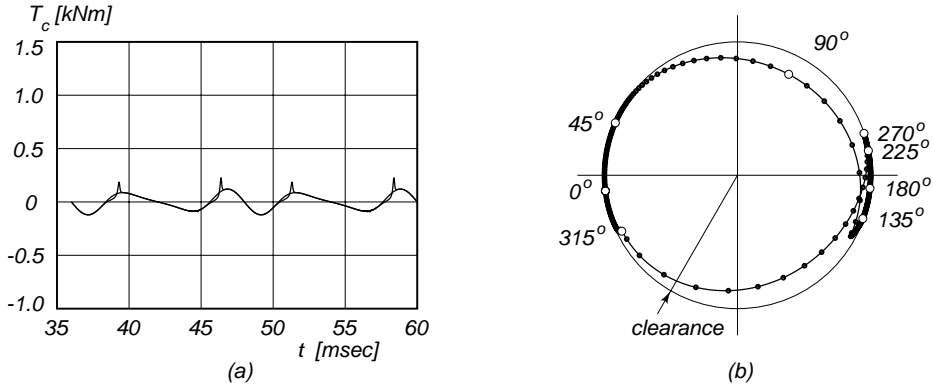


Figure 5.12: Torque acting on the crank (a) and journal centre path (b) for the case of rigid links and a hydrodynamic lubricated bearing model. The smooth curve in the left figure corresponds to the case without clearance, the dots with numbers in the righthand figure indicate the corresponding crank angles. The shown time interval corresponds to two crank revolutions.

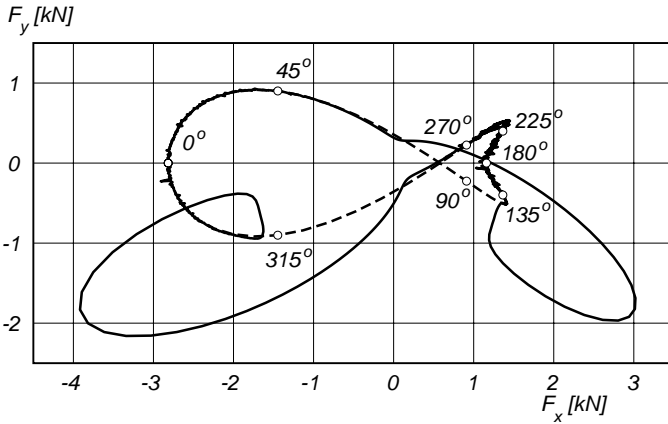


Figure 5.13: Bearing force locus for the case of rigid links and a hydrodynamic lubricated bearing model. Dots with numbers indicate the corresponding crank angles. The dashed curve corresponds to the case without clearance.

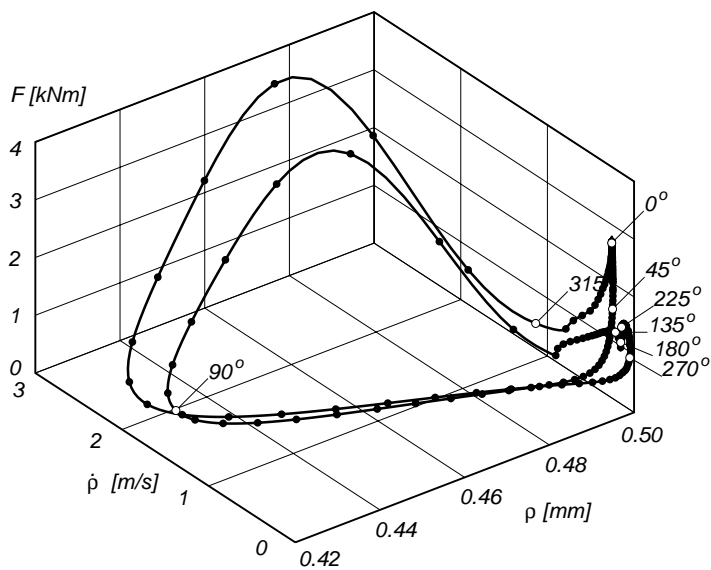


Figure 5.14: Magnitude of the bearing force  $\mathbf{F}$  plotted against the radial displacement  $\rho$  and the radial velocity  $\dot{\rho}$  for the case of rigid links and a hydrodynamic lubricated bearing model. Dots with numbers indicate the corresponding crank angles.

In the case of a hydrodynamic oil film lubricated bearing the joint forces develop much smoother and the peak values are significantly reduced compared with the unlubricated case. A similar but far smaller reduction can be observed when the links are no longer stylized as rigid links but are modelled as elastic elements. The position and velocity deviations of the system due to the clearance stay approximately the same in both cases. The closed-form analytical expressions for the load bearing properties of a hydrodynamic lubricated fluid film bearing as described by Moes *et al.* [51] fit well in the numerical procedure. One numerical complication is the high stiffness at large eccentricity.

Because of the uncertainty of the unlubricated bearing properties such as the coefficient of restitution and friction, it is recommended that the different models presented in this chapter be tested experimentally. Furthermore, it is recommended that the effect of dry friction be incorporated in the analysis of unlubricated joints in spite of the complexity that this may add to the analysis. For example the friction coefficient will have a significant influence on the tangential oscillations shown in Figure 5.7 for the frictionless case.



# Chapter 6

## Concluding Remarks



(Johann Sebastian Bach, Opening chorus from *Cantate 125* (1725))

### 6.1 Conclusions

A method has been described for the calculation of small vibrations superimposed on a nominal rigid body motion of flexible multibody systems. Periodic solutions as well as transient responses can be determined. A method directly based on the Floquet theory has been used successfully to determine the stability of the periodic solutions. Instability of these solutions generally shows itself by a large increase of the amplitude of the solution, where the linearization loses its value. However, in other cases, like for instance the cardan drive shaft example from Section 4.4.4, the solution may lose its stability in a Neimark-Hopf (secondary Hopf) bifurcation without a large increase in amplitude and with negligible non-linear effects.

The method is computationally efficient in comparison with a full non-linear analysis, especially if the system is stiff, that means, high eigenfrequencies relative to the driving frequency are present, or close to resonance peaks. The calculation of the stability may cost a factor ten more computer time than the determination of the periodic solution itself.

The presented belt and pulley pair and the gear pair finite element type are very well applicable to the kinematic and dynamic analysis of complex mechanisms and machines. The presented wheel-on-surface finite element opens a wide field of application for the kinematic and dynamic analysis of multibody systems having rolling contacts as in road vehicle systems. The formulated equations of motion for flexible non-holonomic systems and their linearization can be used to predict the stability of systems in steady motion. These methods have successfully been applied to the modelling and dynamic analysis of the Bombardier-ILTIS road vehicle. The application of quaternion algebra on the Euler parameters gives much insight in the description of relative orientation in space and allows an elegant formulation for a spatial hinge element that still can bend.

The effect of joint clearance on the dynamic response of flexible multibody systems can be predicted by the presented discontinuous contact force model. Together with the impact force prediction this gives insight in force peaks and in position and velocity deviations of the system. The results from this model compare very well with the continuous Hertzian contact model. The impact model together with the concept of small vibrations superimposed on non-linear rigid body motion makes the computation highly efficient. Link flexibility has often to be introduced to obtain accurate contact forces. In the case of a hydrodynamic oil film lubricated bearing the force peaks are small. The maximal position and velocity deviations of the system due to the clearance are approximately the same for all contact models. The closed-form analytical expressions for the load bearing properties of a fluid bearing as described by Moes *et al.* [51] fits well in the numerical procedure. One numerical problem is the high stiffness at large eccentricity.

## 6.2 Suggestions for Further Research

Future work may be directed to the development of a wheel element which allows more complicated tyre force models, like the incorporation of a spin related torque in the contact point. An advanced wheel element with finite thickness is needed for the modelling of the wheel-rail contact as in track-guided vehicles. It would also be useful to develop a three-dimensional version of the belt and pulley pair element and the gear pair element. An improved constitutive model for an elastic belt should be derived which is capable of describing energy conservation.

Because of the uncertainty of the unlubricated bearing properties such as the coefficient of restitution and friction, it is recommended to test the different

models presented in Chapter 5 experimentally, first in a simplified setup to test for the material properties and second in the complete mechanism. Furthermore, it is recommended for practical applications to incorporate the effect of dry friction in the analysis of unlubricated joints in spite of the complexity that this may add to the analysis.

For the analysis and design of controlled systems an interface must be made between the SPACAR software and the control design and simulation software. Jonker and Aarts [33] have shown that such an interface between SPACAR and MATLAB/SIMULINK is quite feasible. This interface then can also be used for the optimization of dynamical systems.

Although the method of superimposition has been described in connection with a specific multibody formalism, it can be used with any formalism that yields linearized equations in a state space form. Finally, procedures for finding the periodic and transient solutions for the small vibrations in the case of a more general gross rigid body motion, for example a motor driven mechanism with given motor characteristic, are interesting and feasible topics for future work.



# Appendix A

## Equations of Motion and Linearization

'I have made a great discovery in mathematics; I have suppressed the summation sign every time that the summation must be made over an index which occurs twice...'

(Albert Einstein, speaking to a friend (1916))

This appendix gives a detailed description of the equations of motion for flexible multibody systems, both holonomic and non-holonomic, according to the finite element method, together with the linearized equations of motion. Opposed to the short-hand matrix-vector notation as used in the main text of this thesis to point out the general structure of the equations, index notation with Einstein summation convention and the so-called iota index selector is used throughout this appendix. This notation eased the implementation of the presented methods in the SPACAR software considerably.

First, the equations of motion for the general holonomic flexible system are derived in terms of independent coordinates. Second, the nominal solution where all elements are assumed to be rigid is obtained. Third, the linearized equations of motion, describing small changes around the nominal solution in terms of small changes in the independent coordinates, are derived; all individual contributions are treated in full detail and finally summarized. This appendix ends with the necessary changes and additions in the case of non-holonomic systems.

## A.1 Equations of Motion

The equations of motion of a flexible holonomic multibody system will be derived with the aid of the principle of virtual power. The inertia properties of elements and nodes will be described by the consistent mass formulation, resulting in position dependent mass matrices and convective force vectors which are quadratic in the velocities.

The principle of virtual power applied to a discrete mechanical system states that the system is in equilibrium when the virtual power of the applied nodal forces  $f_j$  vanishes for all virtual nodal velocities  $\delta\dot{x}_j$  for which all corresponding virtual strain rates  $\delta\dot{\varepsilon}_i$  are zero, as in

$$f_j\delta\dot{x}_j = 0, \quad \forall \quad \{\delta\dot{x}_j | \delta\dot{\varepsilon}_i = 0\}. \quad (\text{A.1})$$

With the index  $j = 1, \dots, n$ , and  $n$  the total number of nodal coordinates, and the index  $i = 1, \dots, m$ , and  $m$  the total number of generalized deformations. The generalized deformations  $\varepsilon_i$ , or generalized strains, can be expressed by the deformation functions  $D_i$  in terms of the nodal coordinates  $x_k$ , as

$$\varepsilon_i = D_i(x_k). \quad (\text{A.2})$$

Differentiation with respect to time yields

$$\dot{\varepsilon}_i = D_{i,j}(x_k)\dot{x}_j. \quad (\text{A.3})$$

The virtual variations of these strain rates  $\dot{\varepsilon}_i$  are given by the same linear velocity expressions

$$\delta\dot{\varepsilon}_i = D_{i,j}(x_k)\delta\dot{x}_j. \quad (\text{A.4})$$

The subsidiary conditions of having zero virtual deformation rates will be incorporated with help of the Lagrangian multipliers  $\sigma_i$ . This results in the virtual power balance

$$f_j\delta\dot{x}_j = \sigma_i\delta\dot{\varepsilon}_i, \quad \wedge \quad \delta\dot{\varepsilon}_i = D_{i,j}\delta\dot{x}_j \quad \forall \quad \delta\dot{x}_j, \quad (\text{A.5})$$

or

$$f_j\delta\dot{x}_j = \sigma_i D_{i,j}\delta\dot{x}_j, \quad \forall \quad \delta\dot{x}_j. \quad (\text{A.6})$$

Since this holds for all virtual velocities  $\delta\dot{x}_j$ , we obtain  $j$  force equilibrium equations:

$$f_j - D_{i,j}\sigma_i = 0. \quad (\text{A.7})$$

The unknown Lagrangian multipliers  $\sigma_i$  can be recognized as the generalized stresses, they are the energetic duals of the generalized strain rates  $\dot{\epsilon}_i$ . For instance in the case of a simple truss element, where  $\epsilon$  is defined as the elongation of the truss, the Lagrangian multiplier  $\sigma$  is identified as the tensile force in the truss. The force equilibrium equations express static force balance. The equations of motion can be found by application of Newton's second law "Mutationem motus proportionalem esse vi motrici impressae, & fieri secundum lineam rectam qua vis illa imprimitur." (*A change in motion is proportional to the motive force impressed and takes place along the straight line in which that force is impressed.*) [56]. In terms of virtual power, the so-called Lagrange's form of d'Alembert's principle, this reads

$$f_j \delta \dot{x}_j = m_{jk} \ddot{x}_k \delta \dot{x}_j, \quad k = 1, \dots, n. \quad (\text{A.8})$$

The matrix,  $m_{jk}$ , represents the lumped nodal mass matrix. In the case of continuous element mass distribution the mass contribution in the virtual power equation gets an integral form, as

$$f_j \delta \dot{x}_j = \int_V \ddot{\mathbf{r}} \cdot \delta \dot{\mathbf{r}} \rho dV. \quad (\text{A.9})$$

In this integral,  $\mathbf{r}$  is the position vector of the infinitesimal particle with mass  $\rho dV$ , and the integral extends over all material elements. For every element type the position of the individual mass particles  $\mathbf{r}$  can always be expressed by the chosen local interpolation functions in terms of the nodal coordinates  $x_j$ . If this procedure is followed we speak of a consistent mass approach. The evaluation of the integral (A.9) results in general in a position dependent mass matrix  $M_{jk}(x_j)$  and additional convective terms  $h_j(x_k, \dot{x}_k)$  being a function of the coordinates and quadratic in the velocities, as in

$$\int_V \ddot{\mathbf{r}} \cdot \delta \dot{\mathbf{r}} \rho dV = (M_{jk}(x_l) \ddot{x}_k + h_j(x_k, \dot{x}_k)) \delta \dot{x}_j. \quad (\text{A.10})$$

An alternative approach [49] is to determine the kinetic energy  $T$  in an element by summing up the contribution of all infinitesimal particles  $\rho dV$  at  $\mathbf{r}$ , and to equate this with the bilinear expression of the kinetic energy in terms of the nodal velocities as in

$$T = \frac{1}{2} \int_V \dot{\mathbf{r}} \cdot \dot{\mathbf{r}} \rho dV = \frac{1}{2} \dot{x}_i M_{ij} \dot{x}_j, \quad (\text{A.11})$$

from which the mass matrix  $M_{ij}$  can be found. The convective inertia terms  $h_i$  are related to this mass matrix as

$$h_i = \left( \frac{\partial M_{ij}}{\partial x_k} - \frac{1}{2} \frac{\partial M_{jk}}{\partial x_i} \right) \dot{x}_j \dot{x}_k. \quad (\text{A.12})$$

This can be seen by considering only the inertia terms in the Lagrange equations as in

$$\frac{d}{dt} \left( \frac{\partial T}{\partial \dot{x}_i} \right) - \frac{\partial T}{\partial x_i} = M_{ij} \ddot{x}_j + h_i. \quad (\text{A.13})$$

This derivation of the convective inertia terms is in most cases more elaborate than the direct approach from (A.10). On the other hand, the kinetic energy approach shows that the position dependent mass matrix is the principal element in the derivation of the inertia forces.

Adding the contribution of the inertia terms to the virtual power, and incorporating the subsidiary conditions  $\delta \varepsilon_i = D_{i,j} \delta \dot{x}_j = 0$  by the Lagrangian multipliers  $\sigma_i$ , leads to the virtual power balance

$$f_j \delta \dot{x}_j - \sigma_i D_{i,j} \delta \dot{x}_j = (M_{jk} \ddot{x}_k + h_j) \delta \dot{x}_j \quad \forall \quad \delta \dot{x}_j. \quad (\text{A.14})$$

From which we derive the equations of motion as

$$M_{jk} \ddot{x}_k = f_j - D_{i,j} \sigma_i - h_j. \quad (\text{A.15})$$

For a system where all elements are considered to be rigid, the unknowns in the equations of motion are the nodal accelerations  $\ddot{x}_k$  and the Lagrangian multipliers  $\sigma_i$ . The known variables are the mass matrix  $M_{jk}$ , the nodal forces  $f_j$ , the first order derivatives of the deformation modes  $D_{i,j}$ , and the additional convective inertia forces  $-h_j$ . To solve the unknowns the algebraic subsidiary condition  $\varepsilon_i = 0$ , which describes the rigidity of the elements, has to be added to the equations of motion. Yet, since the unknowns are the accelerations, we have to differentiate the subsidiary condition from (A.2) twice with respect to time, as in

$$\varepsilon_i = D_i(x) = 0 \rightarrow D_{i,k} \ddot{x}_k + D_{i,jk} \dot{x}_j \dot{x}_k = 0. \quad (\text{A.16})$$

The equations of motion, a set of ordinary differential equations, can now be completed with the subsidiary conditions, a set of algebraic equations, differentiated twice with respect to time. This results in the complete set of differential and algebraic equations, denoted as the set of DAEs

$$\begin{aligned} M_{jk} \ddot{x}_k + D_{i,j} \sigma_i &= f_j - h_j \\ D_{i,k} \ddot{x}_k &= -D_{i,jk} \dot{x}_j \dot{x}_k. \end{aligned} \quad (\text{A.17})$$

This can be presented in a more familiar matrix-vector form as

$$\begin{pmatrix} \mathbf{M} & \mathbf{D}'^T \\ \mathbf{D}' & \mathbf{0} \end{pmatrix} \begin{pmatrix} \ddot{\mathbf{x}} \\ \boldsymbol{\sigma} \end{pmatrix} = \begin{pmatrix} \mathbf{f} - \mathbf{h} \\ -\mathbf{D}''\dot{\mathbf{x}}\dot{\mathbf{x}} \end{pmatrix}, \quad (\text{A.18})$$

where the prime denotes the partial derivatives.

The behaviour of the system in time is found by numerical integration of the nodal velocities and accelerations, the latter being the solution of the equations of motion. The integration is not straightforward. The new coordinates  $x_k + dx_k$  at  $t + dt$  still have to abide the imposed constraints  $D_i(x_k + dx_k) = 0$ . The problem of numerical integration of DAEs can be solved in a number of ways, as pointed out by Gear [17] and treated in depth by Brenan *et al.* [6]. In the SPACAR system the problem of the algebraic subsidiary conditions, the case of deformation modes being zero, is solved by rewriting the system equations in terms of independent coordinates. In literature this is often referred to as coordinate partitioning. The resulting set of ordinary differential equations can then be solved by any type of numerical integration scheme.

For the flexible multibody system we are free to choose the independent coordinates from either the nodal coordinates  $x_k$  or from the generalized deformations  $\varepsilon_i$ . Since the deformations can be looked upon as relative coordinates, they are in favour for describing the small vibrations superimposed on the nominal motion. Therefore, in this appendix, we assume only generalized deformations as being the independent coordinates.

The generalized deformations can be divided into four subsets,

$$\varepsilon = \{\varepsilon^o, \varepsilon^m, \varepsilon^d, \varepsilon^c\}. \quad (\text{A.19})$$

The first,  $\varepsilon^o$ , holds all rigid modes, in other words,  $\varepsilon^o$  is prescribed zero. The second,  $\varepsilon^m$ , describes the input motions, and are usually a function of time. The third,  $\varepsilon^d$ , are the dynamic degrees of freedom, such as flexible modes or generalized independent coordinates. The last,  $\varepsilon^c$ , are the dependent strains, they originate from the redundancy of the structure and are introduced to make the structure statically determinate. The prescribed generalized deformations are  $\{\varepsilon^o, \varepsilon^m\}$ , while the dynamic degrees of freedom  $\varepsilon^d$  are determined through the equations of motion. The state of the system is defined as

$$(\dot{\varepsilon}^d, \varepsilon^d, t). \quad (\text{A.20})$$

The dependent deformations  $\varepsilon^c$  can be calculated as a function of the state or state related variables of the system. In the same manner, the nodal coordinates

are divided into two subsets,

$$x = \{x^o, x^c\}, \quad (\text{A.21})$$

with  $x^o$  for the fixed coordinates and  $x^c$  the free or to be calculated coordinates.

If the constraints imposed by the rigid modes

$$\varepsilon_i = D_i(x_j) = 0, \quad i = \iota(\varepsilon^o), \quad j = \iota(x), \quad (\text{A.22})$$

are consistent, that is, the redundancy of the structure is placed in  $\varepsilon^c$ , the free coordinates can locally be expressed as functions of the prescribed motions and the dynamic degrees of freedom, as in

$$x_j = F_j(\varepsilon_i), \quad j = \iota(x^c), \quad i = \iota(\varepsilon^m, \varepsilon^d). \quad (\text{A.23})$$

These functions  $F_j$  are called the zero order transfer functions.

Here the indices are specified by means of the iota index selector  $\iota(\ )$ . This index selector, as in  $j = \iota(x^c)$ , generates the correct indices  $j$  for the vector  $x_j$  from the subset  $x^c$ . For example:  $\iota(x^c) = 4, 5, 8$  for  $x^c = \{x_4, x_5, x_8\}$ . This notation proved most of its usefulness in the coding stage of the algorithms.

The zero order transfer functions  $F_j$  and their partial derivatives are only implicitly known through the independent generalized deformation functions  $D_i$ . From these we can calculate in every discrete position the velocities according to

$$\dot{\varepsilon}_i = D_{i,j} \dot{x}_j, \quad i = \iota(\varepsilon^o, \varepsilon^m, \varepsilon^d), \quad j = \iota(x^c), \quad (\text{A.24})$$

where  $D_{i,j}$  is a square matrix. Substitution of the velocities from (A.23) given by

$$\dot{x}_j = F_{j,k} \dot{\varepsilon}_k, \quad j = \iota(x^c), \quad k = \iota(\varepsilon^m, \varepsilon^d). \quad (\text{A.25})$$

in (A.24) yields

$$D_{i,j} F_{j,k} = \delta_{ik} \quad (\text{A.26})$$

From these identities the first order transfer function  $F_{j,k}$  can be found as

$$F_{j,k} = (D_{i,j})^{-1} \delta_{ik}, \quad i = \iota(\varepsilon^o, \varepsilon^m, \varepsilon^d), \quad j = \iota(x^c), \quad k = \iota(\varepsilon^m, \varepsilon^d). \quad (\text{A.27})$$

A necessary and sufficient condition for the existence and uniqueness of the solution, which is still a kinematic problem, is determined by the Jacobian  $D_{i,j}$ . If this Jacobian is regular, the inverse exists and the kinematic problem is solvable. This Jacobian is sometimes referred to as the ‘fundamental kinematic

mapping'. The notation  $(D_{i,j})^{-1}$  is somewhat confusing, in the resulting matrix, after the process of inversion, the indices  $i$  and  $j$  are interchanged, as in

$$(D_{i,j})^{-1} = X_{ji}. \quad (\text{A.28})$$

The accelerations are found in the same manner. First we differentiate (A.2) twice, as in

$$\ddot{\varepsilon}_i = D_{i,j}\ddot{x}_j + D_{i,jk}\dot{x}_j\dot{x}_k, \quad i = \iota(\varepsilon), \quad j, k = \iota(x^c). \quad (\text{A.29})$$

With the same implicit substitution as used to determine the nodal velocities, we come up with the expressions for the nodal accelerations in terms of the accelerations of the degrees of freedom and the nodal velocities, as

$$\begin{aligned} \ddot{x}_j &= F_{j,m}\ddot{\varepsilon}_m - (D_{i,j})^{-1}D_{i,kl}\dot{x}_k\dot{x}_l, \\ i &= \iota(\varepsilon^o, \varepsilon^m, \varepsilon^d), \quad j, k, l = \iota(x^c), \quad m = \iota(\varepsilon^m, \varepsilon^d). \end{aligned} \quad (\text{A.30})$$

For convenience, we rewrite the nodal coordinate accelerations  $\ddot{x}^c$  in terms of the accelerations of the dynamic degrees of freedom  $\ddot{\varepsilon}^d$  and the prescribed and convective accelerations, as in

$$\ddot{x}_j = F_{j,i}\ddot{\varepsilon}_i + g_j, \quad i = \iota(\varepsilon^d), \quad j = \iota(x^c), \quad (\text{A.31})$$

with

$$\begin{aligned} g_j &= F_{j,m}\ddot{\varepsilon}_m - (D_{i,j})^{-1}D_{i,kl}\dot{x}_k\dot{x}_l, \\ i &= \iota(\varepsilon^o, \varepsilon^m, \varepsilon^d), \quad j, k, l = \iota(x^c), \quad m = \iota(\varepsilon^m). \end{aligned} \quad (\text{A.32})$$

The dependent strains and their first and second order time derivatives can be calculated by making use of the velocity (A.25) and acceleration expressions (A.31), yielding

$$\begin{aligned} \varepsilon_i &= D_i(F_j(\varepsilon_k)), \\ \dot{\varepsilon}_i &= D_{i,j}F_{j,k}\dot{\varepsilon}_k, \\ \ddot{\varepsilon}_i &= D_{i,j}F_{j,l}\ddot{\varepsilon}_l + D_{i,j}g_j + D_{i,jm}\dot{x}_j\dot{x}_m, \\ i &= \iota(\varepsilon^c), \quad j, m = \iota(x^c), \quad k = \iota(\varepsilon^m, \varepsilon^d), \quad l = \iota(\varepsilon^d). \end{aligned} \quad (\text{A.33})$$

The equations of motion for the dynamic degrees of freedom  $\varepsilon^d$  are found by application of the virtual power principle from (A.14) for all virtual velocities satisfying the first order transfer functions from (A.25), as in

$$\delta\dot{x}_i = F_{i,k}\delta\dot{\varepsilon}_k, \quad i = \iota(x^c), \quad k = \iota(\varepsilon^d). \quad (\text{A.34})$$

Taking arbitrary variations for  $\delta\dot{\varepsilon}_k$  and substitution of the accelerations  $\ddot{x}_j$  according to (A.31) leads to the reduced equation of motion with respect to the dynamic degrees of freedom,

$$(F_{j,l}M_{jk}F_{k,m})\ddot{\varepsilon}_m = -\sigma_l + F_{j,l}(f_j - D_{r,j}\sigma_r - h_j - M_{jk}g_k),$$

$$j, k = \iota(x^c), \quad l, m = \iota(\varepsilon^d), \quad r = \iota(\varepsilon^c). \quad (\text{A.35})$$

Note that in the right-hand side, part of the term  $-F_{j,l}D_{i,j}\sigma_i$  is simplified with the identities from (A.26) to the contribution of the generalized stresses  $-\sigma_l$ , which are dual to the dynamic degrees of freedom  $\varepsilon_m$ , and the contribution of the redundant stresses  $-F_{j,l}D_{r,j}\sigma_r$ . The minus sign is conventional and enters the expressions due to the definition of  $-\sigma_i\delta\dot{\varepsilon}_i$  in (A.5) as the supplied virtual power of the generalized strains to the system. The constraint forces  $\sigma^o$  do not perform any work, and hence drop out of the right-hand of the equation. These equations (A.35) can be compared to (2.7) in the main body of the text. To complete the equations of motion we have to supply a constitutive behaviour for the dynamic degrees of freedom stresses  $\sigma^d$  and the redundant stresses  $\sigma^c$ . If we take, for example, for the dynamic degrees of freedom a linear visco-elastic Kelvin-Voigt material model, then the generalized stresses can be expressed as

$$\sigma_l = S_{lm}\varepsilon_m + S_{lm}^d\dot{\varepsilon}_m, \quad (\text{A.36})$$

with the stiffness matrix  $S_{lm}$ , and the damping matrix  $S_{lm}^d$ . The same behaviour can be used for the redundant stresses, where the indices take the form  $l, m = \iota(\varepsilon^c)$ . On the other hand, any other material model can be chosen, as long as it can be expressed in terms of the state or state dependent variables of the system.

Having solved (A.35) for the accelerations of the dynamic degrees of freedom  $\ddot{\varepsilon}_m$ , the nodal coordinate accelerations follow directly from (A.31). The dependent deformation mode accelerations can be calculated from (A.33). Finally, the constraint forces and the driving forces or rheonomic constraint forces can be derived from (A.15) as

$$\sigma_i = (D_{i,j})^{-1}(f_j - D_{r,j}\sigma_r - h_j - M_{jk}\ddot{x}_k),$$

$$i = \iota(\varepsilon^o, \varepsilon^m, \varepsilon^d), \quad j, k = \iota(x^c), \quad r = \iota(\varepsilon^c). \quad (\text{A.37})$$

Note the use of the transposed inverse of the Jacobian  $D_{i,j}$  opposed to the non-transposed one in the expressions for the first order transfer function (A.27).

## A.2 Nominal Gross Motion

The calculation of the nominal gross motion, the multibody system where all dynamic degrees of freedom set to zero, starts with the equations of motion as in (A.35). We assume that the redundant stresses,  $\sigma_r$ , are known functions of the state. The element forces dual to the fixed dynamic degrees of freedom, which now play the role of constraint forces, result directly from (A.35) with  $\ddot{\varepsilon}_m = 0$ , as

$$\bar{\sigma}_l = F_{j,l}(f_j - D_{r,j}\sigma_r - h_j - M_{jk}g_k). \quad (\text{A.38})$$

Indeed, all constraint forces follow directly from (A.37). These equations (A.38) can be compared to (2.10) in the main body of the text.

Under the assumption of a periodic nominal motion of the system, as in most mechanisms and machines, the calculation of the fundamental state has to be performed in a number of subsequent positions, the discretization of the nominal motion. The transition from one to the next discrete state shall now be discussed. The state of the system is defined by the moment in time  $t$ , from which the kinematic degrees of freedom  $\varepsilon^m$ , which are usually a function of time, can be calculated. Let us assume that at time  $t$  the multibody system is in a state where all constraints are satisfied, meaning that the nodal coordinates  $x_j$  fulfil

$$D_i(x_j) = \delta_{ik}\varepsilon_k, \quad i = \iota(\varepsilon^o, \varepsilon^m), \quad j = \iota(x), \quad k = \iota(\varepsilon^m). \quad (\text{A.39})$$

In this configuration the nodal velocities and accelerations can be calculated according to (A.25) and (A.31), resulting in

$$\dot{x}_j = (D_{i,j})^{-1}\delta_{ik}\dot{\varepsilon}_k, \quad j = \iota(x^c), \quad (\text{A.40})$$

and,

$$\ddot{x}_j = (D_{i,j})^{-1}\delta_{ik}\ddot{\varepsilon}_k - (D_{i,j})^{-1}D_{i,lm}\dot{x}_l\dot{x}_m, \quad l, m = \iota(x^c). \quad (\text{A.41})$$

The constraint forces can be calculated according to (A.37). The nodal coordinates in the subsequent position at  $t + \Delta t$  can be approximated by a Taylor series expansion of  $x_j$  up to the second order, yielding

$$x_j^p(t + \Delta t) = x_j(t) + \dot{x}_j(t)\Delta t + \frac{1}{2}\ddot{x}_j(t)\Delta t^2. \quad (\text{A.42})$$

In general, these predicted coordinates  $x_j^p$  do not fulfil the constraints. With

the help of the following Newton iteration scheme,

$$\begin{aligned}
& \Delta \varepsilon_i = D_i(x_j^p) - \varepsilon_i(t + \Delta t) \\
& \text{while } |\Delta \varepsilon_i| > \text{tolerance} \\
& \quad x_j^p = x_j^p - (D_{i,j}(x_k^p))^{-1} \Delta \varepsilon_i \\
& \quad \Delta \varepsilon_i = D_i(x_j^p) - \varepsilon_i(t + \Delta t) \\
& \text{do} \\
& \quad x_j(t + \Delta t) = x_j^p, \quad i = \iota(\varepsilon^o, \varepsilon^m), \quad j, k = \iota(x^c)
\end{aligned} \tag{A.43}$$

the right coordinates can usually be found within a small number of steps at a given tolerance. If after a maximum number of steps the iteration fails, the system is usually in a near to singular configuration, and the choice of the degrees of freedom have to be reconsidered. The determination of subsequent configurations of the system is found by repetitive analysis, starting from (A.40).

### A.3 Linearized Equations of Motion

In order to describe the behaviour of the small vibrations superimposed on the nominal rigid body motion we have to linearize the reduced equations of motion (A.35) with respect to the dynamic degrees of freedom  $\varepsilon^d$ . The nominal motion is characterized by the undeformed state  $\varepsilon^d = 0$ , and is described in the previous section. We start by adding small changes, denoted by the prefix symbol  $\Delta$ , to all terms in the reduced equation of motion, after which we expand up to the first order of  $\Delta$ , resulting in

$$\begin{aligned}
& (F_{j,l} M_{jk} F_{k,m}) \ddot{\varepsilon}_m + \Delta (F_{j,l} M_{jk} F_{k,m}) \ddot{\varepsilon}_m + (F_{j,l} M_{jk} F_{k,m}) \Delta \ddot{\varepsilon}_m = \\
& \quad - \sigma_l - \Delta \sigma_l + F_{j,l} (f_j - D_{r,j} \sigma_r - h_j - M_{jk} g_k) \\
& \quad \quad + \Delta F_{j,l} (f_j - D_{r,j} \sigma_r - h_j - M_{jk} g_k) \\
& \quad + F_{j,l} (\Delta f_j - \Delta D_{r,j} \sigma_r - D_{r,j} \Delta \sigma_r - \Delta h_j - \Delta M_{jk} g_k - M_{jk} \Delta g_k), \\
& \quad \quad \quad j, k = \iota(x^c), \quad l, m = \iota(\varepsilon^d), \quad r = \iota(\varepsilon^c). \tag{A.44}
\end{aligned}$$

Every single  $\Delta$  term must eventually be expanded into changes in terms of the dynamic degrees of freedom,

$$\Delta \varepsilon_i, \Delta \dot{\varepsilon}_i, \Delta \ddot{\varepsilon}_i, \quad i = \iota(\varepsilon^d),$$

and terms related to the nominal solution, sometimes referred to as the nominal reference state. Each contribution to the linearized equations of motion will be treated separately.

$(F_{j,l}M_{jk}F_{k,m})\ddot{\varepsilon}_m$ : This term is zero since in the nominal reference state  $\ddot{\varepsilon}_m$  is zero.

$\Delta(F_{j,l}M_{jk}F_{k,m})$ : This term does not need to be expanded, with the same reasoning as above.

$\Delta\ddot{\varepsilon}_m$ : No further expansion needed.

$\sigma_l$ : The generalized stresses  $\sigma_l$ , are connected to the generalized strains by the constitutive equations, describing the material behaviour. If we assume a linear visco-elastic Kelvin-Voigt material model as in (A.36) then the stresses  $\sigma_l$  in the nominal reference state will be zero, since in the reference state  $\varepsilon_m$  and  $\dot{\varepsilon}_m$  are zero. These stresses are not to be confused with the the constraint forces from the nominal solution,  $\bar{\sigma}_l$ , as in (A.38) since the boundary conditions have changed.

$\Delta\sigma_l$ : With the same linear visco-elastic Kelvin-Voigt material model as above, small variations of the generalized stresses are described by

$$\Delta\sigma_l = S_{lm}\Delta\varepsilon_m + S_{lm}^d\Delta\dot{\varepsilon}_m, \quad (\text{A.45})$$

with the material stiffness matrix  $S_{lm}$ , and the damping matrix  $S_{lm}^d$ .

$F_{j,l}(f_j - D_{r,j}\sigma_r - h_j - M_{jk}g_k)$ : These are the constraint forces  $\bar{\sigma}_l$  from the nominal reference state as in (A.38).

$\Delta F_{j,l}$ : Using the identities  $D_{i,j}F_{j,l} = \delta_{il}$  as in (A.26), and taking the first variation

$$\Delta D_{i,j}F_{j,l} + D_{i,j}\Delta F_{j,l} = 0, \quad (\text{A.46})$$

leads to

$$\Delta F_{j,l} = -(D_{i,j})^{-1}\Delta D_{i,k}F_{k,l}. \quad (\text{A.47})$$

Substitution of the variation of the Jacobian as

$$\Delta D_{i,k} = D_{i,km}\Delta x_m, \quad (\text{A.48})$$

and the variation of the nodal coordinates from (A.25) as

$$\Delta x_m = F_{m,n}\Delta\varepsilon_n, \quad (\text{A.49})$$

leads finally to

$$\begin{aligned} \Delta F_{j,l} &= -(D_{i,j})^{-1}D_{i,km}F_{k,l}F_{m,n}\Delta\varepsilon_n, \\ i &= \iota(\varepsilon^o, \varepsilon^m, \varepsilon^d), \quad j, k, m = \iota(x^c), \quad l, n = \iota(\varepsilon^d). \end{aligned} \quad (\text{A.50})$$

$\Delta f_j$ : Under the assumption of dead loads, the externally applied nodal forces do not vary, and  $\Delta f_j = 0$ .

$\Delta \sigma_r$ : If we assume a linear visco-elastic Kelvin-Voigt material model for the redundant stresses, then small variations result in

$$\Delta \sigma_r = S_{rs} \Delta \varepsilon_s + S_{rs}^d \Delta \dot{\varepsilon}_s, \quad r, s = \iota(\varepsilon^c), \quad (\text{A.51})$$

with the material stiffness matrix  $S_{rs}$  and the damping matrix  $S_{rs}^d$ . The variations of the dependent strains are

$$\Delta \varepsilon_s = D_{s,j} F_{j,m} \Delta \varepsilon_m, \quad j = \iota(x^c), \quad m = \iota(\varepsilon^d), \quad (\text{A.52})$$

and the variations of the dependent strain rates are

$$\Delta \dot{\varepsilon}_s = D_{s,j} F_{j,m} \Delta \dot{\varepsilon}_m + D_{s,pq} \dot{x}_p F_{q,m} \Delta \varepsilon_m - D_{s,j} (D_{i,j})^{-1} D_{i,pq} \dot{x}_p F_{q,m} \Delta \varepsilon_m, \quad p, q = \iota(x^c). \quad (\text{A.53})$$

$\Delta h_j$ : The convective inertia terms  $h_j$  are in general a function of the coordinates and quadratic in the velocities. The variation takes the form,

$$\Delta h_j = \frac{\partial h_j}{\partial x_k} \Delta x_k + \frac{\partial h_j}{\partial \dot{x}_k} \Delta \dot{x}_k. \quad (\text{A.54})$$

The variation of the nodal velocities  $\Delta \dot{x}_k$  can be calculated from (A.24) as

$$\begin{aligned} \Delta D_{i,k} \dot{x}_k + D_{i,k} \Delta \dot{x}_k &= \delta_{il} \Delta \dot{\varepsilon}_l \rightarrow \\ \Delta \dot{x}_k &= -(D_{i,k})^{-1} \Delta D_{i,m} \dot{x}_m + (D_{i,k})^{-1} \delta_{il} \Delta \dot{\varepsilon}_l. \end{aligned} \quad (\text{A.55})$$

The variation of the nodal velocities is in two parts, the first due to changes in geometry and the second due to changes in the deformation rates. Substitution of (A.48) and (A.49) leads to,

$$\Delta \dot{x}_k = -(D_{i,k})^{-1} D_{i,mj} \dot{x}_m F_{j,n} \Delta \varepsilon_n + F_{k,l} \Delta \dot{\varepsilon}_l. \quad (\text{A.56})$$

Substitution of this result in the expression for  $\Delta h_j$  leads to,

$$\Delta h_j = \left( \frac{\partial h_j}{\partial x_k} F_{k,n} - \frac{\partial h_j}{\partial \dot{x}_k} (D_{i,k})^{-1} D_{i,mj} \dot{x}_m F_{j,n} \right) \Delta \varepsilon_n + \left( \frac{\partial h_j}{\partial \dot{x}_k} F_{k,n} \right) \Delta \dot{\varepsilon}_n. \quad (\text{A.57})$$

$\Delta M_{jk}$ : The consistent mass formulation according to element mass integral (A.10) leads, in general, to a position dependent mass matrix. The variations take the form,

$$\Delta M_{jk} = M_{jk,l} \Delta x_l. \quad (\text{A.58})$$

Substitution of the coordinate variations (A.49) results in,

$$\Delta M_{jk} = M_{jk,l} F_{l,m} \Delta \varepsilon_m. \quad (\text{A.59})$$

$\Delta g_k$ : The variations of the convective and prescribed accelerations is an elaborate task. We will start with the expression from (A.32) in the implicit form, reading

$$D_{i,j} g_j = -D_{i,kl} \dot{x}_k \dot{x}_l + \delta_{im} \ddot{\varepsilon}_m. \quad (\text{A.60})$$

Taking the first variation leads to,

$$\begin{aligned} \Delta D_{i,j} g_j + D_{i,j} \Delta g_j &= -\Delta D_{i,kl} \dot{x}_k \dot{x}_l \\ &\quad - D_{i,kl} \Delta \dot{x}_k \dot{x}_l \\ &\quad - D_{i,kl} \dot{x}_k \Delta \dot{x}_l \\ &\quad + \delta_{im} \Delta \ddot{\varepsilon}_m. \end{aligned} \quad (\text{A.61})$$

The first term on the right-hand side is a new and interesting one, it holds the third order variation of the deformation modes. They expand into,

$$\begin{aligned} \Delta D_{i,kl} \dot{x}_k \dot{x}_l &= D_{i,klm} \Delta x_m \dot{x}_k \dot{x}_l \\ &= D_{i,klm} \dot{x}_k \dot{x}_l F_{m,n} \Delta \varepsilon_n. \end{aligned} \quad (\text{A.62})$$

The second and the third term in (A.61) are the same if all constraints are holonomic since in that case the second order derivatives are symmetric,  $D_{i,kl} = D_{i,lk}$ . Expansion of the third term leads to,

$$D_{i,kl} \dot{x}_k \Delta \dot{x}_l = D_{i,kl} \dot{x}_k [-(D_{p,l})^{-1} D_{p,rs} \dot{x}_r F_{s,n}] \Delta \varepsilon_n + D_{i,kl} \dot{x}_k F_{l,n} \Delta \dot{\varepsilon}_n. \quad (\text{A.63})$$

The last term, the variation of the prescribed degrees of freedom,  $\Delta \dot{\varepsilon}_m$ ,  $m = \iota(\varepsilon^m)$  is zero. Adding up all terms yields,

$$\begin{aligned} \Delta g_j &= -(D_{i,j})^{-1} [\{D_{i,mk} g_m F_{k,n} \\ &\quad + D_{i,klm} \dot{x}_k \dot{x}_l F_{m,n} \\ &\quad - 2D_{i,kl} \dot{x}_k ((D_{p,l})^{-1} D_{p,rs} \dot{x}_r F_{s,n})\} \Delta \varepsilon_n \\ &\quad + 2D_{i,kl} \dot{x}_k F_{l,n} \Delta \dot{\varepsilon}_n]. \end{aligned} \quad (\text{A.64})$$

Assembly of all contributions to the linearized equation of motion and re-ordering them with respect to the variations  $\Delta\ddot{\varepsilon}_m$ ,  $\Delta\dot{\varepsilon}_m$ , and  $\Delta\varepsilon_m$  yields

$$M_{lm}\Delta\ddot{\varepsilon}_m + C_{lm}\Delta\dot{\varepsilon}_m + K_{lm}\Delta\varepsilon_m = \bar{\sigma}_l, \quad l, m = \iota(\varepsilon^d). \quad (\text{A.65})$$

The forcings at the right-hand side,  $\bar{\sigma}_l$ , are the constraint forces (A.38) from the nominal reference state. These equations (A.65) can be compared to (2.11) in the main body of the text. Every matrix in itself is a sum of terms having a clear origin. These origins will be explained and denoted by a superscript symbol. If a matrix is symmetric this will be indicated by the abbreviation ‘sym.’ at the end of a formula.

The first matrix,  $M_{lm}$ , is the mass matrix for which we have only one term,

$$M_{lm} = M_{lm}^r, \quad (\text{A.66})$$

with the reduced mass matrix  $M_{lm}^r$  from the general equation of motion (A.35) as

$$M_{lm}^r = F_{j,l}M_{jk}F_{k,m}, \quad j, k = \iota(x^c), \quad \text{sym.} \quad (\text{A.67})$$

The second matrix,  $C_{lm}$ , holds all the velocity sensitive terms like for instance damping and gyroscopic terms. This matrix is the sum of three contributions,

$$C_{lm} = C_{lm}^d + C_{lm}^g + C_{lm}^h. \quad (\text{A.68})$$

The first term,  $C_{lm}^d$ , is the damping due to the visco-elastic material behaviour of the degrees of freedom and of the redundant strains,

$$C_{lm}^d = S_{lm}^d + F_{j,l}D_{r,j}S_{rs}^dD_{s,p}F_{p,m}, \quad \text{sym.} \quad (\text{A.69})$$

The second term  $C_{lm}^g$  finds its origin in the quadratic velocity dependent contributions to  $g$  from (A.32),

$$\begin{aligned} C_{lm}^g &= F_{j,l}M_{jk}\Delta g_k \\ &= -2F_{j,l}M_{jk}(D_{i,k})^{-1}D_{i,pq}F_{p,m}\dot{x}_q. \end{aligned} \quad (\text{A.70})$$

The third term  $C_{lm}^h$  comes from the convective inertia terms  $h_j$ ,

$$C_{lm}^h = F_{j,l}\frac{\partial h_j}{\partial \dot{x}_k}F_{k,m}. \quad (\text{A.71})$$

The third matrix in the linearized equations of motion (A.65) is the stiffness matrix  $K_{lm}$ , holding terms like material and geometric stiffness. In general, six contributions can be distinguished,

$$K_{lm} = K_{lm}^s + K_{lm}^f + K_{lm}^d + K_{lm}^h + K_{lm}^m + K_{lm}^g. \quad (\text{A.72})$$

The first term  $K_{lm}^s$  originates from the material stiffness, the stiffness due to the constitutive material behaviour, of the degree of freedom stresses and the redundant stresses,

$$K_{lm}^s = S_{lm} + F_{j,l} D_{r,j} S_{rs} D_{s,p} F_{p,m}, \quad \text{sym.} \quad (\text{A.73})$$

The second term  $K_{lm}^f$  is the geometric stiffness matrix, having its origin in  $D_{i,jk} \sigma_i$ , and is well known from the finite element method. At first sight the term,

$$\begin{aligned} K_{lm}^f &= -\Delta F_{j,l} (f_j - D_{r,j} \sigma_r - h_j - M_{jk} g_k) \\ &= (D_{i,j})^{-1} D_{i,pq} F_{p,l} F_{q,m} (f_j - D_{r,j} \sigma_r - h_j - M_{jk} g_k), \end{aligned} \quad (\text{A.74})$$

looks more complicated but after substitution of the constraint forces (A.38) as calculated in the nominal reference state and repeated here as

$$\bar{\sigma}_i = (D_{i,j})^{-1} (f_j - D_{r,j} \sigma_r - h_j - M_{jk} g_k),$$

this contribution gets the well known form,

$$K_{lm}^f = \sigma_i D_{i,pq} F_{p,l} F_{q,m}, \quad \text{sym.} \quad (\text{A.75})$$

Note the extra transformations  $F_{p,l}, F_{q,m}$  which is necessary to transform from coordinate variations  $\Delta x_q$  to degree of freedom variations  $\Delta \varepsilon_m$ . The third term,  $K_{lm}^d$ , is the stiffness due to the geometry change caused by the velocity dependent part of the redundant stresses. This contribution will be split into two parts as

$$K_{lm}^d = K_{lm}^{d1} + K_{lm}^{d2}, \quad (\text{A.76})$$

with

$$K_{lm}^{d1} = F_{j,l} D_{r,j} S_{rs}^d D_{s,pq} \dot{x}_p F_{q,m}, \quad (\text{A.77})$$

and

$$K_{lm}^{d2} = -F_{j,l} D_{r,j} S_{rs}^d D_{s,k} (D_{i,k})^{-1} D_{i,pq} \dot{x}_p F_{q,m}. \quad (\text{A.78})$$

The fourth term,  $K_{lm}^h$ , is the stiffness due to the change of the convective inertia terms  $h_j$ , and originates from

$$K_{lm}^h = F_{j,l} \Delta h_j = F_{j,l} \left( \frac{\partial h_j}{\partial x_k} F_{k,m} - \frac{\partial h_j}{\partial \dot{x}_k} (D_{i,k})^{-1} D_{i,pq} \dot{x}_p F_{q,m} \right). \quad (\text{A.79})$$

In these expressions we can distinguish two parts, the first part due to changes in the coordinates and the second part due to changes in the velocities, as

$$K_{lm}^h = K_{lm}^{h1} + K_{lm}^{h2}, \quad (\text{A.80})$$

with

$$K_{lm}^{h1} = F_{j,l} \frac{\partial h_j}{\partial x_k} F_{k,m}, \quad (\text{A.81})$$

and

$$K_{lm}^{h2} = -F_{j,l} \frac{\partial h_j}{\partial \dot{x}_k} (D_{i,k})^{-1} D_{i,pq} \dot{x}_p F_{q,m}. \quad (\text{A.82})$$

The fifth term,  $K_{lm}^m$ , is the stiffness due to the change of the consistent mass matrix,

$$K_{lm}^m = F_{j,l} \Delta M_{jk} g_k = F_{j,l} M_{jk,p} F_{p,m} g_k. \quad (\text{A.83})$$

The sixth and last term,  $K_{lm}^g$  is the stiffness due to the changes in the convective acceleration terms  $g$ ,

$$K_{lm}^g = F_{j,l} M_{jk} \Delta g_k. \quad (\text{A.84})$$

This contribution is the most complex one and shall be split into three parts

$$K_{lm}^g = K_{lm}^{g1} + K_{lm}^{g2} + K_{lm}^{g3}. \quad (\text{A.85})$$

The first part  $K_{lm}^{g1}$ , is due to the change in the first order geometry,  $\Delta D_{i,p}$ , and reads

$$K_{lm}^{g1} = -F_{j,l} M_{jk} (D_{i,k})^{-1} D_{i,pq} g_p F_{q,m}. \quad (\text{A.86})$$

The second part  $K_{lm}^{g2}$ , finds its origin in the velocity changes  $\Delta \dot{x}_p$ , and reads

$$K_{lm}^{g2} = 2F_{j,l} M_{jk} (D_{i,k})^{-1} D_{i,pq} \dot{x}_p [(D_{t,q})^{-1} D_{t,uv} \dot{x}_u F_{v,m}]. \quad (\text{A.87})$$

The third and last contribution,  $K_{lm}^{g3}$ , originates from the third order partial derivatives of the generalized deformation functions,  $D_{i,pqt}$ , and yields

$$K_{lm}^{g3} = -F_{j,l} M_{jk} (D_{i,k})^{-1} D_{i,pqt} \dot{x}_p \dot{x}_q F_{t,m}. \quad (\text{A.88})$$

The contributions to the mass matrix  $M_{lm}$ , the velocity sensitivity matrix  $C_{lm}$ , and the stiffness matrix  $K_{lm}$  of the linearized equations of motion (A.65),

are summarized as

$$\begin{aligned}
M_{lm}^r &= F_{j,l} M_{jk} F_{k,m} && \text{sym.} \\
C_{lm}^d &= S_{lm}^d + F_{j,l} D_{r,j} S_{rs}^d D_{s,p} F_{p,m} && \text{sym.} \\
C_{lm}^g &= -2F_{j,l} M_{jk} (D_{i,k})^{-1} D_{i,pq} F_{p,m} \dot{x}_q \\
C_{lm}^h &= F_{j,l} \frac{\partial h_j}{\partial \dot{x}_k} F_{k,m} \\
K_{lm}^s &= S_{lm} + F_{j,l} D_{r,j} S_{rs} D_{s,p} F_{p,m} && \text{sym.} \\
K_{lm}^f &= \sigma_i D_{i,pq} F_{p,l} F_{q,m} && \text{sym.} \\
K_{lm}^{d1} &= F_{j,l} D_{r,j} S_{rs}^d D_{s,pq} \dot{x}_p F_{q,m} \\
K_{lm}^{d2} &= -F_{j,l} D_{r,j} S_{rs}^d D_{s,k} (D_{i,k})^{-1} D_{i,pq} \dot{x}_p F_{q,m} \\
K_{lm}^{h1} &= F_{j,l} \frac{\partial h_j}{\partial \dot{x}_k} F_{k,m} \\
K_{lm}^{h2} &= -F_{j,l} \frac{\partial h_j}{\partial \dot{x}_k} (D_{i,k})^{-1} D_{i,pq} \dot{x}_p F_{q,m} \\
K_{lm}^m &= F_{j,l} M_{jk,p} F_{p,m} g_k \\
K_{lm}^{g1} &= -F_{j,l} M_{jk} (D_{i,k})^{-1} D_{i,pq} g_p F_{q,m} \\
K_{lm}^{g2} &= 2F_{j,l} M_{jk} (D_{i,k})^{-1} D_{i,pq} \dot{x}_p [(D_{t,q})^{-1} D_{t,uv} \dot{x}_u F_{v,m}] \\
K_{lm}^{g3} &= -F_{j,l} M_{jk} (D_{i,k})^{-1} D_{i,pqt} \dot{x}_p \dot{x}_q F_{t,m}
\end{aligned}$$

## A.4 Extensions to Non-Holonomic Systems

In addition to the holonomic constraints (A.22) we assume that there are non-holonomic constraints, or non-integrable velocity constraints, present in the system. Furthermore we assume that these non-holonomic constraints originate from idealized rolling contact or perfect knife edge contact. Such a constraint can then be expressed in terms of some zero relative velocity or zero slip function between the two bodies in the contact area, and is therefore linear in the velocities. For instance, if element  $e$  has non-slipping components, it has to satisfy the constraints

$$s_i^e = V_{ij}^e(x_k)^e \dot{x}_j^e = 0. \quad (\text{A.89})$$

Assembly of all slip functions for the system results in

$$s_i = V_{ij}(x_k) \dot{x}_j, \quad i = \iota(s), \quad j, k = \iota(x). \quad (\text{A.90})$$

The slips  $s_i$  can be interpreted as non-integrable generalized strain rates  $\dot{\varepsilon}_i$  (A.3). To make the connection with such strain rates we rewrite the slip functions in

terms of partial quasi-derivatives  $D_{i,j}$  as in

$$s_i = D_{i,j}(x_k)\dot{x}_j, \quad i = \iota(s), \quad j, k = \iota(x). \quad (\text{A.91})$$

The integral of these strain rates have no physical meaning, therefore the prefix ‘quasi’. The slips and the strain rates are physically the same and to unify the finite element approach, we will use from now on the partial quasi-derivatives defined by

$$D_{i,j} = V_{ij}, \quad i = \iota(s), \quad j = \iota(x). \quad (\text{A.92})$$

All element slips can be assembled in a slip space  $s$  which, by the boundary conditions, is divided into two parts

$$s = \{s^o, s^c\}, \quad (\text{A.93})$$

with  $s^o$  the zero prescribed slips and  $s^c$  the free or to be calculated slips. Accordingly the non-holonomic constraints imposed on the system are

$$D_{i,j}(x_k)\dot{x}_j = 0, \quad i = \iota(s^o), \quad j = \iota(x^c), \quad k = \iota(x). \quad (\text{A.94})$$

The remaining free slips can be used to impose forces on the system via a constitutive behaviour. For instance with a rolling tyre model, the vertical aligning torque or spin torque which originates from the finite contact area.

For holonomic systems the number of generalized independent coordinates describing the configuration are the same as the number of generalized independent velocities. This is not the case for non-holonomic systems. The non-holonomic constraints reduce the number of independent velocities by the number of these constraints to the number of degrees of freedom. For the degrees of freedom we will be using the dynamic degrees of freedom  $\varepsilon^d$  from the previous section. For the additional generalized coordinates we introduce the generalized kinematic coordinates expressed by the generalized kinematic deformations  $\varepsilon^k$ , defined by

$$\varepsilon_i = D_i(x_j), \quad i = \iota(\varepsilon^k), \quad j = \iota(x). \quad (\text{A.95})$$

Again we make use of generalized deformations instead of generalized coordinates since the first can be looked upon as relative coordinates and have therefore a wider field of application. The state of the system is now defined by

$$(\dot{\varepsilon}^d, \varepsilon^d, \varepsilon^k, t) \quad (\text{A.96})$$

Compare this with the state of a holonomic constraint system (A.20).

### A.4.1 State Equations

The dynamics of the system is described by the time derivatives of the state or the state equations. The first set,  $d\dot{\varepsilon}^d/dt$ , are the equations of motion for the dynamic degrees of freedom. The second part,  $d\varepsilon^d/dt$ , is apparently the first part of the state self. The last set,  $d\varepsilon^k/dt$ , are the non-holonomic constraints expressed as the time derivatives of the kinematic coordinates in terms of the state variables. We will start with the derivation of the equations of motion.

The configuration of the system can be described by means of a zero order transfer function  $F$  as in

$$x_j = F_j(\varepsilon_i), \quad j = \iota(x^c), \quad i = \iota(\varepsilon^m, \varepsilon^d, \varepsilon^k). \quad (\text{A.97})$$

The prescribed motions, or rheonomic constraints, are represented by the generalized deformations  $\varepsilon^m$ , which are explicit functions of time. The zero order transfer function is implicitly known through the holonomic constraints (A.22) and can be determined by a Newton iteration scheme as in (A.43) but with different indices. Starting from a predicted nearby configuration at time  $t + \Delta t$  with coordinates  $x_j^p$ , which in general do not fulfil the constraints, the iteration scheme reads

$$\begin{aligned} \Delta\varepsilon_i &= D_i(x_j^p) - \varepsilon_i(t + \Delta t) \\ \text{while } |\Delta\varepsilon_i| &> \text{tolerance} \\ x_j^p &= x_j^p - (D_{i,j}(x_k^p))^{-1} \Delta\varepsilon_i \\ \Delta\varepsilon_i &= D_i(x_j^p) - \varepsilon_i(t + \Delta t) \\ \text{do} \\ x_j(t + \Delta t) &= x_j^p, \quad i = \iota(\varepsilon^o, \varepsilon^m, \varepsilon^d, \varepsilon^k), \quad j, k = \iota(x^c) \end{aligned} \quad (\text{A.98})$$

If the Jacobian  $D_{i,j}$  is regular, the correct coordinates which fulfil all holonomic constraints at time  $t + \Delta t$ , can usually be found within a small number of steps at a given tolerance. If after a maximum number of steps the iteration fails, the system is usually in a near to singular configuration, and the choice of the degrees of freedom has to be reconsidered.

The velocities of the system can be described by means of a first order transfer function  $H_{jk}$  as in

$$\dot{x}_j = H_{jk} \dot{\varepsilon}_k, \quad j = \iota(x^c), \quad k = \iota(\varepsilon^m, \varepsilon^d). \quad (\text{A.99})$$

This first order transfer function, which is not a partial derivative of the zero order transfer function, can be found in the following manner. The partial derivatives of the generalized deformation functions and the partial quasi-derivatives

originating from the non-holonomic constraints are combined into

$$\dot{\varepsilon}_i = D_{i,j} \dot{x}_j, \quad i = \iota(\varepsilon^o, \varepsilon^m, \varepsilon^d, s^o), \quad j = \iota(x^c), \quad (\text{A.100})$$

where  $D_{i,j}$  is a square matrix. Substitution of the velocities from (A.99) in (A.100) leads to the identities

$$D_{i,j} H_{jk} = \delta_{ik}, \quad (\text{A.101})$$

from which the first order transfer function  $H_{jk}$  can be found as

$$H_{jk} = (D_{i,j})^{-1} \delta_{ik}, \quad i = \iota(\varepsilon^o, \varepsilon^m, \varepsilon^d, s^o), \quad j = \iota(x^c), \quad k = \iota(\varepsilon^m, \varepsilon^d). \quad (\text{A.102})$$

Note that the Jacobian  $D_{i,j}$  used here, which must be regular, is not the same as the one used in the zero order iteration scheme (A.98). The difference lies within the  $i$  index,  $\varepsilon^k$  for the zero order iteration scheme and  $s^o$  for the first order transfer function.

The nodal accelerations can be found in the same manner. We first differentiate the strain rates and slips from (A.100) with respect to time and with the same implicit substitution come up for the nodal accelerations in terms of the independent state variables as

$$\ddot{x}_j = H_{jm} \ddot{\varepsilon}_m + g_j, \quad j = \iota(x^c), \quad m = \iota(\varepsilon^d), \quad (\text{A.103})$$

with the convective and prescribed accelerations  $g_j$  given by

$$g_j = H_{jn} \ddot{\varepsilon}_n - (D_{i,j})^{-1} D_{i,kl} \dot{x}_k \dot{x}_l, \\ i = \iota(\varepsilon^o, \varepsilon^m, \varepsilon^d, s^o), \quad j, k, l = \iota(x^c), \quad n = \iota(\varepsilon^m). \quad (\text{A.104})$$

Note that the second order derivatives  $D_{i,kl}$  for  $i = \iota(s^o)$  are not symmetric in  $k$  and  $l$  since they originate from the quasi partial derivatives (A.92). The dependent strains and their first and second order time derivatives can be expressed in terms of the independent state variables as

$$\varepsilon_i = D_i(F_j(\varepsilon_k)), \\ \dot{\varepsilon}_i = D_{i,j} \dot{H}_{jl} \dot{\varepsilon}_l, \\ \ddot{\varepsilon}_i = D_{i,j} \dot{H}_{jm} \ddot{\varepsilon}_m + D_{i,j} g_j + D_{i,jn} \dot{x}_j \dot{x}_n, \\ i = \iota(\varepsilon^c), \quad j, n = \iota(x^c), \quad k = \iota(\varepsilon^m, \varepsilon^d, \varepsilon^k), \quad l = \iota(\varepsilon^m, \varepsilon^d), \quad m = \iota(\varepsilon^d). \quad (\text{A.105})$$

The equations of motion for the degrees of freedom  $\varepsilon^d$  are found by application of the virtual power principle from (A.14) for all virtual velocities satisfying the first order transfer functions (A.99), as in

$$\delta \dot{x}_i = H_{ik} \delta \dot{\varepsilon}_k, \quad i = \iota(x^c), \quad k = \iota(\varepsilon^d). \quad (\text{A.106})$$

Taking arbitrary variations for  $\delta \dot{\varepsilon}_k$  and substitution of the accelerations  $\ddot{x}_j$  according to (A.103) in (A.14) leads to the reduced equation of motion with respect to the dynamic degrees of freedom as

$$(H_{jl} M_{jk} H_{km}) \ddot{\varepsilon}_m = -\sigma_l + H_{jl} (f_j - D_{r,j} \sigma_r - h_j - M_{jk} g_k), \\ j, k = \iota(x^c), \quad l, m = \iota(\varepsilon^d), \quad r = \iota(\varepsilon^c). \quad (\text{A.107})$$

The main difference with the holonomic case (A.35) is the presence of the first order transfer function  $H_{jl}$  instead of  $F_{j,l}$ . Where  $F_{j,l}$  stands for partial derivatives, this is not the case with  $H_{jl}$ , due to the non-holonomic constraints. These equations (A.107) can be compared to (2.31) in the main body of the text.

Having solved (A.107) for the accelerations of the dynamic degrees of freedom  $\ddot{\varepsilon}_m$ , the nodal coordinate accelerations follow directly from (A.103). The dependent deformation mode accelerations can be calculated from (A.105). Finally, the constraint forces, holonomic, non-holonomic and rheonomic, can be derived from (A.15) as

$$\sigma_i = (D_{i,j})^{-1} (f_j - D_{r,j} \sigma_r - h_j - M_{jk} \ddot{x}_k), \\ i = \iota(\varepsilon^o, \varepsilon^m, \varepsilon^d, s^o), \quad j, k = \iota(x^c), \quad r = \iota(\varepsilon^c). \quad (\text{A.108})$$

Note the use of the transposed inverse of the Jacobian  $D_{i,j}$  opposed to the non-transposed one in the expressions for the first order transfer function (A.102).

The last set of state equations are the time derivatives of the kinematic coordinates,  $\dot{\varepsilon}^k$ , in terms of the state variables, which are the non-holonomic constraints in an explicit form. They can be found by substitution of the nodal velocities expressed in terms of the velocities of the independent degrees of freedom and the prescribed motion (A.99) in the time derivatives of the kinematic coordinates (A.95) yielding

$$\dot{\varepsilon}_p = D_{p,j} H_{jq} \dot{\varepsilon}_q, \quad p = \iota(\varepsilon^k), \quad j = \iota(x^c), \quad q = \iota(\varepsilon^m, \varepsilon^d). \quad (\text{A.109})$$

We summarize the state equations with the results from (A.107) and (A.109) as

$$\frac{d}{dt} \begin{bmatrix} \dot{\varepsilon}_l^d \\ \varepsilon_l^d \\ \varepsilon_p^k \end{bmatrix} = \begin{bmatrix} (H_{jl}M_{jk}H_{km})^{-1}\{-\sigma_l + H_{jl}(f_j - D_{r,j}\sigma_r - h_j - M_{jk}g_k)\} \\ \dot{\varepsilon}_l^d \\ D_{p,j}H_{jq}\dot{\varepsilon}_q \end{bmatrix} \quad (\text{A.110})$$

These equations can be compared to (2.36) in the main body of the text.

#### A.4.2 Linearized State Equations

In order to describe the behaviour of the small vibrations or small motions superimposed on a nominal motion we have to linearize the state equations (A.110) with respect to the state variables  $(\dot{\varepsilon}^d, \varepsilon^d, \varepsilon^k)$ . The nominal motion is characterized by the undeformed state  $\varepsilon^d = 0$  and  $\varepsilon^k = 0$ , and can be determined from the equations as presented in the previous section. We start by adding small changes, denoted by the prefix symbol  $\Delta$ , to all terms in the reduced equation of motion, after which we expand up to the first order of  $\Delta$ , resulting in

$$\begin{aligned} (H_{jl}M_{jk}H_{km})\ddot{\varepsilon}_m + \Delta(H_{jl}M_{jk}H_{km})\ddot{\varepsilon}_m + (H_{jl}M_{jk}H_{km})\Delta\ddot{\varepsilon}_m = \\ -\sigma_l - \Delta\sigma_l + H_{jl}(f_j - D_{r,j}\sigma_r - h_j - M_{jk}g_k) \\ + \Delta H_{jl}(f_j - D_{r,j}\sigma_r - h_j - M_{jk}g_k) \\ + H_{jl}(\Delta f_j - \Delta D_{r,j}\sigma_r - D_{r,j}\Delta\sigma_r - \Delta h_j - \Delta M_{jk}g_k - M_{jk}\Delta g_k), \\ j, k = \iota(x^c), l, m = \iota(\varepsilon^d), r = \iota(\varepsilon^c). \end{aligned} \quad (\text{A.111})$$

Every single  $\Delta$  term must be expanded into small variations of the state variables

$$\Delta\dot{\varepsilon}^d, \Delta\varepsilon^d, \Delta\varepsilon^k,$$

and terms related to the nominal solution. Assembly of all the contributions and reordering them with respect to these variations leads to the linearized equations of motion as

$$M_{lm}\Delta\ddot{\varepsilon}_m + C_{lm}\Delta\dot{\varepsilon}_m + K_{ln}\Delta\varepsilon_n = \bar{\sigma}_l, \quad l, m = \iota(\varepsilon^d), n = \iota(\varepsilon^d, \varepsilon^k). \quad (\text{A.112})$$

The forcing on the right-hand side are the constraint forces (A.108) which arise from the nominal rigid body solution. These equations (A.112) can be compared to (2.37) in the main body of the text. The contributions to the mass matrix  $M_{lm}$ , the velocity sensitivity matrix  $C_{lm}$ , and the stiffness matrix  $K_{ln}$ , note that

this is now a non-square matrix due to the additional kinematic coordinates, are closely related to those from the holonomic case.

There are two general rules to derive the non-holonomic contributions from the holonomic ones. First, replace all occurrences of  $F_{i,j}$  by  $H_{ij}$ , except for the second index related derivatives in the stiffness matrices. These are the real partial derivatives of the zero order transfer function  $F$ , and can be determined from the holonomic constraints (A.22), and the deformation functions for the prescribed motions  $\varepsilon^m$ , the degrees of freedom  $\varepsilon^d$ , and the additional kinematic coordinates  $\varepsilon^k$ , as in

$$F_{m,n} = (D_{k,m})^{-1} \delta_{kn}, \quad k = \iota(\varepsilon^o, \varepsilon^m, \varepsilon^d, \varepsilon^k), \quad m = \iota(x^c), \quad n = \iota(\varepsilon^d, \varepsilon^k). \quad (\text{A.113})$$

Second, replace all occurrences of  $2D_{i,jk}$  by  $D_{i,jk} + D_{i,kj}$ , since some of these are quasi second order derivatives which are non-symmetric in  $j$  and  $k$ . Application of these rules yields the mass matrix as

$$M_{lm} = H_{jl} M_{jk} H_{km}, \quad \text{sym.}, \quad (\text{A.114})$$

the velocity sensitivity matrix  $C_{lm}$  as the sum of the three contributions

$$\begin{aligned} C_{lm}^d &= S_{lm}^d + H_{jl} D_{r,j} S_{rs}^d D_{s,p} H_{pm}, \quad \text{sym.} \\ C_{lm}^g &= -H_{jl} M_{jk} (D_{i,k})^{-1} \{D_{i,pq} + D_{i,qp}\} H_{pm} \dot{x}_q \\ C_{lm}^h &= H_{jl} \frac{\partial h_j}{\partial \dot{x}_k} H_{km}, \end{aligned} \quad (\text{A.115})$$

and the stiffness matrix  $K_{lm}$  as the sum of the ten terms

$$\begin{aligned} K_{ln}^s &= S_{lm} \delta_{mn} + H_{jl} D_{r,j} S_{rs}^d D_{s,p} F_{p,n} \\ K_{ln}^f &= \sigma_i D_{i,pq} H_{pl} F_{q,n} \\ K_{ln}^{d1} &= H_{jl} D_{r,j} S_{rs}^d D_{s,pq} \dot{x}_p F_{q,n} \\ K_{ln}^{d2} &= -H_{jl} D_{r,j} S_{rs}^d D_{s,k} (D_{i,k})^{-1} D_{i,pq} \dot{x}_p F_{q,n} \\ K_{ln}^{h1} &= H_{jl} \frac{\partial h_j}{\partial \dot{x}_k} F_{k,n} \\ K_{ln}^{h2} &= -H_{jl} \frac{\partial h_j}{\partial \dot{x}_k} (D_{i,k})^{-1} D_{i,pq} \dot{x}_p F_{q,n} \\ K_{ln}^m &= H_{jl} M_{jk,p} F_{p,n} g_k \\ K_{ln}^{g1} &= -H_{jl} M_{jk} (D_{i,k})^{-1} D_{i,pq} g_p F_{q,n} \\ K_{ln}^{g2} &= F_{j,l} M_{jk} (D_{i,k})^{-1} \{D_{i,pq} + D_{i,qp}\} \dot{x}_p [(D_{t,q})^{-1} D_{t,uv} \dot{x}_u F_{v,n}] \\ K_{ln}^{g3} &= -H_{jl} M_{jk} (D_{i,k})^{-1} D_{i,pqv} \dot{x}_p \dot{x}_q F_{v,n}. \end{aligned} \quad (\text{A.116})$$

The indices used are given by

$$\begin{aligned} l, m &= \iota(\varepsilon^d), \quad n = \iota(\varepsilon^d, \varepsilon^k), \quad i, t = \iota(\varepsilon^o, \varepsilon^m, \varepsilon^d, s^o), \quad j, k, p, q, u, v = \iota(x^c), \\ r, s &= \iota(\varepsilon^r). \end{aligned}$$

The linearization of the second part of the state equations,  $d\varepsilon^d/dt = \varepsilon^d$ , is trivial.

The last part, is the linearization of the velocities of the kinematic coordinates (A.109), or the non-holonomic constraints explicitly written in terms of the state variables, yielding

$$\Delta \dot{\varepsilon}_p = A_{pm} \Delta \dot{\varepsilon}_m + B_{pn} \Delta \varepsilon_n, \quad p = \iota(\varepsilon^k), \quad m = \iota(\varepsilon^d), \quad n = \iota(\varepsilon^d, \varepsilon^k), \quad (\text{A.117})$$

The  $A$  and  $B$  matrix can be derived in a similar procedure as in (A.49) yielding

$$\begin{aligned} A_{pm} &= D_{p,j} H_{jm} \\ B_{pn} &= D_{p,jk} H_{jq} \dot{\varepsilon}_q F_{k,n} - D_{p,j} (D_{i,j})^{-1} D_{i,uv} H_{uq} \dot{\varepsilon}_q F_{v,n}, \quad q = \iota(\varepsilon^m). \end{aligned} \quad (\text{A.118})$$

These equations (A.117) can be compared to (2.41) in the main body of the text. Note that in the case of zero nominal motion,  $\dot{\varepsilon}^m = 0$ , the  $B$  matrix is zero.

## Appendix B

# Quaternions, Finite Rotation, and Euler Parameters

SON: Well, Papa, can you multiply triplets?

FATHER: No [sadly shaking his head], I can only add and subtract them.

(William Rowan Hamilton, Conversation with his sons (1843))

A quaternion is a collection of four real parameters, of which the first is considered as a scalar and the other three as a vector in three-dimensional space. In addition, the following operations are defined. If  $q = (q_0, \mathbf{q}) = (q_0, q_1, q_2, q_3)$  and  $p = (p_0, \mathbf{p}) = (p_0, p_1, p_2, p_3)$  are two quaternions, their sum is defined as

$$q + p = (q_0 + p_0, \mathbf{q} + \mathbf{p}), \quad (\text{B.1})$$

and their product (non-commutative) as

$$q \circ p = (q_0 p_0 - \mathbf{q} \cdot \mathbf{p}, q_0 \mathbf{p} + p_0 \mathbf{q} + \mathbf{q} \times \mathbf{p}). \quad (\text{B.2})$$

The adjoint quaternion of  $q$  is defined as  $\bar{q} = (q_0, -\mathbf{q})$  and the length or norm as  $|q| = \sqrt{(\bar{q} \circ q)_0} = \sqrt{q_0^2 + \mathbf{q} \cdot \mathbf{q}}$ . Note that  $|q \circ p| = |q||p|$ . There are two special quaternions, the unit element  $1 = (1, \mathbf{0})$  and the zero element  $0 = (0, \mathbf{0})$ . The reciprocal of a quaternion  $q \neq 0$  is  $q^{-1} = \bar{q}/|q|^2$ . The quaternion with a norm of one,  $|q| = 1$ , is a unit quaternion.

If a quaternion is looked upon as a four-dimensional vector, the quaternion

product can be described by a matrix-vector product as

$$\begin{aligned} q \circ p &= \begin{pmatrix} q_0 & -\mathbf{q}^T \\ \mathbf{q} & q_0 \mathbf{I}_3 + \tilde{\mathbf{q}} \end{pmatrix} \begin{pmatrix} p_0 \\ \mathbf{p} \end{pmatrix} = \mathbf{Q} \begin{pmatrix} p_0 \\ \mathbf{p} \end{pmatrix}, \\ p \circ q &= \begin{pmatrix} q_0 & -\mathbf{q}^T \\ \mathbf{q} & q_0 \mathbf{I}_3 - \tilde{\mathbf{q}} \end{pmatrix} \begin{pmatrix} p_0 \\ \mathbf{p} \end{pmatrix} = \overline{\mathbf{Q}} \begin{pmatrix} p_0 \\ \mathbf{p} \end{pmatrix}. \end{aligned} \quad (\text{B.3})$$

Here we have used the tilde notation for the antisymmetric matrix  $\tilde{\mathbf{q}}$  from the vector  $\mathbf{q}$ , which is defined by the matrix-vector notation for the vector cross product  $\mathbf{q} \times \mathbf{x} = \tilde{\mathbf{q}}\mathbf{x}$ . This skew-symmetric matrix is

$$\tilde{\mathbf{q}} = \begin{pmatrix} 0 & -q_3 & q_2 \\ q_3 & 0 & -q_1 \\ -q_2 & q_1 & 0 \end{pmatrix}. \quad (\text{B.4})$$

The quaternion matrices  $\mathbf{Q}$  and  $\overline{\mathbf{P}}$  commute,  $\mathbf{Q}\overline{\mathbf{P}} = \overline{\mathbf{P}}\mathbf{Q}$ . The matrices of the adjoint quaternion  $\bar{q}$  are  $\mathbf{Q}^T$  and  $\overline{\mathbf{Q}}^T$ .

If we associate the quaternion  $x' = (0, \mathbf{x}')$  with the three-dimensional vector  $\mathbf{x}'$  and define the operation, with the unit quaternion  $q$ , as

$$x = q \circ x' \circ q^{-1} = q \circ x' \circ \bar{q}, \quad (\text{B.5})$$

then this transformation, from  $x'$  to  $x$ , represents a rotation. The resulting quaternion  $x$  is a vectorial quaternion with the same length as  $x'$ . The case of reflection, the other possibility, can be excluded. The rotation matrix  $\mathbf{R}$  in terms of the unit quaternions  $q$  can be derived from equation (B.5) as

$$\mathbf{x} = (q_0^2 - \mathbf{q} \cdot \mathbf{q})\mathbf{x}' + 2q_0(\mathbf{q} \times \mathbf{x}') + 2(\mathbf{q} \cdot \mathbf{x}')\mathbf{q} = \mathbf{R}\mathbf{x}' \quad (\text{B.6})$$

with

$$\mathbf{R} = \begin{pmatrix} q_0^2 + q_1^2 - q_2^2 - q_3^2 & 2(q_1q_2 - q_0q_3) & 2(q_1q_3 + q_0q_2) \\ 2(q_2q_1 + q_0q_3) & q_0^2 - q_1^2 + q_2^2 - q_3^2 & 2(q_2q_3 - q_0q_1) \\ 2(q_3q_1 - q_0q_2) & 2(q_3q_2 + q_0q_1) & q_0^2 - q_1^2 - q_2^2 + q_3^2 \end{pmatrix}. \quad (\text{B.7})$$

This rotation matrix can also be written with the help of the quaternion matrix representation according to

$$\begin{pmatrix} 1 & \mathbf{0}^T \\ \mathbf{0} & \mathbf{R} \end{pmatrix} = \mathbf{Q}\overline{\mathbf{Q}}^T = \overline{\mathbf{Q}}^T\mathbf{Q}. \quad (\text{B.8})$$

The quaternion  $q$  in the rotation matrix  $\mathbf{R}$  according to equation (B.7), is identified as the set of Euler parameters for the description of finite rotation. According to Euler's theorem on finite rotation, a rotation in space can always be described by a rotation along a certain axis over a certain angle. With the unit vector  $\mathbf{e}_\mu$  representing the axis and the angle of rotation  $\mu$ , right-handed positive, the Euler parameters  $q$  can be interpreted as

$$q_0 = \cos(\mu/2) \quad \text{and} \quad \mathbf{q} = \sin(\mu/2)\mathbf{e}_\mu. \quad (\text{B.9})$$

Since the Euler parameters are unit quaternions the subsidiary condition,

$$q_0^2 + q_1^2 + q_2^2 + q_3^2 = 1, \quad (\text{B.10})$$

must always be satisfied. The quaternion  $x'$  in (B.5) can now be associated with the algebraic components of a vector in a body fixed frame and the quaternion  $x$  as the corresponding components expressed in a space fixed frame.

The Euler parameters for successive rotation are given by the quaternion product of the Euler parameters describing the individual rotations. This property is successfully used in the formulation of the relative rotation of the spatial hinge element from Section 3.4.

Before we derive the rotational equations of motion for a spatial rigid body in terms of Euler parameters we have to express the angular velocities and accelerations in terms of the Euler parameters and its time derivatives. By differentiation of the rotational transformation (B.5) as in

$$\dot{x} = \dot{q} \circ x' \circ \bar{q} + q \circ x' \circ \dot{\bar{q}}, \quad (\text{B.11})$$

and substitution of the body fixed coordinates according to  $x' = \bar{q} \circ x \circ q$ , realizing that  $\bar{q} \circ q$  is the unit element  $(1, \mathbf{0})$ , the velocity reads

$$\dot{x} = \dot{q} \circ \bar{q} \circ x + x \circ q \circ \dot{\bar{q}}. \quad (\text{B.12})$$

The scalar part of the products  $\dot{q} \circ \bar{q}$  and  $q \circ \dot{\bar{q}}$  are zero, since  $q$  is a unit quaternion, and the vector parts are opposite so we may write:  $\dot{q} \circ \bar{q} = (0, \mathbf{w})$  and  $q \circ \dot{\bar{q}} = (0, -\mathbf{w})$ . The velocity  $\dot{x}$  now has a zero scalar part, as expected, and a vectorial part,  $\dot{\mathbf{x}} = 2\mathbf{w} \times \mathbf{x}$ , so  $\boldsymbol{\omega} = 2\mathbf{w}$ . We conclude that the angular velocity  $\boldsymbol{\omega}$  expressed in the space fixed reference in terms of the Euler parameters  $q$  and its time derivatives is given by

$$\boldsymbol{\omega} = 2\dot{q} \circ \bar{q} \quad \text{or} \quad \begin{pmatrix} 0 \\ \boldsymbol{\omega} \end{pmatrix} = 2\bar{\mathbf{Q}}^T \begin{pmatrix} \dot{q}_0 \\ \dot{\mathbf{q}} \end{pmatrix}. \quad (\text{B.13})$$

The inverse, the time derivatives  $\dot{q}$  of the Euler parameters for given  $q$  and  $\omega$ , can be found as

$$\dot{q} = \frac{1}{2}\omega \circ q \quad \text{or} \quad \begin{pmatrix} \dot{q}_0 \\ \dot{\mathbf{q}} \end{pmatrix} = \frac{1}{2}\overline{\mathbf{Q}} \begin{pmatrix} 0 \\ \omega \end{pmatrix}. \quad (\text{B.14})$$

Note that these time derivatives are always uniquely defined, opposed to the classical combination of 3 parameters for describing spatial rotation as in for example Euler angles, Rodrigues parameters or Cardan angles. The angular velocities  $\omega'$  expressed in a body fixed reference frame can be derived in the same manner, or by application of the rotational transformation (B.8), as

$$\omega' = 2\overline{q} \circ \dot{q} \quad \text{or} \quad \begin{pmatrix} 0 \\ \omega' \end{pmatrix} = 2\mathbf{Q}^T \begin{pmatrix} \dot{q}_0 \\ \dot{\mathbf{q}} \end{pmatrix}, \quad (\text{B.15})$$

and with the inverse

$$\dot{q} = \frac{1}{2}q \circ \omega' \quad \text{or} \quad \begin{pmatrix} \dot{q}_0 \\ \dot{\mathbf{q}} \end{pmatrix} = \frac{1}{2}\mathbf{Q} \begin{pmatrix} 0 \\ \omega' \end{pmatrix}. \quad (\text{B.16})$$

The angular accelerations are found by differentiation of the expressions for  $\omega$  and  $\omega'$ , resulting in

$$\begin{pmatrix} 0 \\ \dot{\omega} \end{pmatrix} = 2\overline{\mathbf{Q}}^T \begin{pmatrix} \ddot{q}_0 \\ \ddot{\mathbf{q}} \end{pmatrix} + 2 \begin{pmatrix} |\dot{q}|^2 \\ \mathbf{0} \end{pmatrix}, \quad (\text{B.17})$$

and expressed in the body fixed reference frame

$$\begin{pmatrix} 0 \\ \dot{\omega}' \end{pmatrix} = 2\mathbf{Q}^T \begin{pmatrix} \ddot{q}_0 \\ \ddot{\mathbf{q}} \end{pmatrix} + 2 \begin{pmatrix} |\dot{q}|^2 \\ \mathbf{0} \end{pmatrix}. \quad (\text{B.18})$$

The inverse, the second order time derivatives  $\ddot{q}$  of the Euler parameters in terms of  $q$ ,  $\dot{q}$  and  $\dot{\omega}$ , goes without saying. The equations of motion for the rotation of a rigid body in a space with the components of the inertia tensor as matrix  $\mathbf{J}'$  and the vector of applied torques  $\mathbf{M}'$ , all at the centre of mass expressed in the body fixed frame, are

$$\mathbf{J}'\dot{\omega}' = \mathbf{M}' - \omega' \times (\mathbf{J}'\omega'), \quad (\text{B.19})$$

They can be expressed in terms of Euler parameters and its time derivatives by application of the principle of virtual power and introduction of the Lagrangian multiplier  $\lambda$  for the norm constraint (B.10) written as

$$\varepsilon_q = q_0^2 + q_1^2 + q_2^2 + q_3^2 - 1 = 0, \quad (\text{B.20})$$

resulting in the virtual power equation for a rigid body as

$$(\mathbf{M}' - \mathbf{J}'\dot{\boldsymbol{\omega}}' - \boldsymbol{\omega}' \times (\mathbf{J}'\boldsymbol{\omega}'))^T \delta\boldsymbol{\omega}' = \lambda \delta\dot{\varepsilon}_q. \quad (\text{B.21})$$

The virtual constraint rate can be derived from (B.20) as

$$\delta\dot{\varepsilon}_q = 2q_0\delta\dot{q}_0 + 2\mathbf{q}^T\delta\dot{\mathbf{q}}. \quad (\text{B.22})$$

Substitution of these expressions and the expressions for the angular velocities (B.15) and the angular accelerations (B.18) in the virtual power equation (B.21) and taking arbitrary virtual Euler parameter velocities yields after adding the constraints on the accelerations of the Euler parameters as in (B.17) or (B.18), the equations of motion for a rigid body expressed in terms of Euler parameters as

$$\begin{bmatrix} 4\mathbf{Q} \begin{pmatrix} 0 & \mathbf{0}^T \\ \mathbf{0} & \mathbf{J}' \end{pmatrix} \mathbf{Q}^T & 2 \begin{pmatrix} q_0 \\ \mathbf{q} \\ 0 \end{pmatrix} \end{bmatrix} \begin{bmatrix} \ddot{q}_0 \\ \ddot{\mathbf{q}} \\ \lambda \end{bmatrix} = \begin{bmatrix} 2\mathbf{Q} \begin{pmatrix} 0 \\ \mathbf{M}' \end{pmatrix} + 8\dot{\mathbf{Q}} \begin{pmatrix} 0 & \mathbf{0}^T \\ \mathbf{0} & \mathbf{J}' \end{pmatrix} \dot{\mathbf{Q}}^T \begin{pmatrix} q_0 \\ \mathbf{q} \end{pmatrix} \\ -2|\dot{\mathbf{q}}|^2 \end{bmatrix}. \quad (\text{B.23})$$

The multiplier  $\lambda$  can for this single body be obtained by premultiplying the first four equations by  $(q_0, \mathbf{q})^T$  and is identified as twice the rotational kinetic energy of the body

$$\lambda = 4 \begin{pmatrix} q_0 \\ \mathbf{q} \end{pmatrix}^T \dot{\mathbf{Q}} \begin{pmatrix} 0 & \mathbf{0}^T \\ \mathbf{0} & \mathbf{J}' \end{pmatrix} \dot{\mathbf{Q}}^T \begin{pmatrix} q_0 \\ \mathbf{q} \end{pmatrix} = \boldsymbol{\omega}'^T \mathbf{J}' \boldsymbol{\omega}'. \quad (\text{B.24})$$

The transformations of an applied torque, body fixed  $\mathbf{M}'$  or space fixed  $\mathbf{M}$ , to the torque parameters  $(f_0, \mathbf{f})$ , which are dual to the Euler parameters, are apparently

$$\begin{pmatrix} f_0 \\ \mathbf{f} \end{pmatrix} = 2\mathbf{Q} \begin{pmatrix} 0 \\ \mathbf{M}' \end{pmatrix}, \quad \text{and} \quad \begin{pmatrix} f_0 \\ \mathbf{f} \end{pmatrix} = 2\overline{\mathbf{Q}} \begin{pmatrix} 0 \\ \mathbf{M} \end{pmatrix}. \quad (\text{B.25})$$



## Appendix C

# An Algorithm for Hydrodynamic Journal Bearing Forces

Another circumstance brought out by the theory, and remarked on both by Lord Rayleigh and the author at Montreal, but not before expected, is that the point of nearest approach of the journal to the brass is not by any means in the line of the load, and, what is still more contrary to common supposition, is on the *off* side of the line of load.

(Osborne Reynolds, *On the theory of lubrication and its application to Mr. Beauchamp tower's experiments, including an experimental determination of the viscosity of olive oil*)

This appendix gives an algorithmic interpretation of the closed form analytical expressions for the approximate load bearing properties of a fluid film lubricated full journal bearing given by Moes *et al.* [51]. Their solution is based on the Reynolds equation for a thin film. Incorporated is the finite length of the bearing and the effect of cavitation in the fluid film. A good reference to the theory of hydrodynamic lubrication is the book by Pinkus and Sternlicht [60].

Let us consider a full journal bearing with journal radius  $r$ , radial clearance  $c$ , bearing length  $l$ , and lubricant dynamic viscosity  $\mu$ . Attached to the sleeve is a Cartesian reference frame  $Oxy$  with  $O$  in the centre of the sleeve. The position and velocities of the journal centre with respect to the reference frame  $Oxy$  of the sleeve are denoted by  $x, y$  and  $\dot{x}, \dot{y}$ . Let  $\omega$  be the angular velocity of the journal with respect to the reference frame  $Oxy$ , and  $\bar{\omega}$  and  $\lambda$  be defined by

$$\begin{aligned}\bar{\omega} &= \omega/2, \\ \lambda &= l/(2r).\end{aligned}\tag{C.1}$$

Then the algorithm is as follows. Calculate the components of the pure-squeeze velocity  $\mathbf{v}$  as

$$\begin{bmatrix} v_x \\ v_y \end{bmatrix} = \begin{bmatrix} \dot{x} \\ \dot{y} \end{bmatrix} - \begin{bmatrix} 0 & -\bar{\omega} \\ \bar{\omega} & 0 \end{bmatrix} \begin{bmatrix} x \\ y \end{bmatrix} \quad (\text{C.2})$$

Let  $\varphi$  be the angle of this vector with the  $x$ -axis, and  $v_s$  the magnitude,

$$\begin{aligned} \tan \varphi &= v_y/v_x, \\ v_s &= \sqrt{v_x^2 + v_y^2}. \end{aligned} \quad (\text{C.3})$$

Express the scaled journal positions  $x/c$  and  $y/c$  in the coordinate system rotated over the angle  $\varphi$ ,

$$\begin{bmatrix} \xi \\ \eta \end{bmatrix} = \begin{bmatrix} \cos \varphi & \sin \varphi \\ -\sin \varphi & \cos \varphi \end{bmatrix} \begin{bmatrix} x/c \\ y/c \end{bmatrix} \quad (\text{C.4})$$

Define the eccentricity as the length of this vector,

$$\varepsilon = \sqrt{\xi^2 + \eta^2}. \quad (\text{C.5})$$

Calculate the dimensionless damping coefficients  $\mathbf{W}_s$  or impedance vector for the short bearing (Ocvirk [60]) with ruptured or cavitating fluid film, with

$$\begin{aligned} G_s &= \left(\frac{\lambda}{1-\varepsilon^2}\right)^2, \\ J_s &= \frac{2}{\sqrt{1-\varepsilon^2}} \arccos\left(-\frac{\xi}{\sqrt{1-\eta^2}}\right), \end{aligned} \quad (\text{C.6})$$

as:

$$\begin{aligned} W_{sxx} &= G_s((1-\varepsilon^2+3\xi^2)J_s+6\xi), \\ W_{syy} &= G_s\eta(3\xi J_s+4+2\frac{\xi^2}{1-\eta^2}). \end{aligned} \quad (\text{C.7})$$

Calculate the damping coefficients  $\mathbf{W}_l$  for the long bearing (Sommerfeld [60]) with ruptured fluid film, with

$$\begin{aligned} G_l &= \frac{3}{2(1-\varepsilon^2)(1+\frac{1}{2}\varepsilon^2)}, \\ K_l &= \sqrt{(1+\frac{1}{2}\varepsilon^2)^2 - (1+\frac{1}{4}\varepsilon^2)\eta^2}, \\ J_l &= \frac{2}{\sqrt{1-\varepsilon^2}} \arccos\left(-\frac{(1+\frac{1}{2}\varepsilon^2)\xi}{\sqrt{K_l^2-\eta^2}}\right), \end{aligned} \quad (\text{C.8})$$

as:

$$\begin{aligned} W_{lx} &= G_l((2+\varepsilon^2-3\eta^2)J_l+4\xi K_l), \\ W_{ly} &= G_l\eta(3\xi J_l+4K_l). \end{aligned} \quad (\text{C.9})$$

The damping coefficients of the finite length bearing are approximated by the value as if the short- and long bearing damper were connected in series,

$$\begin{aligned} W_x &= 1/(1/W_{sx} + 1/W_{lx}), \\ W_y &= 1/(1/W_{sy} + 1/W_{ly}). \end{aligned} \quad (\text{C.10})$$

The components of the bearing force  $\mathbf{F}$ , being the force exerted by the fluid film on the sleeve expressed in the Cartesian reference frame  $Oxy$  of the sleeve, are

$$\begin{bmatrix} F_x \\ F_y \end{bmatrix} = 2\mu l \left(\frac{r}{c}\right)^3 v_s \begin{bmatrix} \cos \varphi & -\sin \varphi \\ \sin \varphi & \cos \varphi \end{bmatrix} \begin{bmatrix} W_x \\ W_y \end{bmatrix}. \quad (\text{C.11})$$



# Summary

Dynamic simulation of flexible multibody systems is a time consuming task. It is not that the current computers are too slow, rather that the simulation timestep gets to be so small that the total simulation time runs out of hand. Furthermore, the enormous amount of data produced in this way hinders the interpretation of the results. Fortunately, it now appears that linear vibration analysis can be applied to solve the problem.

In this thesis the complex motion of the flexible multibody system is approximated by superimposing small linear vibrations on a non-linear rigid body motion. This idea has been inspired by the computational results from simulations of flexible multibody systems where one often recognizes the motion to be the sum of a gross rigid body motion and small-amplitude, nearly harmonic vibrations.

For a periodic rigid body motion, the method of superimposition as presented in this thesis systematically leads to a system of linear differential equations with periodic coefficients and periodic forcing. Periodic solutions of these equations are assumed to be truncated Fourier series with the same fundamental frequency as the nominal rigid body motion. These series have the advantage that they are a compact frequency-amplitude representation of the solution as opposed to the lengthy time responses. The stability of these periodic solutions is determined by a method which is directly based on the Floquet theory. Transient solutions, which may be added in order to satisfy the initial conditions, are constructed by a method of slowly varying coefficients and averaging.

The equations of motion for the flexible multibody system and their linearization, which describe the small vibrations, are derived by a finite element method. With the help of a limited number of element types, the truss, the beam and the hinge, it is possible to model a variety of flexible multibody systems. The field of application is enlarged by the introduction in this work of new element types, being: the planar cylindrical bearing, the planar belt and

pulley pair, the planar gear pair, and the spatial hinge. Every element type is illustrated by a suitable example problem.

The method of superimposition as presented in this work is also applied to systems having rolling contact, as in road vehicles and track-guided vehicles. If these contacts are ideal, they impose, in addition to some holonomic constraints, also non-holonomic constraints on the system, which can be expressed as constraints of special finite elements like the wheel on a surface. These new element types and a procedure for formulating the equations of motion for such non-holonomic flexible multibody systems and their linearization are an important part of this thesis. The application of these new element types and techniques is illustrated by the stability analysis of a rolling disk and a benchmark problem on a road vehicle.

Finally, a comparative study on the effect of joint clearance modelling in a flexible multibody system illustrates yet another application of the presented superimposition method.

# Samenvatting

Dynamische simulatie van vervormbare meerlichaamsystemen is een tijdrovende bezigheid. Het is niet zo dat de huidige computers te traag zijn maar dat de benodigde rekentijdstep zo klein wordt dat de totale rekentijd uit de hand loopt. Daarbij komt nog dat de enorme hoeveelheid gegevens die zo geproduceerd wordt de interpretatie van de resultaten in de weg staat. Gelukkig kan dit probleem opgelost worden door het toepassen van eenvoudige trillingsleer.

In dit proefschrift wordt voorgesteld de complexe beweging van een vervormbaar meerlichaamsysteem te benaderen door de superpositie van kleine trillingen op een beweging met starre lichamen. Dit idee is ingegeven door de berekeningsresultaten van vervormbare meerlichaamsystemen waarbij men vaak in de beweging de som herkent van een starre lichaamsbeweging en een kleine nagenoeg harmonische trilling.

De methode van superpositie zoals hier gepresenteerd leidt bij een periodieke starre lichaamsbeweging tot een stelsel lineaire differentiaal vergelijkingen met periodieke coëfficiënten en een periodiek rechterlid welke de kleine trillingen beschrijven. Als periodieke oplossing wordt een eindige reeks van Fourier verondersteld waarbij de grondfrequentie gelijk is aan die van de starre lichaamsbeweging. Deze reeksen hebben het voordeel van een compacte frequentie-amplitude vorm tegenover de langdurige tijdresponsies. De stabiliteit van de periodieke oplossingen wordt bepaald met behulp van een methode die direct gebaseerd is op de theorie van Floquet. Het inschakelverschijnsel, wat eventueel kan worden toegevoegd aan de periodieke oplossing om aan de beginvoorwaarden te voldoen, wordt bepaald met behulp van de methode van langzaam veranderende fase en amplitude en die van middeling.

De bewegingsvergelijkingen voor het vervormbare meerlichaamsysteem en de linearisatie welke de kleine trillingen beschrijft, worden bepaald met behulp van de eindige-elementenmethode. Door middel van een beperkt aantal typen elementen zoals de staaf, de balk en het scharnier, kan een grote groep van ver-

vormbare meerlichaamsystemen gemodelleerd worden. De in dit werk beschreven nieuwe elementtypen zoals het vlakke cilindrische lager, de vlakke riem met riemschijven, het vlakke tandwiel en het ruimtelijke scharnier vergroten dit toepassingsgebied nog meer. Al deze nieuwe elementtypen zijn geïllustreerd met een toepasselijk voorbeeld.

De methode van superpositie zoals hier gepresenteerd, kan ook worden toegepast bij systemen met rollende contacten zoals bij weg- en railvoertuigen. De niet-holonome verbindingsvoorwaarden die ontstaan bij het beschrijven van zuiver rollend contact worden beschreven met behulp van speciale eindige elementen zoals het wiel op een vlak. Deze bijzondere eindige elementen en de formulering van de bewegingsvergelijkingen voor zulke niet-holonome vervormbare meerlichaamsystemen en de linearisatie hiervan zijn een belangrijk onderdeel van dit proefschrift. De nieuwe elementen en technieken worden onder andere geïllustreerd aan de hand van de stabiliteitsanalyse van een rollende schijf en een standaardtest op een simulatiemodel van een wegvoertuig.

Tot slot is een vergelijkende studie naar het modelleren van speling in vervormbare meerlichaamsystemen gedaan. Dit onderzoek illustreert tevens een geheel ander toepassingsgebied van de hier gepresenteerde methode van superpositie.

# Curriculum Vitae

- April 6, 1955 Born in Naarden, the Netherlands.
- 1974–1979 BSc study in Mechanical Engineering at Dordrecht Polytechnical School. Graduated with distinction.
- 1979–1981 Military Service.
- 1979–1983 MSc study in Mechanical Engineering at Delft University of Technology. Graduated with distinction at the Laboratory for Engineering Mechanics under the direction of Prof. dr ir J. F. Besseling. Titel of MSc-thesis (in Dutch): “Dynamica van Mechanismen met Vervormbare Schakels,” *Dynamics of Mechanisms with Compliant Links*
- 1983–1986 Assistant Professor at Delft University of Technology, Laboratory for Engineering Mechanics, headed by Prof. dr ir J. F. Besseling.
- 1986–1991 Assistant Professor at Delft University of Technology, department of Mechanical Engineering, Computer Aided Design, headed by Prof. dr ir K. Van der Werff.
- 1991–present Assistant Professor at Delft University of Technology, Laboratory for Engineering Mechanics, headed by Prof. dr ir L. J. Ernst.



# References

Some readers look at the reference list immediately after reading the title, and if the references do not look sufficiently familiar, interesting or comprehensive they may decide not to read further.

(Nicholas J. Higham, *Handbook of Writing for the Mathematical Sciences*)

Numbers within square brackets [ ] at the end of a reference indicate the page numbers on which the reference appears.

- [1] Aannaque, A., Garvey, S., Bennouna, M., and Penny, J., “Operation of a four-bar mechanism above several critical speeds,” *ASME Journal of Vibration and Acoustics* **118**, 1996, pp.198–203. [54]
- [2] Besseling, J. F., “The complete analogy between the matrix equations and the continuous field equations of structural analysis,” in *International symposium on analogue and digital techniques applied to aeronautics: Proceedings*, Presses Académiques Européennes, Bruxelles, 1964, pp. 223–242. [2]
- [3] Bolotin, V. V., *The Dynamic Stability of Elastic Systems*, Holden-Day, San Francisco, 1964. [54, 60]
- [4] Bottema, O., “On the small vibration of non-holonomic systems,” *Proceedings Koninklijke Nederlandse Akademie van Wetenschappen* **52**, 1949, pp. 848–850. [10, 15]
- [5] Bottema, O., and Roth, B., *Theoretical Kinematics*, North-Holland, Amsterdam, 1979. [30]

- [6] Brenan, K. E., Campbell, S. L., and Petzold, L. R., *The Numerical Solution of Initial Value Problems in Differential-Algebraic Equations*, North-Holland, New York, 1989. (corrected reprint by SIAM, Philadelphia PA, 1996). [111]
- [7] Brigham E. O., *The Fast Fourier Transform*, Prentice-Hall, Englewood Cliffs NJ, 1974. [56]
- [8] Cardona, A., Coune, T., Lerusse, A., and Géradin, M., “A multiharmonic method for non-linear vibration analysis,” *International Journal for Numerical Methods in Engineering* **37**, 1994, pp. 1593–1608. [54]
- [9] Carroll, L., *Alice’s Adventures in Wonderland*, 1865. [17]
- [10] Cleghorn, W. L., Fenton, R. G., and Tabarrok, B., “Steady-state vibrational response of high-speed flexible mechanisms,” *Mechanism and Machine Theory* **19**, 1984, pp. 417–423. [54]
- [11] Deck, J. F., and Dubowsky, S., “On the limitations of predictions of the dynamic response of machines with clearance connections,” *ASME Journal of Mechanical Design* **116**, 1994, pp. 833–841. [80]
- [12] Den Hartog, J. P., *Mechanical Vibrations*, 4th ed., McGraw-Hill, New York and London, 1956. [39, 40]
- [13] Dubowsky, S., and Gardner, T. N., “Design and analysis of multilink flexible mechanisms with multiple clearance connections,” *ASME Journal of Engineering for Industry* **99**, 1977, pp. 88–96. [92, 96]
- [14] Dürr, A., *Die Kantaten von Johann Sebastian Bach*, Bärenreiter-Verlag, Kassel, 1971. [103]
- [15] Floquet, G., “Sur les équations différentielles linéaires à coefficients périodiques,” *Annales Scientifiques de l’École Normale Supérieure*, Sér. 2, Tome 12, 1883, pp. 47–88. [54, 58]
- [16] Friedmann, P. P., “Numerical methods for the treatment of periodic systems with applications to structural dynamics and helicopter rotor dynamics,” *Computers & Structures* **35**, 1990, pp. 329–347. [54]
- [17] Gear, C. W., “An introduction to numerical methods for ODEs and DAEs,” in Haug, E.J., and Deyo, R.C. (eds.), *Real-time integration methods for mechanical system simulation*, (NATO ASI series F69), Springer-Verlag, Berlin, 1991, pp. 115–126. [111]

- [18] Glasgow, D. A., and Nelson, H. D., "Stability analysis of rotor-bearing systems using component mode synthesis," *ASME Journal of Mechanical Design* **102**, 1980, pp. 352–358. [68]
- [19] Golub, G. H., and Van Loan, C. F., *Matrix Computations*, third edition, The Johns Hopkins University Press, Baltimore and London, 1996. [60]
- [20] Hain, K., "Einflüsse von Gelenkspiel und Reibung auf die im Getriebe wirkenden Kräfte," (VDI Fortschrittberichte, Reihe 1: Konstruieren Konstruktionstechnik, Nr. 17) VDI Verlag, Düsseldorf, 1969. [79]
- [21] Haines, R. S., "Survey: 2-dimensional motion and impact at revolute joints," *Mechanism and Machine Theory* **15**, 1980, pp. 361–370. [79]
- [22] Harris, T. A., *Rolling Bearing Analysis*, Wiley, New York, 1996. [83]
- [23] Hertz, H., "Über die Berührung fester elastischer Körper," *Journal für die reine und angewandte Mathematik* **92**, 1882, pp. 156–171. [82]
- [24] Higham, N. J., *Handbook of Writing for the Mathematical Sciences*, 2nd ed., siam, Philadelphia, 1998. [147]
- [25] Hill, G. W., "On the part of the motion of the lunar perigee which is a function of the mean motions of the sun and moon," *Acta Mathematica* **8**, 1886, pp. 1–36. (Previously published by J. Wilson and Son, Cambridge MA, 1877) [60]
- [26] Hofstadter, D. G., *Gödel, Escher, Bach: an Eternal Golden Braid*, Basic Books, New York, 1979. [79]
- [27] Hunt, K. H., and Crossley, F. R. E., "Coefficient of restitution interpreted as damping in vibroimpact," *ASME Journal of Applied Mechanics* **42**, 1975, pp. 440–445. [82]
- [28] Johnson, K. L., *Contact Mechanics*, Cambridge University Press, Cambridge, UK, 1985. [45]
- [29] Jonker, J. B., *A finite element dynamic analysis of flexible spatial mechanisms and manipulators*, Dissertation, Delft University Press, Delft, 1988. [2]
- [30] Jonker, J. B., "A finite element dynamic analysis of spatial mechanisms with flexible links," *Computer Methods in Applied Mechanics and Engineering* **76**, 1989, pp. 17–40. [65]

- [31] Jonker, J. B., and Meijaard, J. P., “SPACAR—Computer program for dynamic analysis of flexible spatial mechanisms and manipulators,” in *Multibody Systems Handbook*, W. Schiehlen (ed.), Springer-Verlag, Berlin, 1990, pp. 123–143. [2]
- [32] Jonker, J. B., “A finite element dynamic analysis of flexible manipulators,” *The International Journal of Robotics Research* **9**(4), 1990, pp. 59–74. [2]
- [33] Jonker, J. B., and Aarts, R. G. K. M., “Modelling of flexible mechanisms and manipulators for control purposes,” in Schweitzer, G., Siegwart, R., and Cattin, P. (eds.), *Proceedings of the Fourth International Conference on Motion and Vibration Control*, MoViC, Augustus, 1998, Zürich, Switzerland, Institute of Robotics, ETH-Zürich, Vol 1, pp. 291–297. [105]
- [34] Kakizaki, T., Deck, J. F., and Dubowsky, S., ‘Modeling the spatial dynamics of robotic manipulators with flexible links and joint clearances,’ *ASME Journal of Mechanical Design* **115**, 1993, pp. 839–847. [80]
- [35] Kalker, J. J., *Three-Dimensional Elastic Bodies in Rolling Contact*, Kluwer, Dordrecht, 1990. [45]
- [36] Kantorovich, L. V., and Akilov, G. P., *Functional Analysis in Normed Spaces*, (Russian original published by Fizmatgiz, Moscow, 1959), (translated from the Russian by D. E. Brown; edited by A. P. Robertson), Pergamon, Oxford, 1964. [54]
- [37] Kirk, G. S., and Raven, J. E., *The Presocratic Philosophers*, Cambridge University Press, Cambridge, UK, 1957. [88]
- [38] Kortüm, W., and Sharp, R. S. (eds), *Multibody Computer Codes in Vehicle System Dynamics*, Supplement to Vehicle System Dynamics **22**, 1993. [49, 51, 52]
- [39] Lagrange, J. L., *Analytical Mechanics*, Kluwer, Dordrecht, 1997. (Original French first edition “Mécanique analytique,” Desaint, Paris, 1788) (Translated from the French second edition “Mécanique analytique,” Courcier, Paris, 1811, by A. Boissonnade and V. N. Vagliente) [5, 7]
- [40] Lankarani, H. M., and Nikravesh, P. E., ‘A contact force model with hysteresis damping for impact analysis of multibody systems,’ *ASME Journal of Mechanical Design* **112**, 1990, pp. 369–376. [81]

- [41] Lankarani, H. M., and Nikravesh, P. E., ‘Continuous contact force models for impact analysis in multibody systems,’ *Nonlinear Dynamics* **5**, 1994, pp. 193–207. [81]
- [42] Ling, F. H., and Wu, X. X., “Fast Galerkin method and its application to determine periodic solutions of non-linear oscillators,” *International Journal of Non-Linear Mechanics* **22**, 1987, pp. 89–98. [54]
- [43] Meijaard, J. P., “Direct determination of periodic solutions of the dynamical equations of flexible mechanisms and manipulators,” *International Journal for Numerical Methods in Engineering* **32**, 1991, pp. 1691–1710. [10, 54, 58]
- [44] Meijaard, J. P., “A comparison of numerical integration methods with a view to fast simulation of mechanical dynamical systems,” in Haug, E. J., and Deyo, R. C. (eds.) *Real-time integration methods for mechanical system simulation*, (NATO ASI series F69), Springer-Verlag, Berlin, 1991, pp. 329–343. [89]
- [45] Meijaard, J. P., “Direct determination of periodic solutions of mechanical dynamical systems,” *Archive of Applied Mechanics* **64**, 1994, pp. 249–257. [2, 10, 54, 58, 62, 65, 66, 67]
- [46] Meijaard, J. P., ‘Efficient numerical integration of the equations of motion of non-smooth mechanical systems,’ *Zeitschrift für angewandte Mathematik und Mechanik* **77**, pp. 1997, pp. 419–427. [88]
- [47] Meijaard, J. P., “Continuation of stationary and periodic solutions and their bifurcations,” Laboratory for Engineering Mechanics, Delft University of Technology, LTM report No 1179, September 1998. [60]
- [48] Meijaard, J. P., and Schwab, A. L., “A systematic approach to the analysis of rotor dynamic systems,” *Proceedings of 10th World Congress on the Theory of Machines and Mechanisms, June 20–24, 1999, Oulu, Finland*, Oulu University Press, Oulu, 1999, pp. 1675–1679. [68]
- [49] Meijaard, J. P., and Schwab, A. L., “A component mode synthesis look at planar beam elements,” *Proceedings of ASME 2001 Design Engineering Technical Conferences, September 9–12, 2001, Pittsburgh, Pennsylvania, CD-ROM*, ASME, New York, 2001, 10pp. [109]

- [50] Meyer zur Capellen, W., *Mathematische Instrumenten*, Akademische Verlagsgesellschaft Becker & Erler, Leipzig, 1949. [36]
- [51] Moes, H., Sikkes, E. G., and Bosma, R., “Mobility and impedance tensor methods for full and partial-arc journal bearings,” *ASME Journal of Tribology* **108**, 1986, pp. 612–620. [84, 85, 101, 104, 137]
- [52] Moffatt, H. K., “Euler’s disk and its finite-time singularity,” *Nature* **404**, 2000, pp. 833–834. [48]
- [53] Naab, K., and Weyh, B., “Verallgemeinerte Hill-Matrizen zur direkten Stabilitätsanalyse parametererregter Systeme,” *Zeitschrift für angewandte Mathematik und Mechanik* **67**, 1987, T115–T118. [60]
- [54] Nadolny, S., *Die Entdeckung der Langsamkeit*, R. Piper & Co. Verlag, München, 1983. [53]
- [55] Neĭmark, Ju. I., and Fufaev, N. A., *Dynamics of Nonholonomic Systems*, (Translated from the Russian edition, Nauka, Moscow, 1967), A.M.S., Providence RI, 1972. [10, 36, 45, 46]
- [56] Newton, I., *Philosophiæ Naturalis Principia Mathematica*, London, 1686. (The Principia: Mathematical Principles of Natural Philosophy; A New Translation by I. Bernard Cohen and Anne Whitman assisted by Julia Budenz; Preceded by A Guide to Newton’s Principia by I. Bernard Cohen, University of California Press, Berkeley, 1999.) [109]
- [57] Ota, H., and Kato, M., “Lateral vibrations of a rotating shaft driven by a universal joint (1st report, generation of even multiple vibrations by secondary moment),” *Bulletin of the JSME* **27**, 1984, pp. 2002–2007. [70]
- [58] Pais, A., ‘*Subtle is the Lord...*’ *The Science and the Life of Albert Einstein*, Oxford University Press, Oxford and New York, 1982. [107]
- [59] Pfeiffer, F., and Glocker, C., *Multibody Dynamics with Unilateral Constraints*, Wiley, New York, 1996. [80]
- [60] Pinkus, O., and Sternlicht, B., *Theory of Hydrodynamic Lubrication*, McGraw-Hill, New York, 1961. [137, 138]
- [61] Rankers, H., “Step-dwell-mechanism with a tooth-belt,” in Bautista, E., Garcia-Lomas, J., and Navarro, A. (eds.), *Proceedings of the 7th World Congress on the Theory of Machines and Mechanisms (IFTToMM)*, 17–12

- September 1987, Sevilla, Spain, Pergamon Press, Oxford, 1987, Vol.1, pp. 75–78. [29]
- [62] Ravn, P., “A continuous analysis method for planar multibody systems with joint clearance,” *Multibody System Dynamics* **2**, 1998, pp. 1–24. [80, 83, 91, 92, 93]
- [63] Reynolds, O., “On the theory of lubrication and its application to Mr. Beauchamp tower’s experiments, including an experimental determination of the viscosity of olive oil,” [From the *Philosophical Transactions of the Royal Society*, Part I., 1886.] In: Reynolds, O., *Papers on Mechanical and Physical Subjects*, **II** 1881–1900, Cambridge University Press, Cambridge, 1901, pp. 228–310. [137]
- [64] Rogers, R. J., and Andrews, G. C., “Dynamic simulation of planar mechanical systems with lubricated bearing clearances using vector-network methods,” *ASME Journal of Engineering for Industry* **99**, 1977, pp. 131–137. [74, 76, 84]
- [65] Schiehlen, W., “Multibody system dynamics: roots and perspectives,” *Multibody System Dynamics* **1**, 1997, pp. 149–188. [53]
- [66] Schiehlen, W. (ed.), *Multibody Systems Handbook*, Springer-Verlag, Berlin, 1990. [53]
- [67] Schwab, A. L., “Dynamica van Mechanismen met Vervormbare Schakels,” (in Dutch), Master Thesis, Laboratory for Engineering Mechanics, Delft University of Technology, LTM report No 758, November 1983. [2]
- [68] Schwab, A. L., “The wheel in 3D and other special finite elements for kinematic and dynamic analyses of multi body systems,” Laboratory for Engineering Mechanics, Delft University of Technology, LTM report No 820, May 1985. [4]
- [69] Schwab, A. L., and Meijaard, J. P., “Small vibrations superimposed on non-linear rigid body motion,” *Proceedings of ASME Design Engineering Technical Conferences, September 14–17, 1997, Sacramento, CA, CD-ROM*, ASME, New York, 1997, 7pp. [4]
- [70] Schwab, A. L., and Meijaard, J. P., “The belt, gear, bearing and hinge as special finite elements for kinematic and dynamic analysis of mechanisms and machines,” in Leinonen, T. (ed.), *Proceedings of the Tenth World*

- Congress on the Theory of Machines and Mechanisms*, IFToMM, June 20–24, 1999, Oulu, Finland, Oulu University Press, Vol 4, pp. 1375–1386. [4]
- [71] Schwab, A. L., and Meijaard, J. P., “Dynamics of flexible multibody systems having rolling contact: Application of the wheel element to the dynamics of road vehicles,” *Vehicle System Dynamics Supplement* **33**, 1999, pp. 338–349. [4]
- [72] Schwab, A. L., and Meijaard, J. P., *Manual SPACAR95*, Laboratory for Engineering Mechanics, Delft University of Technology, November 2000. [3]
- [73] Schwab, A. L., and Meijaard, J. P., “Small vibrations superimposed on a prescribed rigid body motion,” *Multibody System Dynamics*, 2002, in press. [4]
- [74] Schwab, A. L., Meijaard, J. P., and Meijers, P., “A comparison of revolute joint clearance models in the dynamic analysis of rigid and elastic mechanical systems,” *Mechanism and Machine Theory*, 2002, accepted. [4]
- [75] Seneviratne, L. D., and Earles, S. W. E., “Chaotic behaviour exhibited during contact loss in a clearance joint of a four-bar mechanism,” *Mechanism and Machine Theory* **27**, 1992, pp. 307–321. [80]
- [76] Shabana, A. A., “Flexible multibody dynamics: review of past and recent developments,” *Multibody System Dynamics* **1**, 1997, pp. 189–222. [53]
- [77] Shampine, L. F., and Gordon, M. K., *Computer solution of ordinary differential equations, the initial value problem*, W. H. Freeman and Company, San Francisco CA, 1975. [38, 90]
- [78] Song, J. O., and Haug, E. J., “Dynamic analysis of planar flexible mechanisms,” *Computer Methods in Applied Mechanics and Engineering* **24**, 1980, pp. 359–381. [65]
- [79] Soong, K. and Thompson, B. S., “A theoretical and experimental investigation of the dynamic response of a slider-crank mechanism with radial clearance in the gudgeon-pin joint,” *ASME Journal of Mechanical Design* **112**, 1990, pp. 183–189. [79]
- [80] Struik, D. J., *A Concise History of Mathematics*, 3rd ed., Dover, New York, 1967. [42]

- [81] Sundararajan, P., and Noah, S. T., “An algorithm for response and stability of large order non-linear systems—application to rotor systems,” *Journal of Sound and Vibration* **214**, 1998, pp. 695–723. [68, 69]
- [82] Van Der Waerden, B. L., *Hamiltons Entdeckung der Quaternionen*, Vandenhoeck & Ruprecht, Göttingen, 1973. [131]
- [83] Van Der Werff, K., *Kinematic and Dynamic Analysis of Mechanisms, a Finite Element Approach*, Dissertation, Delft University Press, Delft, 1977. [2]
- [84] Van Der Werff, K. , and Jonker, J. B., “Dynamics of flexible mechanisms,” in *Computer Aided Analysis and Optimization of Mechanical System Dynamics*, E. Haug (ed.), Springer-Verlag, Berlin, 1984, pp. 381–400. [2]
- [85] Verhulst, F., *Nonlinear Differential Equations and Dynamical Systems*, second edition, Springer Verlag, Berlin, 1996. [57]
- [86] Visser, W., and Besseling, J. F., “Large displacement analysis of beams,” Report WTHD 10, Delft University of Technology, Delft, 1969. [2]
- [87] Whitman, W., *Leaves of Grass*, 1891–92, in *Walt Whitman, Poetry and Prose*, The Library of America, New York, 1982. [1]
- [88] Whittaker, E. T., *A Treatise on the Analytical Dynamics of Particles and Rigid Bodies*, fourth edition, Cambridge University Press, Cambridge, UK, 1937. [10]
- [89] Yakubovich, V. A., and Starzhinskii, V. M., *Linear Differential Equations with Periodic Coefficients*, (Russian original published by Izdatel'stvo “Nauka,” Moscow, 1972), (translated from the Russian by D. Louvish), Israel Program for Scientific Translations, Jerusalem, 1975. [54]